UNIVERSITÀ
DEGLI STUDI
FIRENZE

DOTTORATO DI RICERCA IN
FISICA E ASTRONOMIA

CICLO XXXI

COORDINATORE Prof. D'Alessandro Raffaello

PROBING THE MANY BODY DYNAMICS OF ULTRACOLD REPULSIVE FERMI GASES OF LITHIUM ATOMS

Settore Scientifico Disciplinare FIS/03

Dottorando
Dott. Amico Andrea

Tutore
Dott. Roati Giacomo

Supervisore
Prof. Fort Chiara

Coordinatore
Prof. D'Alessandro Raffaello

Anni 2015/2018

Contents

Chapter 1

Introduction

Itinerant ferromagnetism describes systems comprising microscopic magnetic moments which are not localized in space but are instead mobile. This concept was introduced back in the thirties by the British theoretical physicist Edmund Clifton Stoner, who first devised a minimal model to describe a ferromagnetic instability in a homogeneous Fermi gas driven by short-range repulsive interactions: in a free electron gas, the competition between the kinetic energy, given by the Pauli pressure, and the interaction energy, given by the screened Coulomb potential, drives a paramagnetic to ferromagnetic phase transition, leading the development of a finite magnetization [1]. This model is crucial to understand the magnetic properties of everyday life magnets, made of common metals like iron, nickel or cobalt [2, 3] in which the carriers of magnetism are the unsaturated d-band electrons, which are extremely mobile and can be thought as a free gas. The possibility that pure short-range repulsive interactions suffice to sustain ferromagnetism is still nowadays debated. It is in fact experimentally extremely challenging to isolate the problem from many additional ingredients typically present in solid-state physics such as flat dispersion bands, multi-orbital exchange, or the presence of disorder.

In this thesis, I report our experimental investigations on the repulsive Fermi gas, studied exploiting a mixture of ultra-cold ^{6}Li atoms interacting through a Feshbach resonance. Even with the unparalleled control and purity of ultra-cold atom experiments, evidence confirming Stoner's mechanism for ferromagnetism have remained elusive [4, 5]. The main issue is that genuine strong short-range repulsive interaction, like the one obtained by means of a magnetic Feshbach resonance [6], requires an underlying attractive potential supporting a weakly bound molecular state [7]. As depicted in Figure 1.1, the energy diagram of the many-body system across the Fano-Feshbach resonance includes two energy branches: the repulsive (upper) branch and the attractive (lower) branch. For increasingly (positive) large values of the scattering length the upper branch becomes progressively unstable against the decay onto the lower-lying paired states via recombination processes [8, 9, 10, 11].

In analogy with ultrafast pump-probe experiments in solid state [12, 13], I employ radio-frequency (RF) spectroscopy to address these open problems and probe the physics of the repulsive branch with unparalleled spectral and time resolution. I will present our investigation of the upper branch and its dynamical properties describing two paradigmatic experiments.

In the first, I study the limit of a few impurities strongly interacting with a fermionic bath adopting a quasi-particle description [14, 15, 16, 17, 18]. I measure the repulsive Fermi

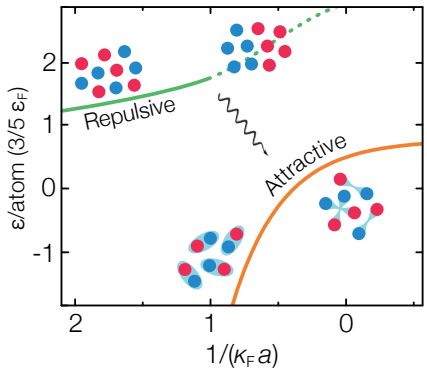

Figure 1.1: Sketch of lowest two energy branches of the repulsive Fermi gas as a function of the interaction parameter $k_F a$: the attractive (or lower) branch in orange and the repulsive (or upper) branch in green. For strong interactions the upper branch in unstable to the decay in the lower branch trough three body recombination processes.

polaron properties such as energy, effective mass, quasi-particle residue and lifetime. In particular, I find a regime of critical interactions above which the polaron energy exceeds the Fermi energy of the bath, providing a clear signature of a ferromagnetic instability of the upper branch in the impurity limit. Moreover, I find out that the polaron effective mass diverges and even turns negative, thereby indicating that the repulsive Fermi liquid state becomes thermodynamically unstable.
In a second experiment, I have characterized the energy spectrum and the out-of-equilibrium dynamics of a balanced fermionic mixture quenched to strong repulsion. As mentioned above, the interacting gas is naturally not stable at strong coupling against pairing. Therefore, its evolution is expected to be driven by the competition between these two instabilities: on the one hand recombination processes let the system decay in its paired ground-state, on the other, the strong repulsion promotes the formation of a spin anti-correlated state that wants to minimize the repulsive interaction. To disclose this intriguing and complex intertwined many-body dynamics, I have developed a selective pump-probe radio-frequency spectroscopy scheme: by the first pulse, I drive the system to selectively populate the many-body repulsive branch, while the second pulse is used to monitor the system's evolution. In this way I have probed both the molecular formation and the onset of anti-correlations, extracting for the first time, their growth rates. Both are found to arise on a time scale of the order of few Fermi time. As a main result, I have found that the growth of anti-correlations can be initially faster than pairing mechanisms. At long evolution times, I have observed that the repulsive gas evolves under the interplay between both the instabilities. The combined effect of these two mechanisms gives rise to a long-lived emulsion state of atoms and dimers in which the inter-atomic anti-correlations survive for long times. Our results clarify previous observations, which separately address the physics of the strongly repulsive Fermi gas to a ferromagnetic state sustained only by atoms [4], or to a complete absence of the upper-branch for strong repulsion due to the coupling with the molecular branch, leading to an incoherent mixture of atoms and dimers [5].

1.1 Outline of the thesis

The structure of this thesis is the following:

- In Chapter 2 I summarize the basic theory of a Fermi gas in the context of ultra-cold atoms experiments. I start from the ideal Fermi gas trapped in a harmonic potential and describe some key statistical properties of the system, focusing on the concept of atom number fluctuation. Later I introduce how I can control the inter-particle interactions between different fermions by exploiting a Feshbach resonance between different scattering channels. Finally, I will report how the presence of interaction modifies the many-body energy spectrum of the system, giving rise to the attractive and repulsive branches.

- In Chapter 3 I give some details of our experimental setup, mostly focusing on the imaging technique and the radio-frequency (RF) spectroscopy. Finally, I describe the analysis routine I employ to extract the atom number fluctuations from the density profiles obtained through absorption imaging.

- In Chapter 4 I characterize the repulsive Fermi polaron by measuring, as a function of the interaction strength, its energy, its effective mass, its residue and its lifetime. For strong repulsion, I observe the signature of a ferromagnetic instability in the polaron energy exceeding the Fermi energy of the system. All the topics discussed in this Chapter are published in PRL [19].

- In Chapter 5 I demonstrate that the upper branch of a balanced repulsive Fermi mixture is well defined up to strong coupling, even for relatively low degeneracy ($T/T_F \sim 0.8$), where T_F is the Fermi temperature. Employing a pump-probe spectroscopy scheme, I quench the system in the upper branch and subsequently probe its evolution. I study the evolution of the system for a wide range of timescales, from few to thousands of Fermi time, showing that the interplay between the pairing and the ferromagnetic instabilities produces a metastable state made of molecules and atoms which preserves spin anti-correlations. The results discussed in this Chapter are submitted to PRL and a preprint version is currently available on the arXiv [20].

Chapter 2

Theory

The classical world is the reign of distinguishability, particles can be labeled and their trajectory followed. In quantum mechanics, as soon as the wavefunctions describing two identical particles overlap, the knowledge of their original identity is washed out. This loss of information is the very foundation of the quantum statistics and deeply affects the physical behavior of a system both in its microscopic and macroscopic domain. Thermodynamics drastically changes as well as the way single particles interact with each other. In this chapter, we will see this concept at work in one of the most paradigmatic systems in nature: the Fermi gas.

We will start from the simplest case, the non-interacting ideal Fermi gas, we will derive the grand-canonical partition function and extract equilibrium properties of the system. Then we will introduce the two-components Fermi gas and show how they interact with each other deeply reshaping their many-body energy spectrum. We will introduce the concepts of the lower and upper branch, showing how the latter is unstable for strong interactions to the relaxation into the lower one.

2.1 Basic theory of Fermi gases

2.1.1 Non interacting Fermi gas

Let us consider an ensemble of identical non-interacting particles, each sharing the same energy spectrum. We name k the collection of quantum number univocally defining the state of the system, $|k\rangle$ and ε_k the corresponding eigenvector and eigenvalue. The partition function of the system within the canonical ensemble as [21] can be written as:

$$\mathcal{Z}_N = \sum_{\{n_k\}} \exp\big(-\beta \sum_k n_k \varepsilon_k\big) = \sum_{n_k} \exp\big(-\beta \sum_k n_k \varepsilon_k\big) \delta(N - \sum_k n_k), \tag{2.1}$$

where N is the total number of particle, n_k is the occupation number of $|k\rangle$, $\beta = 1/k_B T$ is the coldness, k_B is the Boltzmann constant and T the temperature, which is fixed by the system being in thermal equilibrium with a heat bath. The grand-canonical partition

function is obtained by releasing the constraint of the fixed total number of particle:

$$\mathcal{Z}_{GC} = \sum_N e^{\beta\mu N} \mathcal{Z}_N \tag{2.2}$$

$$= \sum_N e^{\beta\mu N} \sum_{n_k} \exp\left(-\beta \sum_k n_k \varepsilon_k\right) \delta(N - \sum_k n_k) \tag{2.3}$$

$$= \sum_{\{n_k\}} \exp\left(-\beta \sum_k (\varepsilon_k - \mu) n_k\right) \tag{2.4}$$

$$= \prod_k \sum_{n_k} \exp\left(-\beta \sum_k (\varepsilon_k - \mu) n_k\right) = \prod_k \xi_k, \tag{2.5}$$

where

$$\xi_k = \sum_{n_k} e^{-\beta(\varepsilon_k - \mu) n_k} \tag{2.6}$$

and μ is the chemical potential. Let us now consider a system of identical fermions. The Pauli principle allows only a single particle in each quantum state, hence the occupation number n_k can only be either 0 or 1. It follows:

$$\xi_k = 1 + e^{-\beta(\varepsilon_k - \mu)} \tag{2.7}$$

Plugging this result in equation 2.2 we can write the average number of particle in the state k, also known as the Fermi Dirac distribution:

$$\langle N_k \rangle = \frac{1}{e^{\beta(\varepsilon_k - \mu)} + 1}. \tag{2.8}$$

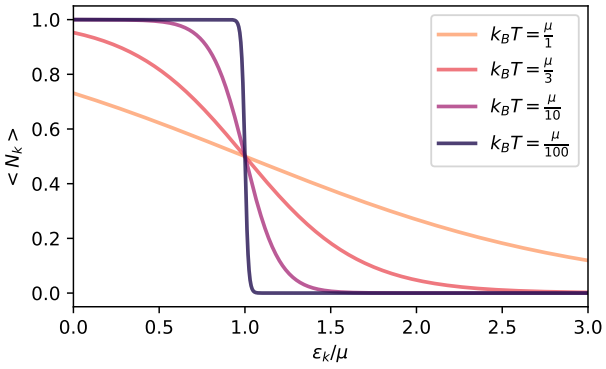

Figure 2.1: Fermi-Dirac distribution for increasing degeneracy parameter μ/k_BT, from lighter to darker color.

Let us now discuss how to calculate the average total number of fermions, $\langle N \rangle = \sum_k \langle N_k \rangle$, in two different cases relevant for this work: the free homogeneous gas and the trapped gas.

Homogeneous gas

For a free Fermi gas, in the volume V, the index k corresponds to the momentum of the particle $\mathbf{p}$. Provided that the volume is large compared to all the other length scales we can replace the summation $\sum_p$ with the integral $V/\hbar^2 \int 4\pi p^2\, dp$:

$$\langle N \rangle = 4\pi \frac{V}{\hbar^3} \int_0^\infty dp\, p^2 \frac{1}{\xi^{-1} e^{\beta\varepsilon_p} + 1} = \frac{V}{\lambda^3} \mathrm{Li}_{3/2}(\xi), \tag{2.9}$$

where $\lambda = \hbar/\sqrt{2\pi m k_B T}$ is the thermal de Broglie wavelength, m the mass of the particle, $\xi = e^{\beta\mu}$ is the fugacity and Li_s is the polylogarithm function[1] of order s.

Trapped gas

The second very relevant case in ultra-cold atoms experiments is the trapped Fermi gas. The density is not homogeneous anymore and increases with the depth of the trapping potential V_{trap}. Assuming this potential to vary slowly on the scale of the de Broglie wavelength, we can take into account the inhomogeneities using the so-called local density approximation (LDA)[22, 23, 24]. The assumption is that thermodynamic equilibrium holds in every infinitesimal volume ΔV of the system. Each volume, described by its position $\mathbf{r}$, is considered as an independent system, characterized by the local chemical potential μ defined as:

$$\mu(\mathbf{r}) \equiv \mu_0 - V_{\mathrm{trap}}(\mathbf{r}), \tag{2.11}$$

where μ_0 is the maximum chemical potential, which is in the center of the trap. Dividing equation 2.8 by the infinitesimal volume we obtain the local density:

$$n(\mathbf{r}) = \frac{4\pi}{\hbar^3} \int_0^\infty dp\, p^2 \frac{1}{e^{-\beta\mu(\mathbf{r})} e^{\beta\varepsilon_p} + 1} = \frac{1}{\lambda^3} \mathrm{Li}_{3/2}(\xi(\mathbf{r})). \tag{2.12}$$

This result will be extremely useful from an experimental point of view because it allows to estimate the temperature of the trapped sample studying its density distribution, which is an experimental observable.

2.1.2 Energy per particle

Contrary to the classical case, because of the Pauli exclusion principle, the energy per particle in a Fermi gas at zero temperature is different from zero. At $T = 0$ all the particles of the gas fill all the energy states from the lowest up to the Fermi energy ε_F. In the homogeneous case, in absence of any trapping potential, the energy is fixed by the total number of particle N and the volume V:

$$\frac{N}{V} = \int_0^\infty d\varepsilon \rho(\varepsilon) n(\varepsilon) \overset{T\to 0}{=} \frac{g_s m^{3/2}}{\sqrt{2}\pi^2\hbar^3} \int_0^{\varepsilon_F} d\varepsilon \sqrt{\varepsilon}, \tag{2.13}$$

[1] The polylogarithm function is defined by the series expansion:

$$\mathrm{Li}_s(\xi) = \sum_{l=1}^{\infty} \frac{(-1)^{l+1} \xi^l}{l^s} \tag{2.10}$$

where we introduced the density of states ρ in thee dimension is defined as:

$$\rho(\varepsilon) = \frac{g_s V}{\sqrt{2}\pi^2}\frac{m^{3/2}}{\hbar^3}\sqrt{\varepsilon}, \tag{2.14}$$

being g_s the spin degeneracy (all the spin states are supposed to be equally populated). In the second passage of equation 2.13 we used the zero temperature limit of the mean occupation number:

$$n_{\varepsilon T\to 0} = \begin{cases} 0, & \text{if } \varepsilon > \varepsilon_F \\ 1, & \text{if } \varepsilon < \varepsilon_F \end{cases}. \tag{2.15}$$

Solving for ε_F one obtains:

$$\varepsilon_F = \frac{\hbar^2}{2m}\left(\frac{6\pi^2}{g_s}\frac{N}{V}\right)^{2/3}, \tag{2.16}$$

from which the energy per particle is:

$$\varepsilon_0 = \frac{g_s m^{3/2}}{\sqrt{2}\pi^2\hbar^3}\int_0^{\varepsilon_F} d\varepsilon\sqrt{\varepsilon}\varepsilon = \frac{3}{5}\varepsilon_F. \tag{2.17}$$

Energy per particle: trapped gas

If we now consider a trapped Fermi gas, we can find the Fermi energy by plugging in Equation 2.13 the proper density of states. In the case of harmonic confinement, characterized by the frequencies $\omega = (\omega_x\omega_y\omega_z)^{1/3}$, an energy state is univocally determined by three quantum numbers n_x, n_y, n_z corresponding to the harmonic oscillator level along the three spatial axes:

$$\varepsilon_{nx,n_y,n_z} = \hbar(\omega_x n_x + \omega_y n_y + \omega_z n_z). \tag{2.18}$$

Moreover, the density of state is [25]:

$$\rho(\varepsilon) = \frac{\varepsilon^2}{2(\hbar\omega)^3}. \tag{2.19}$$

From here, the Fermi energy is given by:

$$\varepsilon_F = \hbar\omega\left(\frac{6N}{g_s}\right)^{1/3} \tag{2.20}$$

2.1.3 Atom number fluctuations

The atom number fluctuations, along with density, is a very important observable. In Chapter 5 we will use this concept both to monitor the temperature and the possible presence of magnetic domains in our system. Here we derive the expression of atom number fluctuations for a non-interacting Fermi gas, which will be used in Section 3.3.8 as a sanity check for our experimental and analysis procedure.
In order to intuitively understand how Fermi statistics affects the atom number variance let us consider the simple picture of a few identical fermions inside a box as shown in

Figure 2.3. Our observable is the number of particle N_v contained inside a smaller volume v (orange square). Because of the Pauli principle, two identical particles can not have the same quantum numbers, therefore, to take this into account, we can qualitatively think that the minimum distance between two fermions should always be bigger than the de Broglie wavelength λ_{dB}. As a consequence, while at high temperature $\lambda_{\mathrm{dB}} \overset{T\to\infty}{=} 0$ all the particle can freely occupy any position in space, at low temperature, when λ_{dB} starts to be of the order of the inter-particle spacing, the particles occupy more evenly the volume of the box. While the mean number $\langle N_v \rangle$ of particles inside the volume v is not affected by the temperature, the number fluctuations depend on it. In the high temperature limit (sketch **A** in Figure 2.3) one finds the classical Poisson statistics [26]:

$$\mathrm{Var}(N_v) = \langle N_v \rangle, \tag{2.21}$$

while in the low temperature one, when the gas progressively becomes a degenerate Fermi gas (sketch **B** and **C**), the atom number fluctuations are reduced [27, 28, 29, 30, 31].

From a purely intuitive point of view, in the high-temperature scenario of panel **A**, if one measures many times the number of atoms inside the volume v, he will find a number ranging freely from 0 to 10. On the other hand, in panel **C**, he will hardly find a number of particles different from 1, 2, or 3, which results in a lower variance of the number of atoms.

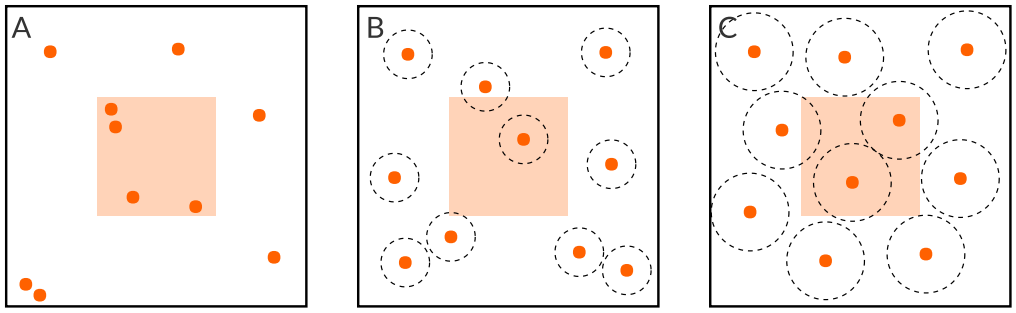

Figure 2.2: Illustration of the number fluctuations reduction in real space due to the Pauli exclusion principle. One can think that two identical fermions cannot be closer than the de Broglie wavelength, sketched as a dashed black circle. In panel **A** we show the classical limit: the de Broglie wavelength is negligible and the particles can occupy any position in space. In the observation volume, sketched as an orange square, the number of particles follows a Poisson statistics [26]. As the temperature drops below the Fermi temperature, as shown in panel **B** and **C**, the particles tend to fill up more equally the volume because of Fermi pressure and the number variance in the observation volume is therefore drastically reduced. In other words, while in panel **A**, for different realizations, the number of particles inside the volume can freely vary from 0 to 10, in panel **C** it is hardly different from 1 or 2. Since the mean number of particles is the same, the ratio between variance and the average number decreases together with the temperature.

In order to quantitatively write the atom number variance of a non-interacting Fermi gas one can start from the definition of variance and of the grand-canonical partition function

(see equation 2.8):

$$\langle(\Delta N)^2\rangle = \langle N^2\rangle - \langle N\rangle^2 = \frac{\mathcal{Z}''_{GC}}{\mathcal{Z}_{GC}} - \frac{\mathcal{Z}'^2_{GC}}{\mathcal{Z}^2_{GC}} \tag{2.22}$$

$$= \left(k_B T \frac{\partial}{\partial \mu}\right) \frac{\mathcal{Z}'_{GC}}{\mathcal{Z}_{GC}} = \left(k_B T \frac{\partial}{\partial \mu}\right)^2 \log(\mathcal{Z}_{GC}) \tag{2.23}$$

$$= k_B T \frac{\partial \langle N\rangle}{\partial \mu}, \tag{2.24}$$

where the apostrophe symbol indicates the derivative with respect to the chemical potential. This result is nothing else but the fluctuation-dissipation theorem [32], which links together temperature and fluctuations, and allows us to use the atom number variance as a thermometer for our gas.
In order to compare this result with experimental observables we first need to define our observation volume V and explicitly differentiate the mean atom number contained in the volume by the chemical potential. The volume V corresponds to a parallelepiped of which the base is a pixel of our imaging (or super-pixel as we will describe in section 3.3) and the height crosses all the atomic cloud. Since our sample is harmonically trapped, the local density is given by equation 2.12, therefore we can write the mean and the variance of the number of atoms in the volume as [33, 34, 35][2]:

$$\langle N^{\mathrm{col}}_{i,j}\rangle = A \int_{-\infty}^{\infty} n_{i,j}(z)\, dz = \frac{k_B T}{\hbar \omega_z} \frac{A}{\lambda^2_{\mathrm{dB}}} \mathrm{Li}_2(\xi_{i,j}) \tag{2.26}$$

and

$$(\Delta N^{\mathrm{col}}_{i,j})^2 = A \int_{-\infty}^{\infty} \frac{(\Delta n_{i,j}(z))^2}{V} dz = \frac{k_B T}{\hbar \omega_z} \frac{A}{\lambda^2_{\mathrm{dB}}} \mathrm{Li}_1(\xi_{i,j}), \tag{2.27}$$

where ω_z is the harmonic frequency of the trap along the imaging direction and the indexes i and j define the position of the pixel (or super-pixel) of area A. One can notice that these two expressions are identical except for the index of the polylogarithmic function. By taking their ratio one can directly link two experimental observables to the fugacity:

$$\frac{(\Delta N^{\mathrm{col}}_{i,j})^2}{\langle N^{\mathrm{col}}_{i,j}\rangle} = \frac{\mathrm{Li}_1(\xi_{i,j})}{\mathrm{Li}_2(\xi_{i,j})}. \tag{2.28}$$

We can now numerically solve this equation for the local temperature T/T_F to find the relation between temperature and fluctuations (plotted in Figure 2.3). In the low temperature limit, the variance per number of atoms increases linearly with the temperature, making the fluctuations a very sensitive thermometer. For $T > T_F$ one recovers the Poisson statistics expected for a classical gas [26].

[2] Here we use the following polylogarithm relation:

$$\int_{-\infty}^{\infty} \mathrm{Li}_s(\xi e^{-x^2})\, dx = \sqrt{\pi}\mathrm{Li}_{s+1/2}(\xi) \tag{2.25}$$

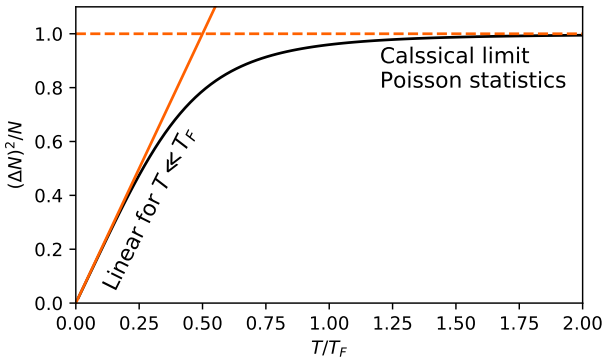

Figure 2.3: Atom number variance as a function of the temperature of the Fermi gas. The curve is obtained by numerically solve equation 2.28. For $T \ll T_F$ the variance grows linearly and can be used as a sensitive thermometer for the gas. For $T \gg T_F$ one recovers the classical statistics, i.e. the Poisson distribution $(\Delta N)^2 = \langle N \rangle$.

2.2 Interacting Fermi gas

Ultra-cold gas experiments are one of the best platforms to study many-body phenomena and the reason is simple: they let us start from what we know and gradually add complications later on, in a bottom-up approach. With interactions, an incredibly rich world emerges: one can study superfluidity and superconductivity in the so-called BEC-BCS crossover, one can bring the physics taking place in neutron stars down to a tabletop experiment in the unitary regime, one can explore the foundation of ferromagnetism from short-range repulsive interactions. In this section we will introduce the scattering problem between fermions and we will discuss how one can exploit the internal hyperfine structure of lithium atoms to experimentally tune the inter-particle interactions via the so-called Feshbach resonance [36, 37].

2.2.1 Introduction to the scattering problem

The collision between two particles can be represented in the center of mass reference frame by the scattering of a single particle of reduced mass[3] μ with the interaction potential V. We can find the stationary states of the problem by solving the equation:

$$(H_0 + V)|\Psi\rangle = E|\Psi\rangle, \tag{2.29}$$

where H_0 is the free-particle hamiltonian, E is the energy and $|\Psi\rangle$ the particle wavefunction. The solution is given by the so called Lippmann-Schwinger equation [38]:

$$|\Psi\rangle = |\Phi\rangle + \frac{1}{E - H_0 + i\epsilon} V|\Psi\rangle, \tag{2.30}$$

which, in coordinate space can be rewritten as [39]:

$$\Psi(\mathbf{r}) = \frac{1}{(2\pi)^{3/2}} \left[e^{i\mathbf{k}\cdot\mathbf{r}} + f(\mathbf{k}, \mathbf{k}') \frac{e^{ikr}}{r} \right], \tag{2.31}$$

[3]The reduced mass μ is defined by $\mu = m_1 m_2/(m_1 + m_2)$, where m_1 and m_2 are the masses of the two particles involved in the collision

where $\mathbf{k}$ is the initial wave vector and $\mathbf{k}'$ the scattered one. We also introduced the scattering amplitude $f(\mathbf{k}, \mathbf{k}')$ which is defined by:

$$f(\mathbf{k}, \mathbf{k}') \equiv -\frac{(2\pi)^2 m}{\hbar^2} \int d\mathbf{r}' \frac{e^{i\mathbf{k}'\cdot\mathbf{r}'}}{(2\pi)^{3/2}} V(\mathbf{r})\Psi(\mathbf{r}) \tag{2.32}$$

This quantity represents the probability amplitude of the outgoing spherical wave as result of an incoming plane wave and fully characterizes the interactions between the two particles. Its modulus squared is the scattering cross section:

$$\frac{d\sigma}{d\Omega} = |f(\mathbf{k}, \mathbf{k}')|^2, \tag{2.33}$$

where Ω is the solid angle. We can simplify this equation by considering the case of elastic scattering and spherically symmetric scattering potential. From the first assumption we know that $|\mathbf{k}| = |\mathbf{k}'|$, therefore, we can reduce the number of variables to just the scattering angle, described by θ and ϕ, and the wave-vector modulus $k = |\mathbf{k}|$. Moreover, the scattering amplitude, which is a priori a vector if one considers the internal degrees of freedom of the atoms, in the limit of elastic scattering, it is a scalar quantity. The second assumption allows us also to exclude the angle ϕ, which describes the direction in the symmetry plane. Both assumptions are well justified in the context of our experiments since the collision cannot change the internal state of each particle (elastic scattering) and the inter-particle potential (Van Der Waals) has spherical symmetry. In the end, we have:

$$\boxed{f(\mathbf{k}, \mathbf{k}') \overset{\text{elastic scattering}}{\rightarrow} f(k, \theta, \phi) \overset{\text{central potential}}{\rightarrow} f(k, \theta).} \tag{2.34}$$

2.2.2 Ultra-cold scattering

Let us now discuss the specific case of scattering between lithium atoms at very low temperature. The inter-particle interactions mostly come from the van der Waals force, which is the result of the mutual dipolar interaction induced by fluctuations and of the short-range Coulomb repulsion between the nuclei. The combination of the two is described by the Lennard-Jones potential:

$$V(r) = \frac{A}{r^{12}} - \frac{B}{r^6}, \tag{2.35}$$

In the context of ultra-cold atoms experiments, this potential is short-range since it becomes completely negligible as soon as r becomes of the order of magnitude of the average inter-particle distance. Moreover, a great simplification of the scattering problem comes from the fact that the collision process occurs at low momentum, corresponding to a wavelength much larger than the range of the inter-particle potential: $r_0 \ll 1/k$. In this regime, since the atomic wave-function is delocalized with respect to r_0, the details of the potential do not influence the collisional properties and, as a consequence, the potential can be modeled as the product of a regularized spatial delta function and a constant coefficient. One can therefore fully characterize the interactions in the system using a single parameter.
In order to understand this concept, it is useful to expand the scattering wave function on a spherical-wave basis. The reason is that only the very first few wave functions of the

basis contribute to the actual scattering wavefunction, drastically simplifying the scattering problem. This expansion can be written as:

$$\psi(\mathbf{r}) = \sum_{l=0}^{\infty} \sum_{m_l=-l}^{l} Y_l^m(\theta,\phi) \frac{u_{k,l,m_l}(r)}{r} \rightarrow \sum_{l=0}^{\infty} Y_l^0(\theta) \frac{u_{k,l}(r)}{r}, \tag{2.36}$$

where $Y_{m_l}^l$ are spherical harmonics and u_{k,l,m_l} is the radial wavefunction. In the second passage we removed the dependence from the azimuthal angle ϕ exploiting the spherical symmetry of the Lennard Jones potential. Plugging this result in the Schrödinger equation 2.29 one finds the effective one-dimensional equation for each radial wave function $u_{k,l}(r)$ separately:

$$\left[\frac{d^2}{dr^2} + k^2 - \frac{l(l+1)}{r^2} - \frac{2m}{\hbar^2} V(r)\right] u_{k,l}(r) = 0, \tag{2.37}$$

The power of the partial spherical-wave expansion comes from the fact that, because of the third term, i.e. the centrifugal term, in the ultra-cold regime all the waves with $l \neq 0$ can be neglected. The reason is that, in this regime, the kinetic energy is much lower than the centrifugal barrier and, in the scattering process, the incoming particle is simply reflected and does not feel the details of the short-range potential (a more rigorous argument can be found in reference [40]). Since the only partial wave affecting the scattering is the s-wave, i.e. the one with $l = 0$, identical fermions do not interact in the ultra-cold regime. Their wave function must, in fact, be antisymmetric, which corresponds to odd values of l.
From now on we will consider only the scattering between two distinguishable fermions, which in our experiment are two lithium-6 atoms in a different hyperfine state. The solution of equation 2.37 for s-wave scattering and large distances, i.e. $r \gg 1/k$, can be written as:

$$u_{k,0}(r) \simeq \sin\left(kr - \delta_0(k)\right), \tag{2.38}$$

where we introduced the s-wave phase shift $\delta_0(k)$. In the low-energy limit the scattering amplitude can be rewritten as [41]:

$$f = \frac{1}{k\cot\delta_0(k) + ik} \simeq \frac{1}{\frac{1}{a} + \frac{r_{\text{eff}}\, k^2}{2} + ik}, \tag{2.39}$$

where we introduced the effective range r_e, which depends on the details of the interaction potential, and the scattering length a which is defined as:

$$a = -\lim_{k\to 0} \frac{\tan\delta_0(k)}{k}. \tag{2.40}$$

It is important to notice that if $|k^2 r_{\text{eff}}| \ll |a^{-1} + ik|$, the so called zero-range limit, the scattering amplitude does not depend anymore by the details of the scattering potential and the inter-atomic interactions are completely characterized by the scattering length and the relative momentum. In the limit of $k \gg a^{-1}$ the gas enters in the so called unitary regime, in which the inter-particle interactions are the strongest allowed by quantum mechanics [42] and are only limited by the collision momentum $f = 1/(ik)$. Finally we can write the s-wave scattering cross section for vanishing momentum ($k \to 0$) as:

$$\sigma_0 = \frac{4\pi a^2}{1 + k^2 a^2}. \tag{2.41}$$

A second important limit is ($|a| \ll k^{-1}$), in which the only relevant parameter for the inter-particle interactions is the scattering length a and we can write the scattering potential as proportional to a delta-like function [42]:

$$V(r) = \frac{4\pi\hbar^2}{m} a\delta(r). \tag{2.42}$$

The bigger is a, the higher is the the interaction strength while its sign defines if the interaction is attractive ($a < 0$) or repulsive ($a > 0$).

2.2.3 The Fano-Feshbach resonance

Up to now, we have completely neglected the internal structure of the two colliding atoms, which, due to the coupling of the nuclear spin to the electron spin via the hyperfine interaction, can drastically change the interaction property thanks to the so-called Fano-Feshbach resonance [6]. The presence of these resonances is an additional tool that makes ^{6}Li an exceptional element for ultra-cold gases experiments. They can, in fact, be exploited to tune the inter-particle interactions at will, from attractive to repulsive, from the weak interacting to the unitary regime.
For alkali atoms, the Feshbach resonance involves the presence of two different scattering potentials, which correspond to the singlet and triplet configuration of the electron spin. These two potential are coupled by the hyperfine interaction, which is not diagonal in the total electron spin of the two colliding atoms [41].

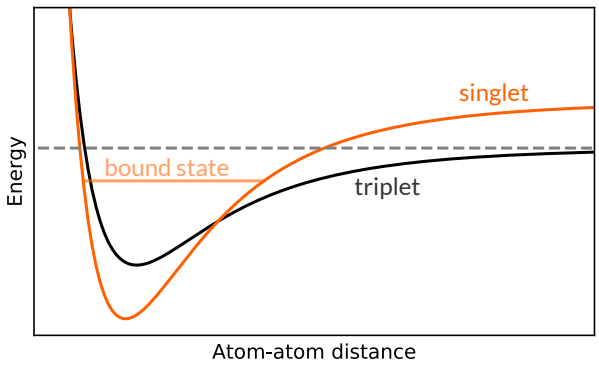

Figure 2.4: Triplet (black solid line) and singlet (orange solid line) scattering potential for two colliding atoms. The energy separation between the singlet bound state and the scattering threshold (dashed gray line) can be experimentally tuned by applying a bias magnetic field. The crossing of these two energies gives rise to a Feshbach resonance, which can be exploited to control the inter-particle interactions in the system.

At low temperature, as soon as the difference between the asymptotic values of the singlet and the triplet potential (see Figure 2.4) becomes much larger then the thermal energy, the continuum states of the former potential stops to be available because of energy conservation and the channel is referred as *closed channel*. The triplet potential is instead called *open channel* since the atoms can enter and leave the scattering region. If the energy of a bound state of the closed channel potential approaches the energy of an incoming particle in the open channel, the two potentials become coupled and the phase-shift $\delta_0(k)$ of the scattered wave is heavily affected giving rise to the so-called Feshbach resonance. Since the

magnetic moment of the singlet and triplet potentials are different, we can experimentally tune the energy splitting between open and close channel by changing a bias static magnetic field and therefore control the inter-particle interactions in the system at will. On a phenomenological level, the effective scattering length close to a Fano-Feshbach resonance can be written as [43]:

$$a(B) = a_{bg}\left(1 - \frac{\Delta B}{B - B_0}\right) \tag{2.43}$$

where a_{bg} is the off-resonance background scattering length, ΔB is the width of the resonance and B_0 its center. The Feshbach resonances between the three lowest lowest hyper-

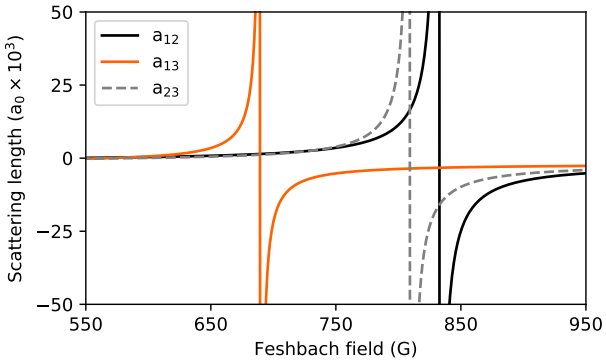

Figure 2.5: Scattering length as a function of the bias magnetic field for different hyperfine mixtures of lithium-6 atoms. Positive values of scattering length correspond to repulsive interactions, negative values to attractive ones. Data adapted from reference [44].

fine states of lithium-6, referred as $|1\rangle$, $|2\rangle$ and $|3\rangle$ are shown in Figure 2.5. These three resonances have an extremely large width, around 300 G, which is a very favorable feature for cold-gases experiments for two main reasons. The first is practical: the larger is the resonance, the easier is to experimentally tune the scattering length since less stability on the bias magnetic field is required. The second is more fundamental: in the case of broad Feshbach resonances the microscopic potential details are completely decoupled from the scattering problem since the effective range of the scattering potential becomes smaller than the Van Der Waals range itself [6].

2.2.4 The attractive and repulsive branches

In the previous section, we have outlined the basic features of the atom-atom scattering potential of a two-component Fermi gas and how we can experimentally control the interaction strength exploiting a Feshbach resonance. Now we want to discuss the consequences of these interactions on the energy spectrum of a many-body system consisting of a fermionic mixture in two different hyperfine states. This is indeed a very challenging problem and still a state of the art theoretical topic. As soon as the interaction parameter $k_F a$ becomes of the order of 1, one can not find an obvious small parameter to characterize the system and any theoretical description becomes extremely difficult [45]. In this section, we introduce the problem in a qualitative way using the toy model developed in Reference [46]. The aim is to intuitively approach the concept of the upper and lower branch without any claim of being quantitatively rigorous.

Let us consider an ultra-cold Fermi mixture of N particles of mass m in two different quantum states labeled as $|i\rangle$ and $|j\rangle$. We introduce the effect of the Pauli exclusion principle by imposing that the particle wavefunction $\phi(\mathbf{r})$ must vanish on the surface of a sphere of radius R, limiting this way to R the minimum distance allowed for the position of two identical fermions [46]:

$$\phi(\mathbf{r})\big|_{|\mathbf{r}|=R} = 0, \tag{2.44}$$

where the value of R can be obtained by comparing the zero-point energy of a particle confined on a sphere of radius R, $E = (N/2)(\hbar^2\pi^2)/(mR^2)$ to the energy of a non interacting Fermi gas $E = (3/5)N\varepsilon_F$, which leads to:

$$R = \frac{\pi}{k_F}\sqrt{\frac{5}{3}} \tag{2.45}$$

In order to solve the Schrödinger equation is advantageous to introduce a second boundary condition called the Bethe-Peierls condition (also known as contact condition):

$$\lim_{r\to 0} \frac{\partial_r(r\phi)}{r\phi} = -\frac{1}{a} \tag{2.46}$$

This condition is equivalent to neglect the effective radius r_{eff} in the expression of the scattering amplitude (see equation 2.39), which is indeed a good approximation for the broad Feshbach resonances of lithium-6. The first two lowest energy solutions of the Schrödinger equation are shown in Figure 2.6 as a function of the dimensionless interaction parameter $-1/(k_F a)$, where k_F is the Fermi wave-vector. As a sanity check for the model

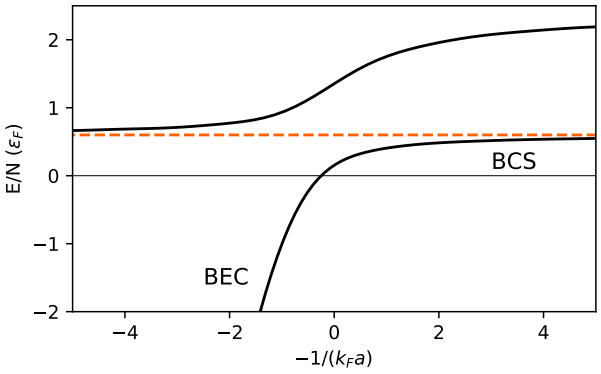

Figure 2.6: First two lowest energy solutions of the energy spectrum of an interacting Fermi gas as derives by the two-body model described in Reference [46] (black solid curves). The ground state is named lower or attractive branch. The first excited state, upper or repulsive. For vanishing interaction strength the energy of a non-interacting Fermi gas is recovered (orange dashed line): $E/N \overset{k_F a\to 0}{=} (3/5)\varepsilon_F$.

one can notice that at the low interaction limit, i.e. $|1/(k_F a)| \gg 1$, the total energy approaches indeed the value expected for a non-interacting Fermi gas: $E/N = (3/5)\varepsilon_F$. The two lowest energy solutions are usually named lower (attractive) and upper (repulsive) branch.

The lower branch

The lower branch is the ground-state of the many-body system. For positive scattering length a two-body bound state emerges with binding energy given by [47]:

$$E_b = -\frac{\hbar^2}{ma^2} \tag{2.47}$$

This atom pair is also known as Feshbach molecule and has a characteristic size of the order of the scattering length. At very low temperature, as soon as the collision energy is much lower than the binding energy, the fermionic nature of the atoms becomes hidden and the molecule starts to behave like a single boson. The gas can eventually form a Bose-Einstein condensate and that's why the $a > 0$ region of the Feshbach resonance is commonly named BEC side. On the other hand, for negative values of the scattering length and sufficiently low temperature, one expects the formation of Cooper-like pairs and a transition to the superfluid BCS state as predicted by Leggett [48]. On top of the Feshbach resonance, $1/(k_F a) = 0$, the so-called unitary limit, the scattering amplitude saturates to $1/k$ and all the relevant scales are set by a single parameter: the Fermi energy ε_F [24]. In this limit, the model predicts a smooth transition between the BEC and the BCS side, the so-called BEC-BCS crossover [49, 43, 50]. The energy of the system is positive but smaller than the non-interacting Fermi gas, indicating an effective attraction.

The upper branch

The first excited state of the many-body system is called the upper or repulsive branch. In this branch the inter-particle interactions are repulsive and short-range, making the system a perfect candidate to study the physics of itinerant ferromagnetism, which describes the properties of a material in which the magnetic moments are not localized in space but are instead mobile. This concept was introduced by Stoner back in the thirties to describe the magnetic behavior of mobile electrons in the conduction band of metallic materials [1]. His physical idea, the Stoner model, describes how, when the screened Coulomb interaction energy between electrons overcomes the Fermi pressure, a ferromagnetic phase is energetically favored over a paramagnetic one.
In the language of ultra-cold atoms the model can be translated in the following example: let us consider a two-component Fermi gas in a trap, with short-range tunable repulsive interaction (for example the $|1\rangle$-$|3\rangle$ ^{6}Li mixture in the repulsive branch) at zero temperature. In the zero interaction limit, the fermions fill all the trap levels up to the Fermi energy ε_F as sketched in the left panel of Figure 2.7. In the opposite limit of extremely large interactions, the two spin components strongly repel with each other and the system minimizes the interaction energy by forming magnetized domains at the cost of increased kinetic energy (right panel of Figure 2.7). The Stoner model predicts a phase transition between these two regimes for a critical value of the interaction parameter $(k_F a)_c = \pi/2$. More recent studies step beyond the mean field approximation and predict the phase transition to occur at $(k_F a)_c \simeq 1$. Between them one can mention the References [51, 52, 53, 54, 55, 56, 57, 58, 11, 59].
While the Stoner idea is very simple, the experimental test of his theory is extremely challenging if not impossible. The main issue is that any strong short-range repulsive interaction is fundamentally based on an underlying attractive potential which supports a weakly bound molecular state [60]. In the ultra-cold language, this statement is equivalent

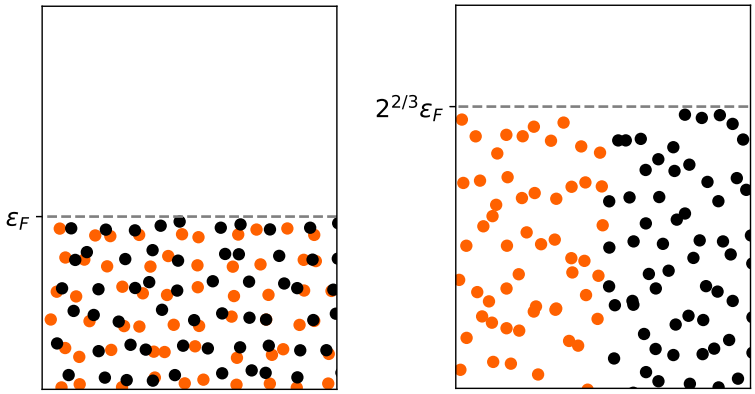

Figure 2.7: Intuitive idea of the ferromagnetic phase transition in the Stoner model. For low repulsive interaction parameter (left panel), the system consists of a paramagnetic mixture of two spin components (black and orange). For strong repulsion (right panel), the different atoms repel with each other and the system minimizes the interaction energy by spatially separating the two spins forming two ferromagnetic domains. The paramagnetic to ferromagnetic phase transition is driven by the competition between the repulsive interaction energy and the Fermi pressure. The data are adapted from reference [46].

to say that the repulsive upper branch is not the real ground state of the system, hence it is unstable to the decay into the lower branch.
From a purely formal point of view, in the Stoner model, the ferromagnetic phase is a proper ground-state of the system and therefore it should not be possible to observe it in ultra-cold gases experiments. On the other hand, real ground states can be rarely observed in Nature, basically, everything is metastable and what really matters is the comparison between the timescale associated with the physical phenomena we are probing and the lifetime of the relative state. Following this idea, the itinerant ferromagnetism can be regarded as a metastable and transitory phase which one can observe by rapidly quenching the repulsive interactions in the system and monitor its response in time. This approach, already exploited in Ketterle's group at MIT [4, 61, 62, 5], is the one we adopted in the work described in this thesis.

Preparation of the repulsive Fermi gas

What do we mean by a quench in the interaction strength? And how can one produce a repulsive Fermi gas avoiding to directly populate the ground state of the system during the cooling procedure? What is the timescale associated with the hypothetic ferromagnetic phase transition, and how it compares with the decay rate of the system into the lower branch?
The main physical process which causes the decay of the upper branch population to the lower one, as we will establish in chapter 5, is the molecular formation via three-body recombination [63]. The process involves three atoms: two of them form a dimer and the third ensures the conservation of energy and momentum, carrying away the excess of kinetic energy. The rate associated with this recombination heavily depends on the shape of the wavefunction of the final molecular state. The lower is the interaction parameter, $k_F a \to 0^+$, the higher is the binding energy of the molecule and the smaller is its size, which qualitatively scales as the scattering length a [47]. The probability associated with

the molecular formation depends on the Frank-Condon overlap between the wavefunctions of the initial and the final states. As shown in Figure 2.8, the process related with the creation of a deeply bound dimer is therefore suppressed because its wavefunction is more and more localized for smaller a and it would require the three free atoms to be at a progressively smaller relative distance to occur. As a consequence, for $k_F a \ll 1$, the

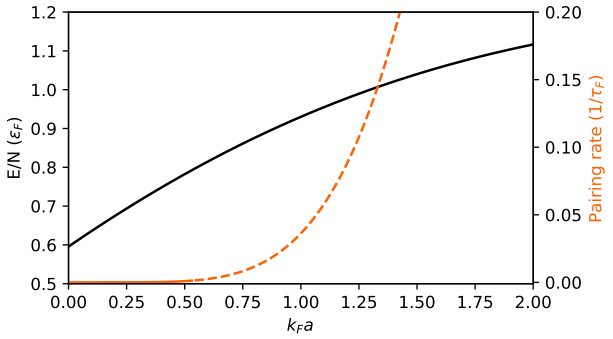

Figure 2.8: Qualitative behavior of the energy per particle in the upper branch (black line) and the pairing rate (orange line). For $k_F a \ll 1$ the weakly repulsive gas is stable and can not decay into the lower branch because the wavefunction overlap between the atomic and the molecular state is negligible. On the other hand, as soon as $k_F a$ becomes of the order of 1, the decay channel from the upper to the lower branch becomes very efficient and the repulsive gas rapidly decays into the ground-state of the many-body system. The pairing rate is expressed in the unit of the inverse of Fermi time calculated using the three-body recombination theory in Reference [63] which is compatible with our measurement shown in chapter 5.

molecular formation is practically suppressed and the upper branch is the lowest accessible energy state of the system. Exploiting this property one can produce a weakly repulsive Fermi gas by cooling the gas at a sufficiently low scattering length (see section 3.1.3).
In order to study the physics of itinerant ferromagnetism one needs to approach interaction strengths of the order of $k_F a = 1$. In this region the size of the Feshbach molecules becomes of the order of the inter-particle spacing and the decay into the lower branch becomes extremely fast, on a timescale of the order of few Fermi times, which is namely the minimum collective response time in interacting fermionic systems [64] and it is defined starting from the Fermi energy as $\tau_F = \hbar/\varepsilon_F$. It is therefore extremely challenging to experimentally quench the interaction parameter in the system in such a short time. One possibility, exploited by the MIT group [4, 61, 62, 5], is to rapidly sweep the Feshbach magnetic field to change the scattering length. Our strategy is instead to adopt a pump-probe scheme, which is widely used in solid-state experiments [12, 13]. We use a series of two radio-frequency pulses to first selectively quench the system into the upper branch and then to probe its out-of-equilibrium dynamics. As we will report in chapter 4 and 5, this technique will allow us to probe the upper branch of the repulsive Fermi gas up to strong coupling and finally study the interplay between the pairing and the ferromagnetic instabilities.

Chapter 3

Experimental setup

In this chapter, I describe the experimental sequence we follow to cool and probe clouds of fermionic ^{6}Li atoms. In the first part, I relate about the experimental setup and the cooling sequence, which allows us to repeatedly produce degenerate non-interacting Fermi gas clouds, the starting point of all the experiments described in this work. Here the basic setup is only quickly sketched and details about the experimental infrastructure can be found in reference [65].
In the second part of the Chapter, I describe the two main probing techniques we employ in our experiments: the radio-frequency (RF) spectroscopy and the absorption imaging. I describe how we employ RF pulses to both calibrate the Feshbach field and to probe the energy spectrum of the gas. Moreover, I sketch our experimental scheme, describing the amplification circuit and the antenna.
I introduce the basics of the absorption imaging in low and high-intensity light conditions and about the calibration of the number of atoms. I give details of the optical system and the acquisition apparatus, describing their features and limitation concerning the spatial resolution, the signal to noise and the acquisition speed. Moreover, I present a dispersive imaging technique, the phase contrast imaging, which allows to produce signals with opposite signs from two different hyperfine spin states. I conclude by illustrating the procedure we employed to extract information about the density and spin density fluctuations and the calibration of the method exploiting the known equation of state of an ideal Fermi gas.

3.1 Production of a weakly repulsive Fermi gas

In this section we will outline our experimental scheme to repeatedly produce cold non-interacting Fermi gas clouds, the starting point of all the experiment reported in Chapter 4 and 5. We will describe the vacuum system and the cooling technique, mostly focusing on the last evaporation stage.

3.1.1 Ultra-high vacuum system

Our vacuum system, sketched in Figure 3.1, consists in the oven, the Zeeman slower and the science chamber. Inside the oven an artificially enriched ^{6}Li sample is heated up to 420° to produce a significant vapor pressure and create an atomic beam which is then collimated by a copper cold finger. The beam passes through the Zeeman slower [41, 66, 67] which decelerates the atoms down to around 60 m/s before they finally enter in the science chamber where they are captured in a magneto-optical trap (MOT)[41, 66, 67]. The

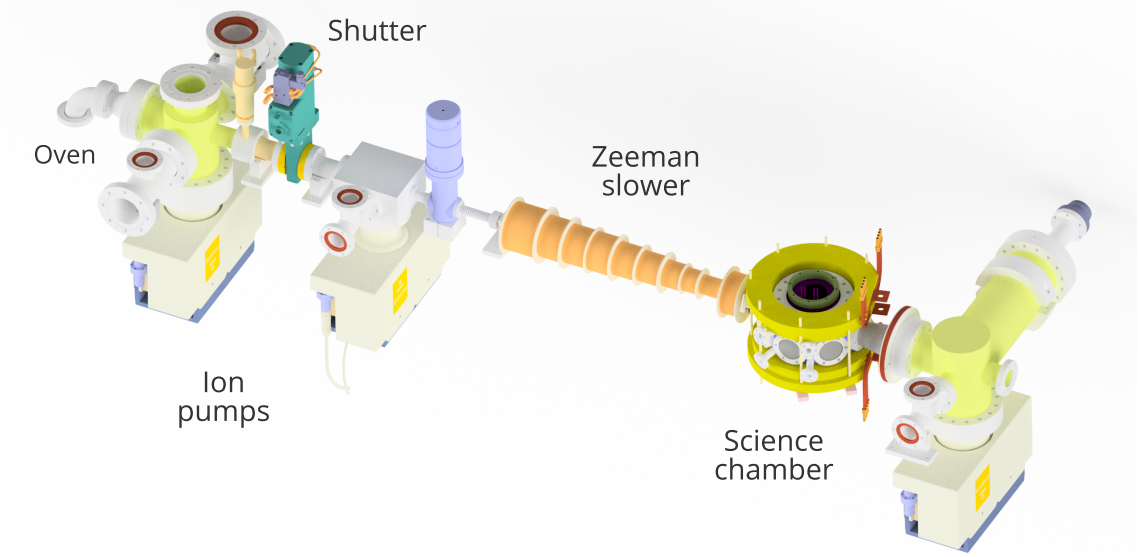

Figure 3.1: Sketch of the Ultra-High-Vacuum system. The lithium vapor is first produced in the oven (not drawn), it is decelerated via the Zeeman slower and it's finally cooled and trapped in the science chamber. The actual experiment takes place inside the science chamber, where the pressure is $\sim 10^{-11}$ mBar.

science chamber is a custom-made octagonal stainless-steel cell from Kimball Physics, on its vertical axis it has two large re-entrant view-ports allowing for a high-resolution imaging system. The pressure in this last segment is kept below 10^{-11} mBar in order to guarantee a sufficiently long lifetime of the atomic sample [68]. The pressure gradient between the oven and the science chamber is achieved by using three Agilent 75 l/s ion pumps and by the non-evaporative getter (NEG) coating applied to the chamber's walls. The detailed description of the ultra-high vacuum system can be found in Reference [65].

3.1.2 Laser sources

For all the experiments reported in this thesis, we used four different light sources: two red lasers for the first cooling stages and for the imaging, and two infrared ones to generate an optical dipole trap (ODT) [41].
The hyperfine structure of ^{6}Li is reported in Figure 3.2, on the left we sketch the D_1 and D_2 lines at zero magnetic field, on the right the magnetic field dependence of the hyperfine structure of the $2^2S_{1/2}$ and $2^2P_{3/2}$ states [69]. The hyperfine splitting of the ground state manifold is 228 MHz large, allowing a single light source for cooling and repumper, both in the MOT and in the D_1 cooling stage. We use two Toptica TA-Pro lasers and two MOPA amplifiers to increase the available power. The two lasers are set to work around 671 nm, locked to the D_1 and D_2 lithium-6 transitions respectively. The fine tuning of the wavelength is controlled by a chain of Acousto-Optical Modulators (AOMs)[65]. The D_2 laser is also used for the imaging, driving the transition from one of the $m_j = -1/2$ states to the $m_j = -3/2$ manifold.
For our optical dipole trap we use two high power infrared beams: the IPG, which is a 1073 nm multi-mode ytterbium fiber laser with a maximum power of 200 W, and the Mephisto, a 1064 nm Nd-YAG laser with a maximum output power of 50 W. The power of these two lasers is set and stabilized by two acousto-optic modulators (AOM) controlled via

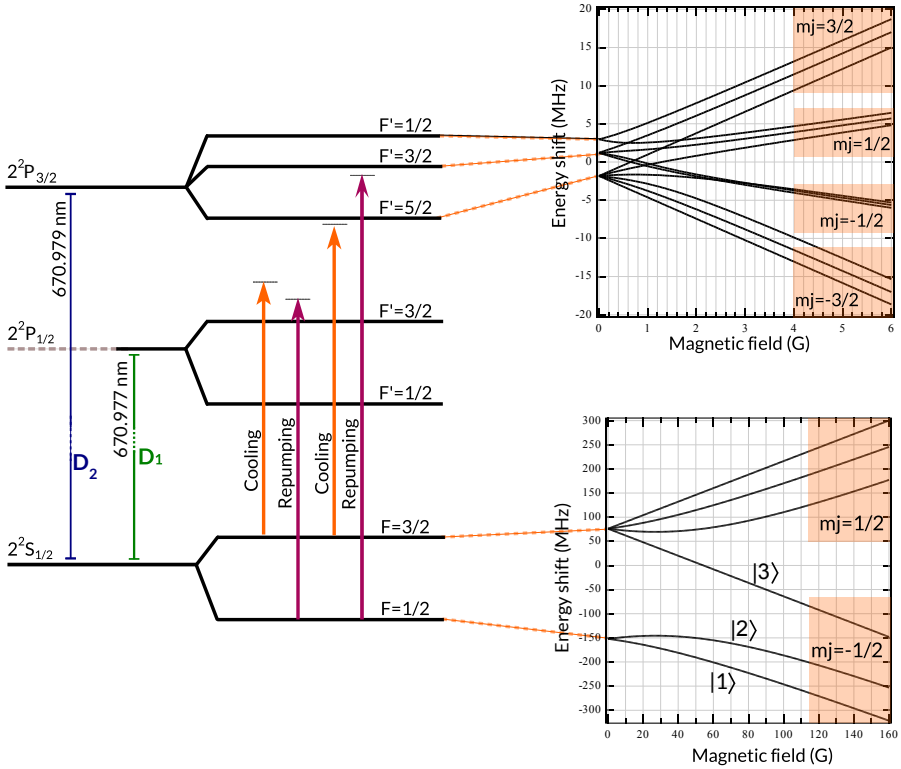

Figure 3.2: **On the left** the D_1 and D_2 line structure of ^{6}Li at zero field. The D_2 line is used for the MOT, the imaging and the optical blasting, while the D_1 for sub-Doppler cooling. The orange arrows represent the cooling transitions while the purple one the repumper, which brings the atoms from the $2^2S_{1/2}F = 1/2$ back to the $F = 3/2$ state. **On the right** the ground state and D_2 line splitting in the presence of a bias magnetic field. The bottom three energy states at high field, labeled as $|1\rangle$, $|2\rangle$ and $|3\rangle$, are the one used during the experiments described in this thesis. In particular, we will exploit the fact that the energy distance between them is of the order of 80 MHz, which allow us to transfer the atomic population from one to the other with radio-frequency radiation.

a feedback loop consisting of a photo-diode (Thorlabs DET36A/M), measuring a fraction of the total light from a transmission leak of a mirror in the laser path, and an analog PID controller (SRS SIM960). As shown in Figure 3.3 both beams are focused in the center of the science chamber and they cross each other with an angle of 14°. They have a similar waist of about 40 μm. In order to increase the trapping volume, the position of the IPG waist is rapidly varied along the y direction by modulating out of phase the amplitude and the frequency of the AOM driving signal, increasing the effective waist of the beam up to 80 μm.

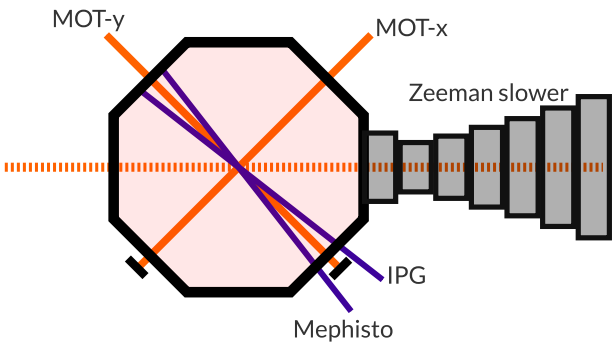

Figure 3.3: Sketch of the cooling lights in the science chamber in a top view. In dashed orange, we show the Zeeman slower beam, in solid red the MOT beams along the x and y direction. In violet, we show the two crossing optical dipole trap (ODT) beam, the IPG, and the Mephisto. They cross each other with an angle of 14° and an angle of 7° and −7° with respect to the y MOT beam.

3.1.3 Cooling to quantum degeneracy

In this section, we will present a short overview of our scheme to produce a degenerate Fermi gas starting from the collimated high-temperature atomic beam quitting the oven. A detailed explanation of each step can be found in Reference [65].

1. A Zeeman slower [41, 66, 67] decelerates the beam from an average velocity of 800 m/s down to around 60 m/s.

2. The slow atomic beam is captured in a magneto-optical trap (MOT) [41, 66, 67] which loads 10^9 atoms with a temperature of $\sim 500\mu$K in about 5 seconds.

3. The MOT is switched off and the gas is cooled down to about 50 μK with an efficient sub-Doppler scheme based on gray molasses which exploits the D_1 transition [70, 71, 72, 73]. This method was tested for the first time on ^{6}Li atoms by our group and its detailed description is published in Reference [74].

4. The sample is transferred into the optical-dipole trap and it is cooled down to quantum degeneracy through evaporative cooling [66].

The evaporation sequence is not straightforward but requires careful control of the interparticle interaction strength involving several stages which are optimized for different temperatures of the gas. As anticipated in the previous Chapter, the interactions are introduced by exploiting a Feshbach resonance between two different Zeeman hyperfine states, which can be tuned via a static bias magnetic field. The field is generated using a pair of large coils in a quasi-Helmholtz configuration, which can produce up to 1000 G and a magnetic curvature up to 5 Hz. The coils consist in 8 vertical and 7 horizontal windings of a hollow core copper wire of section 4.6×4.6 mm. A water flow circulating inside the wire guarantees sufficient cooling to allow a current of about 140 A for 8 seconds without overheating the system. The magnetic field is stabilized with a feedback loop which controls the current by monitoring it with a hall transducer. The precise value of the magnetic field is calibrated using radio-frequency spectroscopy as described in section 3.2.2.
The scheme of the evaporation sequence is the following:

1. The IPG beam is turned on at a power of $\sim 140\,\mathrm{W}$, corresponding to a trap depth of about 1 mK, to maximize the transfer from the MOT. Immediately after, an exponential ramp of $\sim 20\,\mathrm{ms}$ on the laser current brings down its power to $\sim 30\,\mathrm{W}$. Along with this first evaporation section, the Feshbach field is switched on at 832 G, which correspond to the unitary regime of the $|1\rangle$-$|2\rangle$ mixture, making evaporation and thermalization extremely efficient.

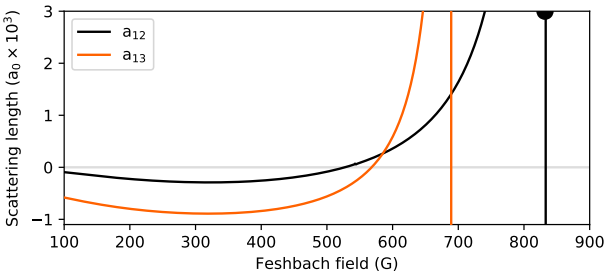

2. After this initial very fast evaporation stage in the IPG, the Mephisto beam is switched on and its power is set to match the IPG one in the waist position. During the rest of the evaporation, we keep fixed the relative power between the beams by checking with the vertical imaging the tilt of the atomic cloud. This way we avoid to excite unwanted oscillation modes which potentially lead to a heating of the sample and to a decreased signal to noise in our measurements given by lower stability of the center of mass position.

3. After about one second of evaporation the molecular ground state of the many-body system becomes accessible leading to the formation of dimers. Since our goal is to prepare a weakly interacting Fermi gas we anticipate this process by sweeping the Feshbach field down to 300 G where ground state of the system is a weakly attractive BCS gas, which is stable.

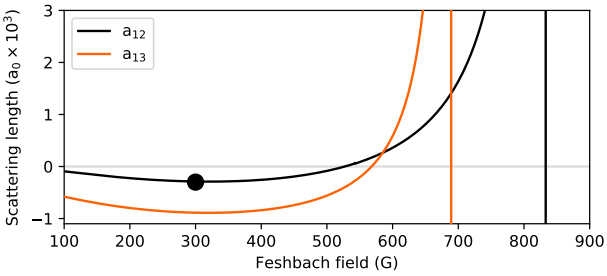

4. After about one more second of evaporation we transfer the state-$|2\rangle$ population to the state-$|3\rangle$ in order to increase the evaporation efficiency since, at 300 G, the scattering length a_{13} is about three times larger than the a_{12}. To efficiently transfer the population we first sweep the field to 585 G, where the scattering length of the $|1\rangle$-$|2\rangle$ coincides with the one of the $|1\rangle$-$|3\rangle$ mixture. Here we perform a radio-frequency (RF) rapid adiabatic passage (RAP) to adiabatically transfer the $|2\rangle$ population into the $|3\rangle$ state. The process consists in a 20 ms RF pulse during which the frequency is swept from 10 KHz below the bare 2-3 energy splitting up to 10 KHz above, which

allows for a transfer efficiency higher than 99%. Finally, the Feshbach field is swept back to 300 G. The reason why we could not pump the system into the $|1\rangle$-$|3\rangle$ mixture before in the evaporation sequence, is because if the temperature is too high we observe decoherence effects during the RAP, probably induced by collisions, which do not allow for high transfer efficiencies.

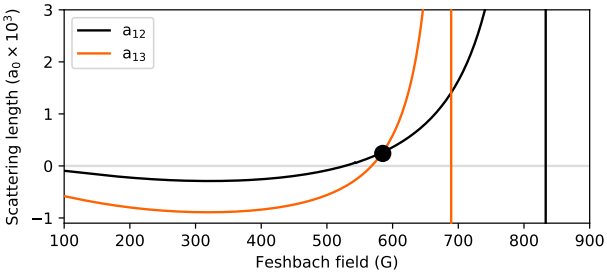

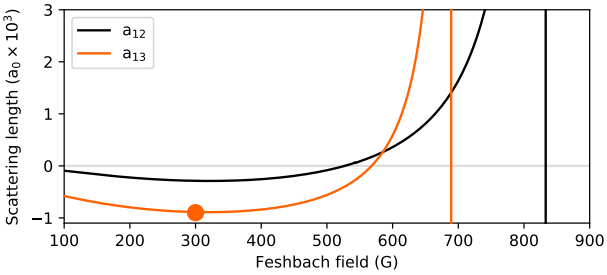

5. At this point the gas is evaporated until the temperature reaches a temperature of about $0.1T_F$, where $T_F = \varepsilon_F/k_B$ is the Fermi temperature. The measurement of the temperature is performed through a polylogarithmic fit (see section 3.3.9) of the density profile of the cloud after we set the Feshbach field to 575 G where the scattering length is negligible and the sample is a trapped non interacting Fermi gas.

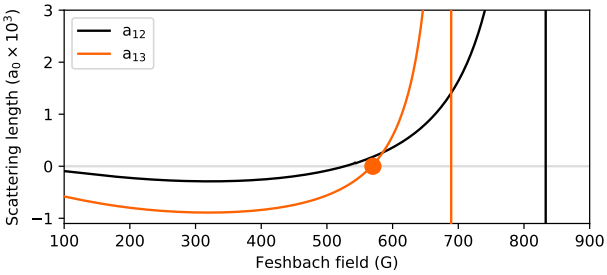

Following this procedure, we are able to produce a degenerate $|1\rangle$-$|3\rangle$ Fermi mixture at a temperature of $0.10(1)\,T_F$ in about 15 seconds. From now on this will be considered as the starting point for all the experiment described in this thesis.

3.2 Radio-frequency spectroscopy

In this section, I will introduce the radio-frequency (RF) spectroscopy as an essential tool to probe the energy spectrum of our system and to quench the Fermi gas out of equilibrium,

into the repulsive upper branch. This is possible because the RF field can couple two hyperfine states of ^{6}Li atoms and allows for a coherent transfer of the population between them. We will start by describing its working principle in a two-level system framework in which two hyperfine levels are coupled by a radio-frequency photon. We will introduce the effect of interactions in the system within a mean field model and the effect of a finite temperature of the system within the framework of the *impact theory of pressure-induced effects on spectral lines* [75]. A more rigorous description, which extends the RF coupling to the case of a many-body system, including beyond mean-field effects, is reported in Chapter 4, where we will connect the spectroscopy signal with the properties of the Fermi polaron. I will conclude this section outlining the RF scheme employed in our experiment, describing our RF sources, amplifiers, and finally the RF antenna design.

3.2.1 Rabi flopping in a two-level system

Let us consider two hyperfine manifolds of the ground states of ^{6}Li, $|i\rangle$ and $|f\rangle$. The Breit-Rabi energy splitting at high magnetic field is of the order of 80 MHz, which corresponds to a wavelength of a few meters, hence the momentum transferred to the atoms in the absorption process is completely negligible and the RF transition can be regarded as a pure spin-flip operation. By setting to zero the energy of the $|i\rangle$ state and to ν_0 the one of the state-$|f\rangle$, we can write down the Hamiltonian which describes the coupling between the RF field and the atom as:

$$H = H_0 + V_{\mathrm{RF}} = \begin{bmatrix} h\nu_0 & 0 \\ 0 & 0 \end{bmatrix} + \frac{\hbar\Omega}{2} \begin{bmatrix} 0 & e^{-i2\pi\nu t} \\ e^{i2\pi\nu t} & 0 \end{bmatrix}, \tag{3.1}$$

where H_0 is the Hamiltonian of the unperturbed atom and V_{RF} is the radiation-atom coupling term. We also introduces the RF frequency ν and the Rabi frequency Ω, which is defined as:

$$\Omega = \frac{\mathbf{d}_{i,f}\mathbf{B}}{\hbar} \tag{3.2}$$

where $\mathbf{d}_{i,f}$ is the magnetic dipole matrix element and $\mathbf{B}$ the magnetic field vector. By

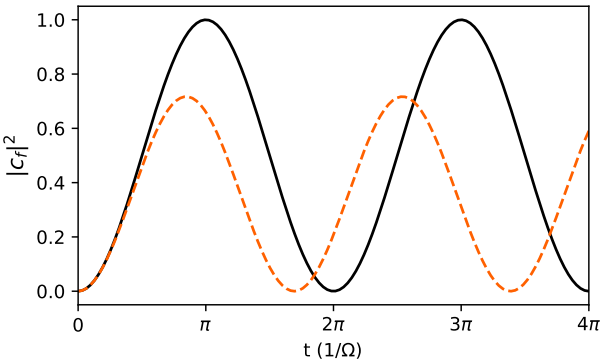

Figure 3.4: Rabi oscillation for zero detuning (black solid line) and for $\delta = \Omega/10$ (orange dashed line). In the presence of a resonant RF field the atomic population oscillates between the state $|i\rangle$ and $|f\rangle$ with a frequency Ω. A RF pulse with a duration of $t = \pi/\Omega$, which completely transfers the population between the first and the second state, is named π-pulse.

working in the so-called rotating frame, we can write the Schrödinger equation as:

$$i\hbar\frac{d}{dt}\begin{bmatrix} c_f \\ c_i \end{bmatrix} = \hbar\begin{bmatrix} 2\pi\delta & \frac{\Omega}{2}e^{-i2\pi t} \\ \frac{\Omega}{2}e^{i2\pi t} & 0 \end{bmatrix}\begin{bmatrix} c_f \\ c_i \end{bmatrix} \tag{3.3}$$

and look for a solution in the form of $|\psi(t)\rangle = c_i(t)|i\rangle + c_f(t)e^{i2\pi\nu t}|f\rangle$. Assuming that at $t = 0$ the system occupies the state $|i\rangle$, the time evolution of the occupation probability of the state $|f\rangle$ if given by:

$$|c_f(t)|^2 = \frac{\Omega^2}{\Omega_{\text{eff}}^2}\sin^2\left(\frac{\Omega_{\text{eff}}}{2}t\right), \tag{3.4}$$

where we define the effective Rabi frequency as $\Omega_{\text{eff}} = \sqrt{\Omega^2 + (2\pi\delta)^2}$. The solution, shown in Figure 3.4, oscillates at the effective Rabi frequency, which has its minimum on top of the resonance ($\delta = 0$). Moreover, the smaller is the detuning, the higher is the transfer efficiency, which reaches 1 for a resonant π-pulse, i.e. for $t = \pi/\Omega$.

3.2.2 Calibration of the Feshbach field

An important use of the RF spectroscopy in our experiment is to finely calibrate the Feshbach magnetic field, which is fundamental to precisely tune the inter-particle interactions. The high field energy splitting between two of the lowest hyperfine states of lithium denoted as $|i\rangle$ and $|f\rangle$ depends on the magnetic field via the Breit-Rabi relation [76] as shown in Figure 3.5. Once one has measured the energy splitting via RF spectroscopy,

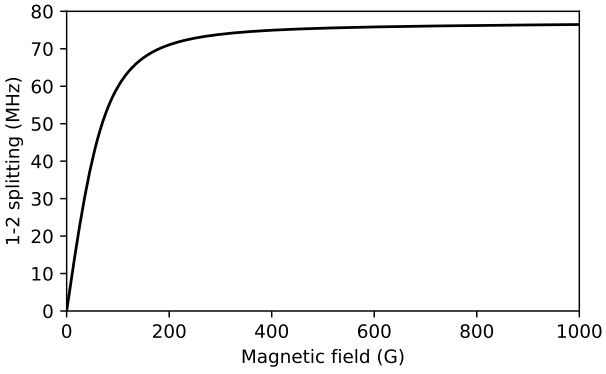

Figure 3.5: Breit-Rabi splitting between the hyperfine levels $|1\rangle$ and $|2\rangle$ of ^{6}Li atoms as a function of the bias magnetic field. Exploiting this relation one can calibrate the magnetic field measuring the energy splitting via radio-frequency spectroscopy.

he can invert this relation and retrieve the value of the magnetic field. In practice, the spectroscopy run consists in irradiating a spin-polarized Fermi gas in the state-$|i\rangle$ with a rectangular radio-frequency pulse slightly shorter than a π-pulse (typically 0.8π), scanning the frequency ν and monitoring the transfer of the atomic population to the hyperfine state $|f\rangle$. In Figure 3.6 we show a typical spectroscopy signal which is fitted using equation 3.4 to extract the value of ν_0. Moreover, its spectral width can be used to verify the stability of the Feshbach magnetic field. The signal plotted in Figure 3.6 has a $1/e^2$ width of $\sim 350Hz$ which corresponds to a maximum fluctuation of the magnetic field of 50 mG: a larger noise would introduce an additional broadening in the spectroscopy signal. Such

stabilization, necessary for our spectroscopy measurements described in Chapter 4 and 5, is achieved controlling the current flowing into through the Feshbach coils via a feedback loop comprising of an analog PID control (SRS SIM960) which drives the current power supply and a Hall probe that measures the current flow.

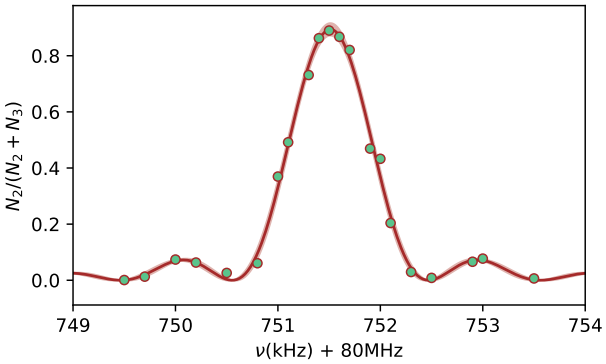

Figure 3.6: Example of a spectroscopy signal around the $|2\rangle$-$|3\rangle$ resonance of a spin polarized Fermi gas. The central frequency is extracted by fitting the signal with equation 3.4. The spectral width of the peak is $\sim 350\,\mathrm{Hz}$ (Gaussian sigma) which corresponds to a stability of the magnetic field of about 50 mG.

3.2.3 Probe of the inter-particle interactions

In the previous sections, we introduced the Rabi dynamics driven by an RF field in an isolated two-level system. We now want to release this boundary and study the effect of interactions in the radio-frequency signal. This will allow us to probe the energy spectrum of the many-body system consisting in a two-component Fermi gas with repulsive interactions, both in the impurity limit in Chapter 4 and in the balanced Fermi mixture in Chapter 5. In order to study this problem let us consider the specific case of lithium atoms interacting through a Feshbach resonance. In Figure 3.7 we show on the left panel the energy splitting between the lowest three hyperfine Zeeman levels named as $|1\rangle$, $|2\rangle$ and $|3\rangle$, and on the right panel the scattering length of the $|1\rangle$-$|2\rangle$ and $|1\rangle$-$|3\rangle$ mixture for a bias magnetic field ranging from 600 and 700 G. In this range the scattering length a_{13} is much larger than a_{12}, hence, for simplicity, we will approximate the latter to zero. Let us now consider the states $|2\rangle$ and $|3\rangle$ as our two level system, while the state-$|1\rangle$ as an external bath which introduces finite interactions to the $|3\rangle$ level. For the moment let us consider the limit of zero momentum collision by approximating the forward scattering amplitude with the scattering length ($\Re[f(k \to 0)] \simeq -a$) and the limit of weak interactions. These two conditions allow for a mean field description of the interaction energy between $|1\rangle$ and $|3\rangle$, which can be expressed as:

$$E_{\mathrm{MF}} = \frac{4\pi\hbar^2 n_1}{m} a, \tag{3.5}$$

where m is the lithium mass and n_1 the state-$|1\rangle$ atomic density. As sketched in Figure 3.8, in the presence of finite interactions in the final state, the radio-frequency driving the transition from state-$|2\rangle$ to state-$|3\rangle$ will be shifted by E_{MF}/h. Experimentally this energy shift can be precisely measured by comparing the resonance peak position of the RF

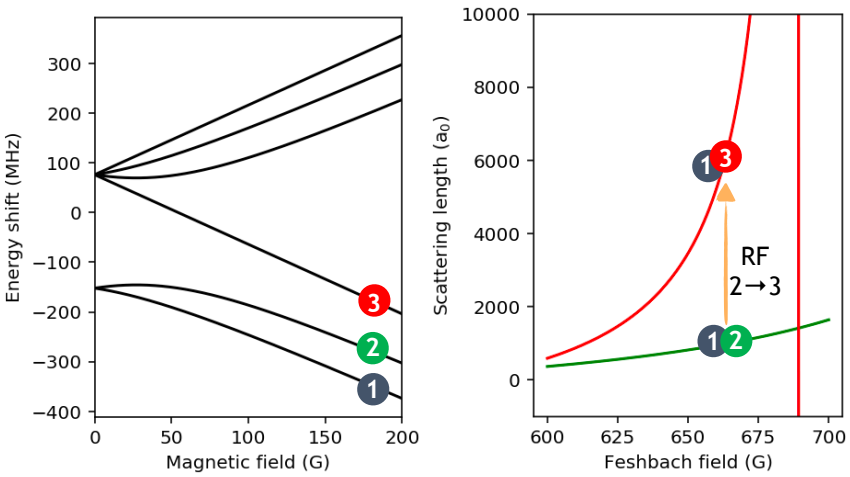

Figure 3.7: **On the left** the Breit-Rabi splitting of ^{6}Li at high magnetic field. We sketch in blue, green and red the lowest three hyperfine Zeeman states ($|1\rangle$, $|2\rangle$ and $|3\rangle$). **On the right** we plot the scattering length of the $|1\rangle$-$|2\rangle$ and $|1\rangle$-$|3\rangle$ mixture around the 1-3 Feshbach resonance. The RF spectroscopy allows to study the 1-3 interactions by probing the $|2\rangle \rightarrow |3\rangle$ transition.

spectroscopy signal in presence and in absence of the state-$|1\rangle$ atoms, i.e. with or without interactions in the final state.

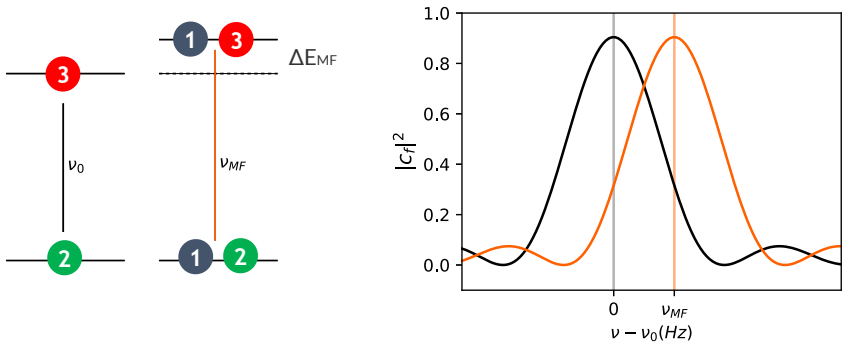

Figure 3.8: Sketch of the effect of mean field interaction on the radio-frequency spectroscopy signal relative to the $|2\rangle \rightarrow |3\rangle$ transition. The final energy level is shifted by the interaction E_{MF} as described in Equation 3.5. This shift can be spectroscopically measured by probing the 2-3 resonance frequencies ν_{MF} and ν_0, in presence and absence of state-$|1\rangle$ atoms respectively. The interactions energy shift is finally obtained as $E_{\mathrm{MF}} = h(\nu_{\mathrm{MF}} - \nu_0)$.

It is important to mention that the same RF pulse used to probe the interactions in the system can be used also to quench the interaction in the fermionic mixture. This will be exploited in chapter 4 and 5 in the so-called pump-probe spectroscopy scheme, which consists of two RF pulses with delay time in between. The first pulse creates a strongly repulsive mixture $|1\rangle$-$|3\rangle$ pushing the system out of equilibrium, while the second probes its evolution as a function of the waiting time.

3.2.4 Effect of finite collision energy on the RF signal

Let us now release the limit of zero-momentum collision introduced in the previous section and discuss the effect on the RF spectroscopy signal given by the finite temperature in the system. We will adopt the framework of the *impact theory of pressure-induced effects on spectral lines* [75] which links the shift and the broadening of the spectroscopy signal with the real and imaginary part of the forward atom-atom scattering amplitude respectively:

$$h\Delta = \frac{2\pi\hbar^2}{\mu}\Re(\langle f\rangle)n, \tag{3.6}$$

$$h\omega = 2\frac{2\pi\hbar^2}{\mu}\Im(\langle f\rangle)n, \tag{3.7}$$

where ω is the full width at half maximum of the spectroscopy signal, μ the reduced mass, n the atomic density and $\langle f\rangle$ the average of f over all the atom-atom collision energies $E_{\text{coll}} = \hbar^2 k_{\text{coll}}^2/(2\mu)$. For s-wave collision the scattering amplitude can be written as (see section 2.2.1):

$$\frac{f(k_{\text{coll}})}{a} = -\frac{1}{1+(k_{\text{coll}}a)^2} + i\frac{k_{\text{coll}}a}{1+(k_{\text{coll}}a)^2}. \tag{3.8}$$

We can explicitly rewrite the RF shift and its broadening normalized by the Fermi energy as:

$$\frac{h\Delta}{\varepsilon_F} = -\frac{h}{\varepsilon_F}hn\frac{2}{m}\frac{a}{1+(ka)^2} = -\frac{4}{3\pi}k_F a\frac{1}{1+\frac{\varepsilon_{\text{col}}}{\varepsilon_{\text{b}}}}n \tag{3.9}$$

and

$$\frac{h\omega}{\varepsilon_F} = -\frac{h}{\varepsilon_F}hn\frac{2}{m}\frac{ka^2}{1+(ka)^2} = -\frac{8}{3\pi}k_F a\frac{\sqrt{\frac{\varepsilon_{\text{col}}}{\varepsilon_{\text{b}}}}}{1+\frac{\varepsilon_{\text{col}}}{\varepsilon_{\text{b}}}}n, \tag{3.10}$$

where we introduced the mean collisional energy $\varepsilon_{\text{col}} = \hbar^2k^2/m$ and the binding energy $\varepsilon_{\text{b}} = \hbar^2/(ma^2)$. Moreover, we used the definition of Fermi energy $\varepsilon_F = \hbar^2k_F^2/(2m)$ and the Fermi wave vector $k_F = (n6\pi^2)^{1/3}$. In Figure 3.9 we plot the ratio between the real and imaginary part of the forward scattering amplitude and the scattering length, which is the relative correction to the mean-field radio-frequency signal concerning the resonance shift and the spectral broadening respectively, as a function of the collision energy. This plot qualitatively describes the effect of a finite temperature in the spectroscopy signal. A higher temperature, corresponding to a higher collision energy, slightly decreases the interaction energy shift and increases the width of the spectroscopy signal. In Chapter 5 we will exploit this latter property to exclude the presence of finite momentum collision effects in our spectroscopy measurements.

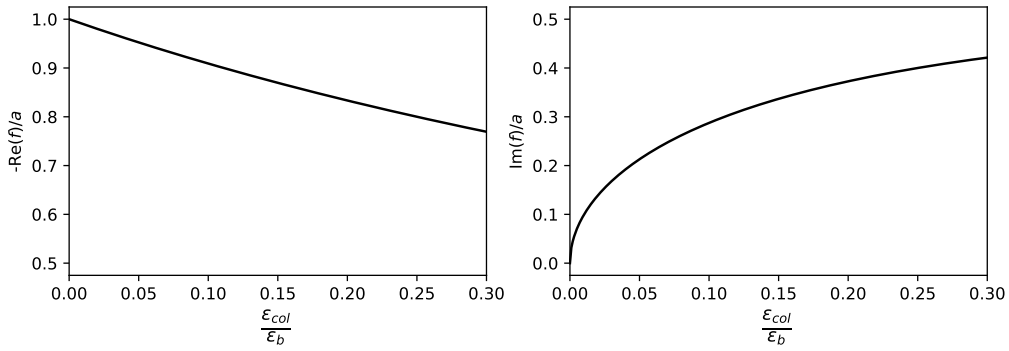

Figure 3.9: Real (left panel) and imaginary (right panel) part of the forward scattering amplitude as a function of the collision energy, which correspond to the relative change of the energy shift and broadening of the spectroscopy signal respectively.

3.2.5 Radio-frequency scheme

In the previous sections, we introduced the basics of the interactions between our atomic sample and radio-frequency pulses, now we will describe how we experimentally generate and control the field. The RF signal is initially generated from two different oscillator sources, an HP 83752A synthesized sweeper and a DDS AD9958. Having two distinct sources is fundamental for the pump-probe spectroscopy protocol which requires a sequence of two pulses within a small time window and different frequencies. Since we only have one antenna, the two signals are combined via an RF mixer. After the mixer a variable attenuator (Mini-circuits ZX73-2500S+) allows us to switch on and off the RF output signal via a TTL channel of our control board DIO64. This is fundamental to precisely control the duration of the pulses and the delay between them. The signal is then amplified by a Mini-circuit amplifier ZHL-100W-GAN+ directly connected to a circular antenna consisting in a single wire loop with a diameter of 5 cm and 1 mm thickness. The antenna is placed close to the atomic sample (about 3 cm), inside the lower reentrant window of our science chamber, in order to maximize the atom-field coupling. In order to maximize the output RF field generated by the antenna, we built an impedance matching circuit, shown in Figure 3.10, consisting in a resonator centered on a frequency of about 80 MHz, the hyperfine Zeeman splitting between the states $|2\rangle$ and $|3\rangle$ at high field ~ 600 G (close to the $|1\rangle$-$|3\rangle$ Feshbach resonance). The matching condition is obtained by changing the

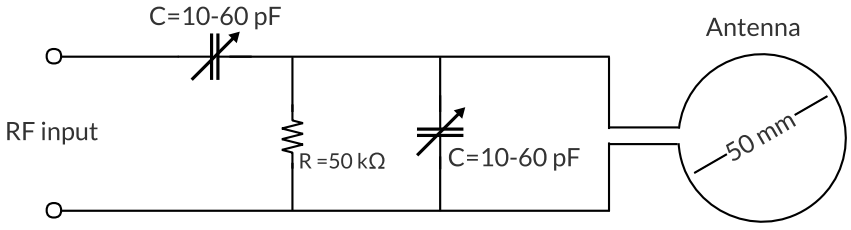

Figure 3.10: Impedance matching circuit of the RF antenna consisting of a 5 KΩ resistor and two compensators with a capacitance range between 10 and 60 pf. The antenna consists of a single loop of copper with a diameter of ~ 50 mm and a section of 1 mm.

capacitance of two compensators and looking at the absorption as a function of the signal frequency with a network analyzer. The absorption profile of our antenna, placed close to

the science chamber, is shown in Figure 3.11. One can see that we achieved a coupling efficiency better than 90% (−20 dBm) in a frequency range between 78 and 83 MHz, which corresponds to the energy splitting between the state-$|2\rangle$ and state-$|3\rangle$ for a bias magnetic field ranging from 600 to 700 G. The efficiency will be relevant for the experiments described in chapter 4 and 5, where we will need the strongest possible RF field to maximize the Rabi frequency between these two states.

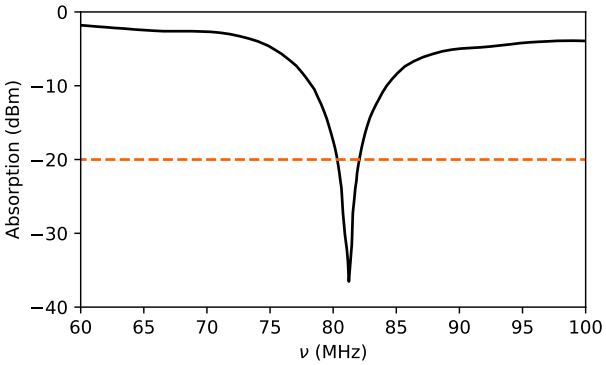

Figure 3.11: Absorption of the RF antenna as a function of the signal frequency. The matching circuit is optimized by acting on the two compensator to be resonant around 80 MHz, which is the ^{6}Li hyperfine Zeeman splitting between the states $|2\rangle$ and $|3\rangle$ for a bias field of about 600 G. The final coupling is better than 90% (−20 dBm as marked by the orange dashed line) in the frequency range between 78 and 83 MHz.

3.3 Imaging

The imaging is the bridge that allows us to gather information about the gas sample contained in our vacuum chamber. In ultra-cold atoms experiment the most important observable is the density: $n(x, y, z)$. In this section I will describe our imaging system and present different imaging techniques that we exploited during the work described in this thesis. I will start introducing the basics of the absorption imaging, the most common imaging technique in ultra-cold atoms experiments. I will describe its calibration protocol for probing atomic cloud with high intensity light. Then, I will present a dispersive imaging technique which allow to probe two hyperfine states in the same imaging shot. Finally I will describe the procedure we followed to measure the atom number fluctuations in our atomic sample and some technical setting to the image acquisition sequence we adopted to improve the signal to noise ratio in the measurement.

3.3.1 Imaging apparatus

Our setup has two different imaging paths, one along the horizontal and one along the vertical direction. The former has a wide field of view given by a low magnification $M = 0.49(2)$ which allows to image the full size of the cloud trapped in the MOT. The imaging light has a linear polarization perpendicular to the quantization axis of the Feshbach field which reduces the atomic scattering cross section by a factor of two. The setup consists in two lenses in a $2 - f$ telescope configuration, the first one has a focal length of 150 mm and 1 inch diameter, the second one has a focal length of 75 mm and a 2 inches diameter.

The light profile is finally probed with a Stingray CCD camera[1]. As sketched in Figure

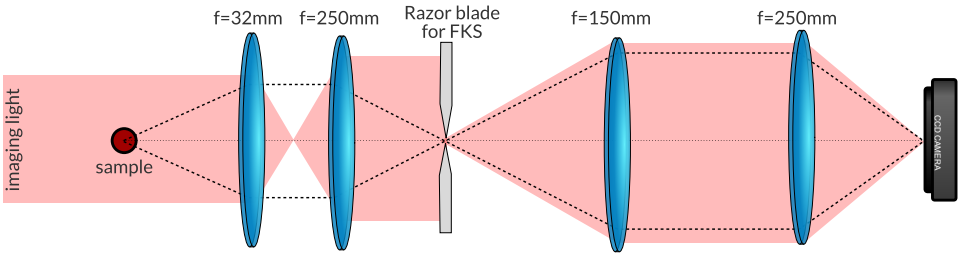

Figure 3.12: Sketch of the vertical imaging $4-f$ telescope which focuses the image of the atomic cloud on the CCD camera chip with a magnification of $M = 13.0(2)$ and a resolution of about $1.5\,\mu$m. The razor blades in the middle of the four lenses limit the light reaching the CCD to a small rectangle containing the atomic cloud, which is essential to acquire several images within a small time delay exploiting the fast-kinetic acquisition mode (FKS) of our CCD as described in section 3.3.5.

3.12 , the vertical imaging system, along the z-axis, consists in a $4-f$ high resolution telescope which consists in four 2 inches lenses with focal lengths of 32, 250, 150 and 250 mm respectively (from the science chamber to the CCD camera). The first lens has a high numerical aperture of around 0.61 which allows us to achieve a resolution of about $1.5\,\mu$m. The imaging light is finally probed with an Andor IXon3 EMCCD camera[2] which is cooled down to $-70°$ to drastically reduce the dark count noise. As shown in Figure

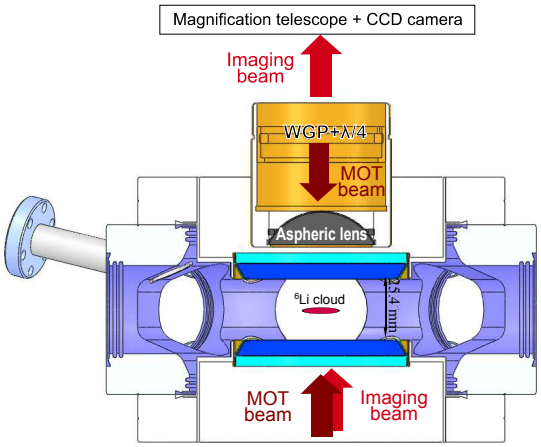

Figure 3.13: The MOT beam and the imaging beams share the same path entering the science chamber from the bottom window. The two beams are divided by the combination of a wire grid polarizer (WPG) and a $\lambda/4$ wave-plate which reflects the σ_+ polarized MOT light and let through the σ_- polarized imaging one. The imaging light is collected by an aspheric lens and imaged on the CCD camera chip.

3.13, the vertical MOT beam and the imaging light follow the same path, hence, in order to separate them, we exploit a wire-grid polarizer plus a $\lambda/4$ wave-plate to reflect σ_+ polarized

[1] AVT Stingray F-145B. 1388 (H) × 1038 (V) resolution. $6.45\,\mu$m squared pixel.

[2] Andor iXon3 X-9260 CCD camera. Model number CCD201-20-1-179. 1024×1024 resolution. $13\,\mu$m squared pixel.

MOT light and let through the σ_- polarized imaging one. The overall magnification of the setup is $M = 13.0(2)$.

3.3.2 Absorption imaging

Absorption imaging consists in imaging the shadow of an atomic sample illuminated by resonant light. The atoms absorb the incoming radiation causing a reduction of the transmitted intensity. The "shadow" of the atoms is finally imaged on a CCD chip. To model this process let us consider the atoms as two-level systems coupled with the radiation field of the imaging light. The relevant parameters are:

- ω_0: the atomic resonance (angular) frequency, corresponding to the energy splitting of the two-level system ($\hbar\omega_0$).
- Γ: the linewidth of the atomic transition, corresponding to the spontaneous emission rate.
- δ: is the detuning in half linewidths,

$$\delta \equiv \frac{\omega - \omega_0}{\Gamma/2}. \tag{3.11}$$

- $s = I/I_{\text{sat}}$: the saturation parameter, i.e. the ratio between the imaging field intensity and the transition saturation intensity, defined as:

$$I_{\text{sat}} = \frac{\hbar\Gamma\omega_0^3}{12\pi c^2} \tag{3.12}$$

The fluorescent power, i.e. the rate of energy emitted by a sample of N atoms can be written as [67]:

$$P_F = N\hbar\omega_0 \frac{\Gamma}{2} \frac{s}{s+1} \frac{1}{1 + \left(\frac{\delta}{\sqrt{1+s}}\right)^2} \tag{3.13}$$

This relation can be obtained by integrating the Maxwell-Bloch equations (or optical Bloch equations) where the spontaneous emission term is introduced "by hand" as decay from the upper to the lower level [66]. It is important to notice that without the relaxation process given by the spontaneous emission, the atoms would perform Rabi oscillations between the ground and the excited states, therefore being on average transparent to the imaging beam. In order for the atoms to cast a "shadow", it is necessary for the Rabi oscillation to be dumped during the imaging pulse. This condition is easily fulfilled in ultra-cold atoms experiment: the damping time t_D is given by the inverse of the spontaneous emission rate of the atomic transition Γ, e.g., for lithium $t_D \sim^{-1}\sim 1/(2\,\pi\,6\text{MHz}) \sim 25\text{ns}$, while the imaging pulse length is always $\geq 1\mu$s.
From equation 3.13, exploiting the conservation of energy, one can calculate the drop of the laser intensity while the beam travels through the atomic medium. In a distance dz traveled in the gas, the light intensity decreases by dI:

$$dI = -\frac{1}{A} P_F(dz) = -\hbar\omega_0 \frac{\Gamma}{2} \frac{s}{1+s} \frac{1}{1 + \left(\frac{\delta}{\sqrt{1+s}}\right)^2} n\, dz, \tag{3.14}$$

where A is the laser beam cross section and n is the atomic density. Solving this equation one can link the intensity drop to the atomic density, which is exactly the purpose of the imaging. In the special case of low imaging light intensity ($s \ll 1$) and resonant frequency ($\delta = 0$) the equation 3.17 can be rewritten as:

$$dI = -\hbar\omega_0 \frac{\Gamma}{2} \frac{I}{I_{\text{sat}}} n \, dz = -I \frac{3\lambda_0^2}{2\,\pi} n \, dz, \tag{3.15}$$

Starting from this result it is possible to measure the density profile of an atomic cloud. In the following, I will describe the most common way to measure it experimentally.

3.3.3 Absorption imaging: the experimental implementation

Let us now consider a cloud with a density distribution $n_{3\text{D}}(x, y, z)$ and a resonant imaging beam propagating along the z direction with an intensity profile given by $I_0(x, y)$. The density profile is integrated along the direction of the imaging beam and the only measurable quantity is the integrated density profile:

$$n_{2\text{D}}(x, y) \equiv n(x, y) \equiv \int_{-\infty}^{\infty} n_{3\text{D}}(x, y, z) dz \tag{3.16}$$

The intensity profile of the imaging beam after the atomic cloud $I(x, y)$ can be obtained integrating the equation 3.15 and it is given by the Lamber-Beer law:

$$I(x, y) = I_0(x, y) \mathrm{e}^{-\sigma_0 n(x,y)}, \tag{3.17}$$

where we introduced the absorption cross section $\sigma_0 = \hbar\omega_0\Gamma/(2I_s)$. The density profile is therefore given by:

$$n(x, y) = \frac{1}{\sigma_0} \log\left(\frac{I_0(x, y)}{I(x, y)}\right) \tag{3.18}$$

The intensity profiles $I(x, y)$ and $I_0(x, y)$ can be measured using a CCD camera with two different imaging pulses: the first with the atomic cloud and the second without it. The CCD actually measures the number of photons that reach each pixel, therefore the intensity is obtained by:

$$I(x, y) = C(i, j) \frac{\hbar\omega_0}{g} \frac{1}{M \, A_{\text{px}} \, t_{\text{pulse}}}, \tag{3.19}$$

where C are the CCD counts, M is the magnification of the imaging system, $A_{\text{px}} = L_{\text{px}}^2$ is the area of the CCD pixel of dimension $L_{\text{px}} \times L_{\text{px}}$, t_{pulse} is the duration of the imaging light pulse and g is the CCD gain, i.e. the conversion between number of photons and counts (see section 3.3.8). The CCD pixel indexes i and j correspond to a position in the object plane given by the scaling $x \to i \times L_{\text{px}}/M$ and $y \to j \times L_{\text{px}}/M$. Finally, the integrated density profile can be obtained as:

$$n(x, y) \equiv n\left(\frac{i \times L_{\text{px}}}{M}, \frac{j \times L_{\text{px}}}{M}\right) = \frac{1}{\sigma_0} \log\left(\frac{C^2(i, j) - C^{\text{bg}}(i, j)}{C^1(i, j) - C^{\text{bg}}(i, j)}\right), \tag{3.20}$$

where C^1 are the CCD counts with the atom cloud, $\propto I$, and C^2 without the atom cloud, $\propto I_0$. We also introduced C^{bg}, that corresponds to a CCD acquisition without imaging

light. C^{sat} is called background or the dark image and it is necessary to remove the offset, present in every acquisition, mainly introduced by the dark current, i.e. the presence of thermal electrons accumulating in the CCD[3]. This result is valid for resonant light and low saturation parameter ($s \ll 1$) which is the relevant case concerning our horizontal imaging. In the next sections I will describe how to obtain the density profile when these two conditions are not fulfilled.

3.3.4 High intensity imaging

Working in the regime of low imaging light intensity is not always feasible: the higher are the optical thickness of the atomic sample and the magnification of the imaging system, the higher is the imaging intensity required to keep constant the signal to noise ratio of the measured density profile [77].
In order to obtain the integrated density profile for $s \geq 1$ one has to integrate directly the equation 3.17. The result is [78]:

$$n(x,y) = \sigma_0 \left[\log\left(\frac{C^2(i,j) - C^{\text{bg}}(i,j)}{C^1(i,j) - C^{\text{bg}}(i,j)} \right) - \frac{C^2(i,j) - C^1(i,j)}{C^{\text{sat}}} \right], \tag{3.21}$$

where we introduced C^{sat} that are the measured CCD counts for an imaging beam with an intensity $I = I_{\text{sat}}$. In order to find these constant several strategies are available. One is to estimate the light intensity in the position of the atomic cloud, which can be done either measuring the power and waist of the imaging beam or the light intensity on the CCD chip and the magnification of the imaging system. Both these methods end up with a big uncertainty on the value of C^{sat}. In the first case, most of the experimental error comes from the determination of the total beam power using a power-meter, while in the second from the estimation of the light losses of all the optical elements between the atoms and the CCD chip. Another possible method, which ends up to be the most precise for our setup, is to calibrate the saturation intensity directly with the atomic cloud: first of all, we optimize the evaporation sequence to prepare an atomic sample with lowest possible shot-to-shot total atom number fluctuations. Then we measure the number of atoms using our low-resolution horizontal imaging, which has a very low magnification ($M = 0.49$) and does not suffer from saturation problem since the imaging intensity is much lower than I_{sast}. Once we know the total atom number we switch to the vertical high-resolution imaging. At this point, as we can see in the left panel of Figure 3.14, if we do not use the high-intensity correction to calculate the optical density, as soon as we change the imaging intensity, the OD drastically changes. Darker colors correspond to low imaging light intensity, the optical density is big and the signal very noisy. As soon as we increase the imaging light power, the OD drops and the signal gets cleaner.

[3]Some CCD camera, like the Andor iXon3 we use, add an artificial baseline or bias level to the output signal to ensure that the displayed signal level is always a positive number of counts. The C^{bg} is also needed to subtract this offset.

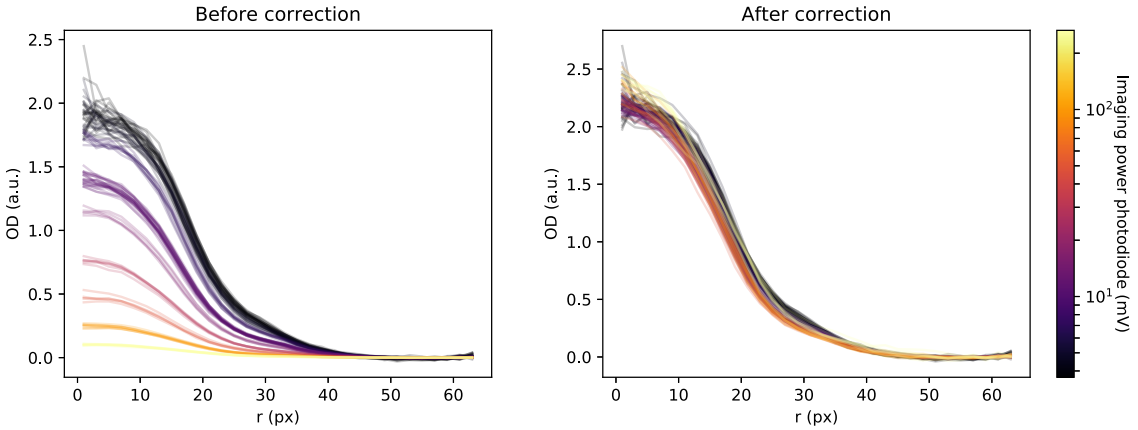

Figure 3.14: **On the left** the azimuthal average many optical density profiles calculated without the correction for $s \geq 1$ (using equation 3.20). Every line corresponds to a different experimental run where the imaging beam intensity has been changed by two orders of magnitude. Darker colors correspond to lower intensity: the optical density profile is saturated near the center of the atomic cloud, where the optical density is higher, and the signal to noise ratio is lower. Lighter colors correspond to higher imaging light intensity: the optical density profile has a better signal to noise but its value is underestimated because of the saturation of the atomic transition. **On the right** the optical density is calculated on the same images using the linear correction for high imaging intensity (equation 3.21). The optical density profiles collapse one on top of the others, i.e. they are independent on the imaging light intensity.

Since the atom number in the atomic cloud is constant, the measured optical density must be constant as well. We can, therefore, find the best value of C^{sat} as the one that minimizes the difference between the optical densities obtained from different imaging intensities.
In practice, we acquire several images of the atomic sample with j_{tot} different imaging intensities I_j, ranging from $\sim 1\%$ of the saturation intensity to $\sim 50 I_{\text{sat}}$. We then compute the optical density using equation 3.21, using different values of C^{sat}. We azimuthally slice each image obtaining the radial optical density profile $OD(r, C^{\text{sat}}, I_j)$, where r represents the distance from the center of the cloud[4]. We finally calculate the variance of each slice for the different intensities:

$$\mathrm{V}(r, C^{\text{sat}}) = \frac{1}{j_{\text{tot}}} \sum_{j=0}^{j_{\text{tot}}} (OD(r, C^{\text{sat}}, I_j) - \langle OD(r, C^{\text{sat}}) \rangle_{I_j})^2, \tag{3.22}$$

where the angle brackets $\langle \cdot \rangle_{I_j}$ represent the mean over all the different imaging intensities I_j. In the left panel of Figure 3.15 we plot the variance $\mathrm{V}(r, C^{\text{sat}})$ for five different values of C^{sat}. As one can notice, between the five C^{sat} values tested, 31.2 is the one which better minimizes the optical density variance. In order to quantitatively find the best value for C^{sat}, we define as an optimization metric the average of the variance over all the azimuthal slices. By minimizing this value we finally find the optimal C^{sat} value as showed in the right panel of Figure 3.15.
Using this result in equation 3.21 we observe a very weak dependence of the optical density to the imaging light intensity, which is exactly the purpose of the calibrations. As we can

[4]Since the cloud is cigar-shaped, in order to perform the azimuthal average, we need to squeeze the image along the x direction to obtain spherically symmetric density distribution.

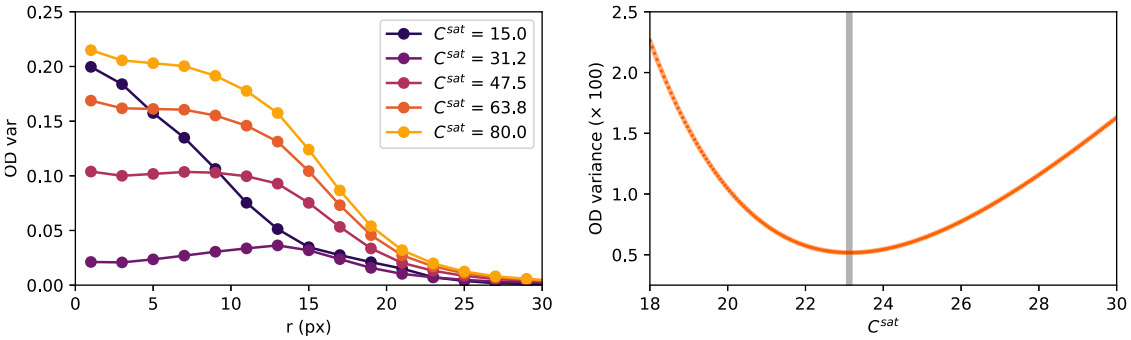

Figure 3.15: **On the left** panel we show the variance of the optical density for each azimuthal slice of the atomic cloud for 5 different values of C^{sat}. **On the right** panel we plot the average of the variance over all the slices as a function of C^{sat}. The best value is the one that minimizes the variance.

see in the right panel of Figure 3.14, using the optimal value for C^{sat}, the optical densities corresponding to different imaging intensities collapse one on top of the other.

3.3.5 Experimental imaging sequence

In the previous sections, we described the main aspects of the absorption imaging and we have seen how to obtain the column density of the atomic cloud by taking three different images:

1. C^1 (atom image), corresponding to a resonant imaging pulse in the presence of the atoms.
2. C^2 (reference image), identical to the first pulse but without the atoms.
3. C^{bg} (background or dark image), the background obtained with no imaging light to record the dark noise of the CCD.

The calculation of the optical density involves taking the ratio between C^1 and C^2, therefore it is very important for the intensity profile of the imaging beam to be as flat and constant in time as possible in order to avoid artifacts in the final image. Since the imaging light is coherent, a common source of problems is the presence of fringes in the beam profile due to the self-interference with some unwanted reflections by one of the optical element of the setup. This causes the presence of stripes in the beam profile and, if mechanical vibration of the setup moves the beam between the two images, these fringes appear also in the optical density. The typical frequency of these mechanical vibrations is in the KHz range, hence it is very important to take the first two images with a small time delay between them, possibly $\Delta t \ll 1\,\text{ms}$. On the other hand, this time has to be sufficiently long to allow us to get rid of the atomic cloud before acquiring the reference image, which is achieved by either waiting for the atoms to fly away or by changing the bias magnetic field and detune the atomic transition from the imaging light. We usually employ the latter option because it is slightly faster.
In practice, the delay time bottleneck is typically given by the frame-rate of the CCD camera, which in our case is on the Hz timescale when we use the full CCD chip. Since this timescale is way to slow for our purpose we employ the so-called Fast Kinetic Series

(FSK) acquisition mode, which allows taking a sequence of a few images with a delay time on the order of $\sim 200\,\mu$s at the price of using a smaller portion of the CCD chip [79].

3.3.6 Imaging two spin states in the same run: the 5 imaging pulses sequence

In order to perform the spectroscopy measurement described in Chapter 4 and Chapter 5 it is very useful to image two different spin states, usually state-$|2\rangle$ and state-$|3\rangle$, within the same experimental run. In order to achieve this, we extend our images sequence to the following 5 consecutive imaging pulses:

1. C^{1a} imaging light pulse resonant with state-$|2\rangle$ atoms
2. C^{1b} imaging light pulse resonant with state-$|3\rangle$ atoms
3. C^{2a} reference pulse resonant with state-$|2\rangle$ atoms
4. C^{2b} reference pulse resonant with state-$|3\rangle$ atoms
5. C^{bg} background

We then calculate the optical densities of the states $|2\rangle$ and $|3\rangle$ by using (C^{1a}, C^{2a}, C^{bg}) and (C^{1b}, C^{2b}, C^{bg}) respectively.
In some of our experimental sequences (described in Chapter 4 and 5), we need to perform an optical blast just before the imaging. This becomes a problem as soon as the time delay between the blast and the first imaging pulse is shorter than the opening time of the CCD shutter, which is of the order of 5 ms. In this case, the light of the blast would be captured by the CCD together with C^{1a}. In order to avoid this, we acquire an additional image before C^{1a} to collect the light from the blast. This image will be later discarded and the optical density calculated in the standard way.

3.3.7 Non-resonant imaging

So far we have discussed about resonant imaging techniques, which are used to selectively probe single hyperfine states of lithium. In this section we will discuss how to exploit non resonant imaging light to probe two spin states at the same time, which can generate a signal with opposite sign. There are several techniques which can be used in ultra-cold atoms experiment such as phase-contrast imaging [80], Faraday imaging [81] and speckle imaging [62]. In the following we will describe the basics of the first one.

Basic theory for dispersive imaging techniques

To understand the principle of non-resonant imaging techniques it is useful to model the atomic cloud as a thin lens following the reference [80]. This model consists of considering the imaging light as an incoming electric field E_0 which is attenuated and phase shifted by the atoms producing an outgoing electric field E_{out}:

$$E_{\mathrm{out}} = tE_0e^{i\phi} = E_0 + \Delta E, \tag{3.23}$$

where t is the transmission coefficient, ϕ is the phase shift and ΔE is the scattered light. As already described in the absorption imaging section, the transmission is given by the

Lamber-Beer law:

$$t = e^{-\mathrm{OD}(\delta)/2} = \exp\left(-\frac{\tilde{n}\sigma_0}{2}\frac{1}{1+\delta^2}\right), \tag{3.24}$$

where $\mathrm{OD}(\delta) = \tilde{n}\sigma_0/(1+\delta^2)$ is the off resonant optical depth of the atomic cloud, being $\tilde{n} = \int dz\, n(x,y,z)$ the column density. The phase shift is given by:

$$\phi = -\delta\frac{\mathrm{OD}(\delta)}{2} = -\frac{\tilde{n}\sigma_0}{2}\frac{\delta}{1+\delta^2}. \tag{3.25}$$

Here is important to notice that, while the absorption is independent of the sign of the detuning, the phase shift varies with it. This is exactly the property that one can exploit to obtain an opposite response signal from two different hyperfine states: if one sets the imaging frequency to be between the resonance of the two, one state will produce a positive shift while the other one negative.

Phase-contrast imaging

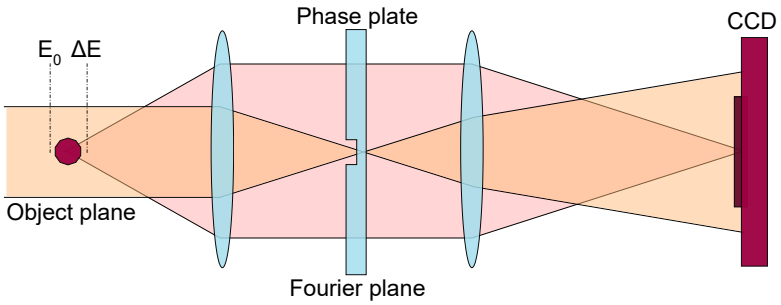

Figure 3.16: Sketch of the phase-contrast imaging scheme. The imaging field interacts with the atomic sample in the object plane. Part of the field is unaffected (E_0, in yellow) and part is scattered by the atoms (ΔE in pink). The phase plate, positioned on the Fourier plane of the imaging, introduces a phase shift between E_0 and ΔE of $\pi/2$. The CCD camera finally detects the intensity resulting from the interference between the two fields.

The phase-contrast imaging is based on the experimental scheme sketched in Figure 3.16: a transparent phase plate[5] is positioned in the Fourier plane of the imaging system. The phase plate has a phase dimple in the middle which shifts the phase of the light by $\pi/2$ with respect to the light passing in the outer region. Hence, the intensity profile generated on the CCD chip is given by the interference between these two fields. We can write the average intensity as [80]:

$$< I_{\mathrm{CCD}} >= \frac{1}{2}\left|E_{\mathrm{out}} + E_0(e^{i\frac{\pi}{2}} - 1)\right|^2 = I_0\left[t^2 + 2 - 2\sqrt{2}t\cos(\phi + \frac{\pi}{4})\right], \tag{3.26}$$

which in the limit of small shift ϕ becomes:

$$< I_{\mathrm{CCD}} >\simeq I_0\left(t^2 + 2 - 2t + 2t\phi\right) \tag{3.27}$$

[5]We use a BK7 phase-plate (n=1.51391 for a wavelength of 670 nm). A circular dimple with a diameter of 200 μm in the middle of the plate introduces a phase shift of $\pi/2$.

In the limit of big detunings, $\delta \gg 1$, the phase shift scales as $1/\delta$ while the transmission as $1/\delta^2$. Hence, the absorption can be neglected, $t \to 1$ and, using equation3.25, we can solve 3.28 for the column density and find:

$$\tilde{n} = \frac{1}{\sigma_0}\frac{I - I_0}{I_0}\frac{\delta^2 + 1}{\delta} = \frac{1}{\sigma_0}\frac{C^1 - C^2}{C^2 - C^{\mathrm{bg}}}\frac{\delta^2 + 1}{\delta}. \tag{3.28}$$

In Figure 3.17 we show two examples of phase contrast images obtained with an imaging frequency between the resonance of the state-$|1\rangle$ and the state-$|2\rangle$. The plotted signal is $\tilde{n}/\delta$ in order to clearly show the effect of the sign of the detuning. The image on the left corresponds to a spin-polarized Fermi gas in the $|2\rangle$ state and the atomic signal is negative because of the negative detuning. On the other hand, the image on the right corresponds to atoms in the hyperfine state-$|1\rangle$, have a positive detuning and positive signal.

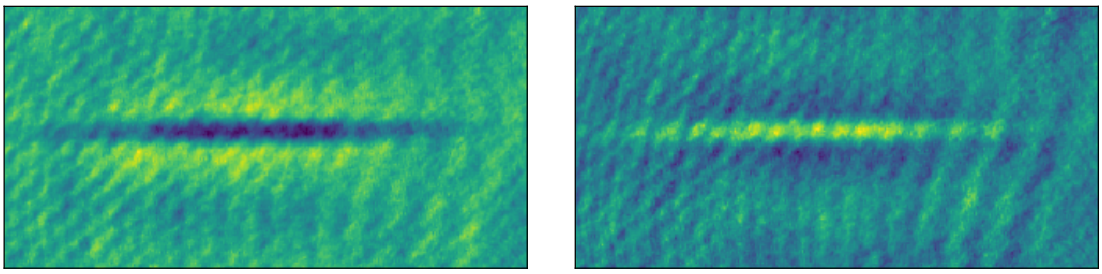

Figure 3.17: Example of phase-contrast signal. The imaging frequency is set between the resonance of the state $|1\rangle$ and the state $|2\rangle$. **The left** panel shows the signal of a spin polarized Fermi gas in the state $|2\rangle$. **The right** panel shows the signal of a spin polarized gas in the state $|1\rangle$. As one can see, the sign of the signal corresponds to the sign of the detuning.

In Figure 3.17 one can also notice that a sort of shadow is present around the atomic cloud. This spurious signal introduced by the phase plate is called *funnel*. This artifact comes from the fact that the size of the phase-plate dimple is finite and does not perfectly match the size of the beam in the Fourier plane. Because of this, part of the scattered field ΔE is also phase shifted by the plate and part of E_0 is not shifted. The result is a low-frequency interference shaped like a *sinc* function. In Figure 3.18 we plot the integration of a phase-contrast signal along the x axis of the cloud, which shows a funnel with an amplitude of about 1/4 of the atomic signal. In order to remove the funnel and isolate the atomic signal we follow the procedure represented in Figure 3.19 which starts by fitting the region of the image not containing the atomic cloud with the following function:

$$f(x, y) = \mathrm{off} + A \exp\left(\frac{(x - x_0)^2}{2\sigma_x^2}\right) \frac{\sin[(y - y_0)s_y]}{(y - y_0)s_y} \tag{3.29}$$

The best fit is now our model of the funnel and can be removed from the whole image allowing us to obtain the atomic signal alone.

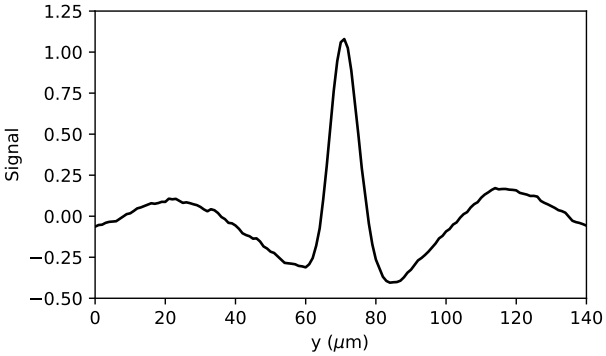

Figure 3.18: Phase-contrast signal of a state $|1\rangle$ spin-polarized Fermi gas integrated along the x direction. The imaging frequency is set between the state-$|1\rangle$ and the state-$|2\rangle$ resonances. One can see the *sinc* shape of the funnel, which has a non negligible amplitude when compared with the atomic signal in the middle.

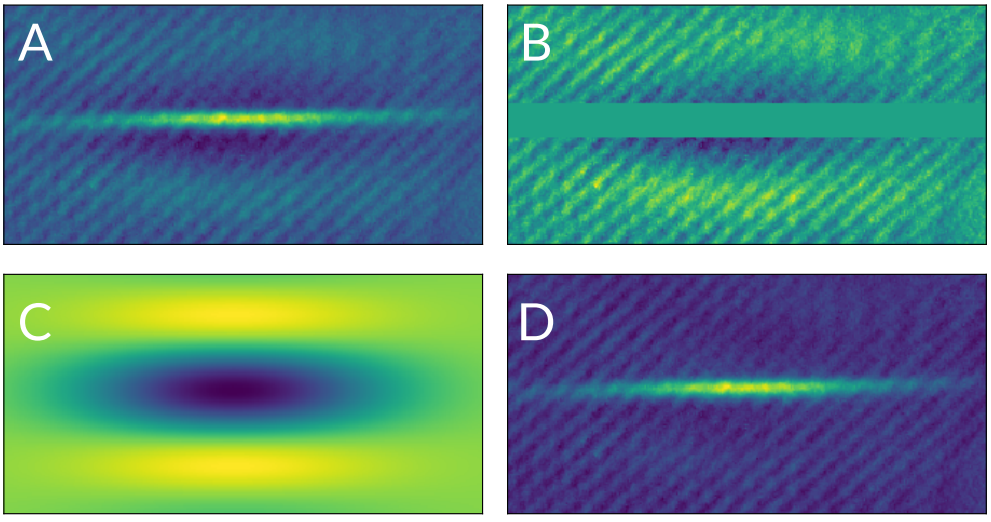

Figure 3.19: **(A)** phase-contrast signal. **(B)** mask on the region of the image occupied by the atomic cloud. **(C)** best fit of the funnel (see equation 3.29) on the unmasked region. **(D)** atomic signal obtained removing the best fit of the funnel from the phase-contrast signal.

While this procedure is very simple when the atomic signal is higher than the funnel amplitude, it becomes very challenging in the opposite scenario, which is indeed very common in our work. Most of the time we are interested in probing a $|1\rangle$-$|2\rangle$ or $|1\rangle$-$|3\rangle$ mixture, hence, when we set the detuning in between the two resonances, the total signal is very close to zero (see Figure 3.20) The relative importance of the funnel increases and the uncertainty on the final atomic distribution increases and becomes very hard to quantify. Because of this reason, other methods like the Faraday imaging or the speckle imaging end up to be a better choice.

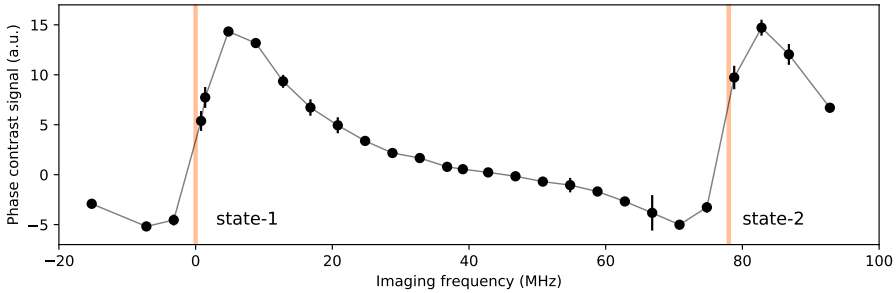

Figure 3.20: Phase contrast signal in the center of the cloud of a balanced $|1\rangle$-$|2\rangle$ mixture as a function of the imaging detuning. The zero detuning is set to be the state-$|1\rangle$ resonance. The positive offset of the signal is due to the funnel, which has not been removed here.

3.3.8 Measuring the atom number fluctuation of a trapped gas

Together with the atomic density, the number of atom variance is a very important observable one can exploit in ultra-cold gases experiments [4, 61, 62, 35, 5]. Atoms fluctuations can be exploited as a thermometer, provide important information about the homogeneities of the density distributions and probe for the presence of spin domains in the system. The measurement of the in-situ density fluctuations of a given atomic sample, i.e. the atom number variance $\Delta N = \mathrm{Var}(N)$, is not straightforward, even though the principle is simple: one takes K images of a given atomic sample prepared with the same experimental condition, measure the number of atoms contained in each pixel and finally calculates the variance of this number:

$$(\Delta N)^2_{i,j} = \frac{1}{K}\sum_{k=0}^{K}\Big(N^k_{i,j} - \langle N_{i,j}\rangle\Big)^2 = \mathrm{Var}(N_{i,j}), \tag{3.30}$$

where the indexes i and j represent the row and column of a given image, k is the image realization index and the angle brackets represents the mean over the K samples: $\langle N_{i,j}\rangle = \sum_{k=0}^{K} N^k_{i,j}/K$. In practice, measuring noise is noisy and full of systematic errors that need to be addressed. The major sources of problems are the following few points:

1. **Imaging resolution:** since the resolution of the imaging system is finite, a point source (i.e. a single atom) in the object plane is spread over several pixels of the CCD chip in the imaging plane (point spread function). This effectively reduces the measured atom number variance.

2. **Total atom number fluctuations:** even though the experimental sequence to realize the atomic sample is kept the same, there are intrinsic fluctuations on the atomic flux, on the laser intensity and on the stability of the magnetic fields that can not be avoided. All these factors, in our experiment, originate a shot to shot fluctuation of the total number of atoms in the cloud of about 15%. This effectively increases the measured atom number variance.

3. **Photon shot noise:** the measurement of the imaging light intensity is ultimately a measurement of a discrete number of photons collected by each pixel of the CCD chip, therefore, it comes with Poissonian fluctuations. These fluctuations contribute as a positive offset to the measured variance.

4. **CCD camera readout and dark noise:** every CCD has both a dark noise, given by the presence of thermal electrons and readout noise, given mostly by electronic noise. Both these effects effectively increase the atom number variance, but with the use of modern CCD cameras, this effect is negligible with respect to those listed above.

In the following, I will describe these effects one by one in more details and the approach we adapted to subtract them from the measured variance.

Imaging resolution

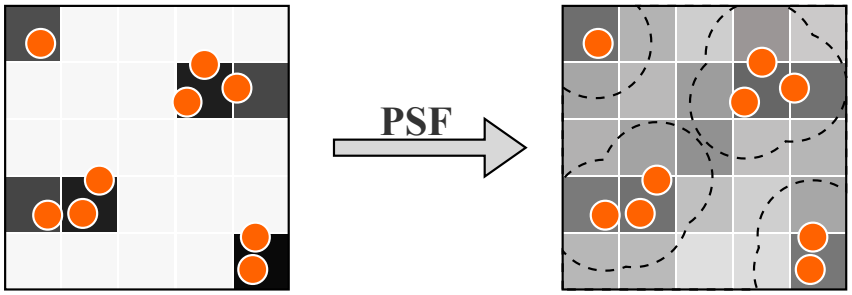

Figure 3.21: Reduction of the detected variance given by the point spread function of the imaging system. On the left, each atom (orange dots) only affects the value measured by a single CCD pixel (darkness of the squares). The result is a signal with high variance: some of the pixels are completely white and some are very dark. On the right, each atom affects all the pixel within its point spread function (dashed orange circle). The result is a low variance signal: most of the pixels are gray.

As sketched in figure 3.21, the observed variance is suppressed when the point spread function of the imaging system is of the same order, or bigger, than the size of a CCD pixel. This is caused by the fact that the signal of a single emitter is shared by more than one pixel. The solution to this problem is, therefore, to increase the size of the pixel until its size is about five times the resolution of the imaging system [82]. This can be done by reducing the magnification of the imaging or by binning more pixel together in a super-pixel. The first approach is beneficial whenever the CCD camera readout and dark noise are non-negligible noise sources since it helps increase the signal to noise ratio in every single pixel. If instead, these effects are negligible, it is much preferred to bin the pixel counts during the data analysis since it does not require a modification of the imaging

setup and the amount of pixel binned together can be chosen in a much more controlled way during the data analysis. It is possible to calculate the variance of a given sample for different binning size $\mathcal{N} \times \mathcal{N}$ and chose the value of $\mathcal{N}$ where the variance reaches the maximum. As shown in figure 3.22 the estimated variance increases with $\mathcal{N}$ until $\mathcal{N} \geq 5$, the limit in which the point spread function can be considered small with respect to the size of the super-bin 5×5. The chosen size of the super-pixel is, therefore, $\sim 5 \times 5 \mu m$ and, since the resolution of our imaging system is $\sim 1.2 \mu m$, the variance reaches a saturation when the ratio between these two values is about $4-5$, consistently with reference [61]. The

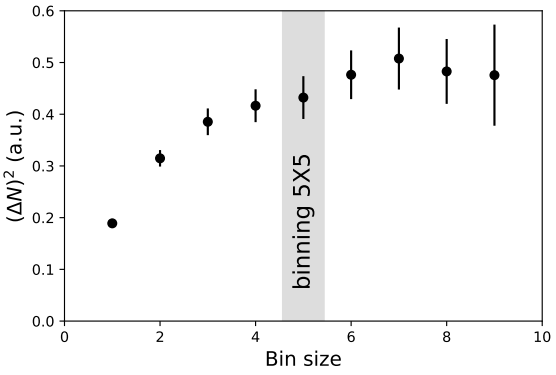

Figure 3.22: Measured variance in a central region $\Re$, corresponding to about 5 atoms per pixel (showed in section 5.3.2), of a Fermi gas cloud obtained with different binning size. For binning size $\mathcal{N} < 5$ the resolution of the imaging system is too close to the size of the pixel, the variance is therefore underestimated and increases as the binning size increases. For binning size $\mathcal{N} \geq 5$, the value of the variance saturates, meaning that the size of a bin is big with respect to the point spread function of the imaging system. The error-bar is given by the standard deviation of the mean of the different variance values obtained for each pixel of the region R.

reason why we stopped at a binning size of 5×5 is that for larger bin sizes the dimension of the super-pixel stops to be negligible with respect to the dimension of the transverse size of the atomic cloud, that is around $30 \mu m$. Because of that, the variance is averaged over regions of different density which implies a loss of resolution when comparing the atom number variance with the atom number average.
The binning procedure should be done directly on the raw images acquired by the CCD camera before the optical density is calculated. While this is not relevant for resolution effect just described, it will help to reduce the effects of photon shot noise and electronic noise as discussed in the next subsection.
To summarize, for each of the K experimental runs we end up with three matrices corresponding to the three acquisitions of the absorption imaging: $C_{i,j}^{1,k}$, $C_{i,j}^{2,k}$ end $C_{i,j}^{\mathrm{bg},k}$ where i and j are the row and the column indexes of the $\mathcal{N} \times \mathcal{N}$ super-pixel and k is the experimental run index. The superscript indexes 1, 2 and "bg" refer to the binned images with atoms, without atoms (i.e. reference) and background described in the section 3.3.2.

Total number fluctuations

The shot to shot fluctuations of the total number of particle of the atomic cloud contributes as an unwanted positive offset to the calculated variance. The first step to reduce this effect is working on the experimental setup and cooling sequence, mostly on the evaporation, in

order to minimize the intrinsic fluctuations. Once the system is optimized we still observe fluctuations on the total number of the order of 15% plus a small number of outliers. In order to reject the outliers, for each experimental run k we calculate the optical density $\mathrm{OD}^k_{i,j}$:

$$\mathrm{OD}^k_{i,j} = \log\left(\frac{C^{2,k}_{i,j} - C^{\mathrm{bg},k}_{i,j}}{C^{1,k}_{i,j} - C^{\mathrm{bg},k}_{i,j}}\right) \tag{3.31}$$

Using the absorption cross section σ_0 and the area A_{sp} of a super-pixel we convert to optical density in number of atoms per super-pixel:

$$\mathrm{N}^k_{i,j} = \frac{A_{\mathrm{sp}}}{\sigma_0}\mathrm{OD}^k_{i,j} \tag{3.32}$$

We then obtain the total number of atoms per shot integrating over all the super-pixels: $N^k_{\mathrm{TOT}} = \sum_{i,j} \mathrm{N}^k_{i,j}$. An example of the total atom number distribution is shown in the histogram in figure 3.23. The outliers are rejected by performing a post selection on the images, discarding 10 experimental shots with the highest and the lowest total atom number. To further reduce the effect of total number fluctuations we fit each optical density

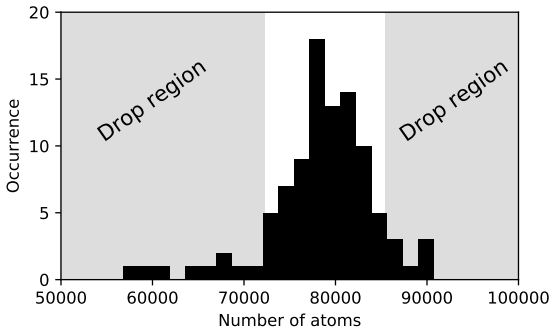

Figure 3.23: Example of total atom number distribution. The outliers (gray region) are discarded from the variance analysis.

profile with a two-dimensional Gaussian envelope and we subtract this envelope from the density profile. This operation corresponds to a high-pass filter to the density profiles: long wavelength fluctuations are suppressed while the short wavelength ones, the ones we are interested in, remain untouched.

Photon shot noise

The measurement of the imaging light intensity is ultimately a measurement of a discrete number of photons collected by each pixel of the CCD chip. If a pixel is illuminated by the imaging light pulse and reveals an average number of photons $\langle N_{\mathrm{ph}}\rangle$, in a single shot the probability p of counting $N^{\mathrm{meas}}_{\mathrm{ph}}$ photons follows a Poisson distribution [82]:

$$p(N^{\mathrm{meas}}_{\mathrm{ph}}) = \frac{\langle N_{\mathrm{ph}}\rangle^{N^{\mathrm{meas}}_{\mathrm{ph}}} \times e^{\langle N_{\mathrm{ph}}\rangle}}{N^{\mathrm{meas}}_{\mathrm{ph}}!}, \tag{3.33}$$

The standard deviation of the Poisson distribution is $\Delta N_{\mathrm{ph}} = \sqrt{\langle N_{\mathrm{ph}}\rangle}$. This relation allows us to link pixel by pixel the variance given by the photon shot noise with the mean

number of revealed photons. Therefore we can obtain the atom number variance $\Delta(N^{\mathrm{at}}_{i,j})^2$ subtracting the photonic component from the measured optical density variance $\Delta(\mathrm{OD}^k_{i,j})^2$ using the relation (see supplementary materials of reference [61]):

$$\Delta(\mathrm{OD}^k_{i,j})^2 = \frac{1}{\langle N^{ph,1}_{i,j}\rangle} + \frac{1}{\langle N^{ph,2}_{i,j}\rangle} + \frac{\sigma_0^2}{A^2}\Delta(N^{\mathrm{at}}_{i,j})^2, \tag{3.34}$$

where $N^{ph,1}_{i,j}$ and $N^{ph,2}_{i,j}$ are the number of detected photons in the pixel i, j. This relationship is strictly valid in the low saturation imaging regime, when it is possible to neglect the linear term in the optical density given by saturation effects (see section 3.3.4). In order to obtain $N^{ph,1}_{i,j}$ and $N^{ph,2}_{i,j}$ we need to convert the CCD counts $C^{1,k}_{i,j}$, $C^{2,k}_{i,j}$ to photons count. One way to do it is to use the gain factor g given by the quantum efficiency of the CCD and its amplifier gain. Despite its simplicity, this method relies on calibrations provided by the CCD camera constructor, therefore we prefer to use a second option instead, that is to directly calibrate this coefficient exploiting the Poisson nature of the imaging light itself. In practice one can acquire some images without the atomic cloud and we find the coefficient g that satisfies the equation:

$$g(\Delta N^{ph})^2 = N^{ph} \tag{3.35}$$

This is equivalent to directly use the images from an experimental run and consider only the regions outside the atomic cloud, where $\Delta(N^{\mathrm{at}}_{i,j})^2$ is 0 by definition, therefore we find g by minimizing the expression:

$$\left(\Delta(\mathrm{OD}^k_{i,j\,\mathrm{out}})^2 - \frac{1}{g\langle C^1_{i,j,\mathrm{out}}\rangle} - \frac{1}{g\langle C^2_{i,j,\mathrm{out}}\rangle}\right)^2 \tag{3.36}$$

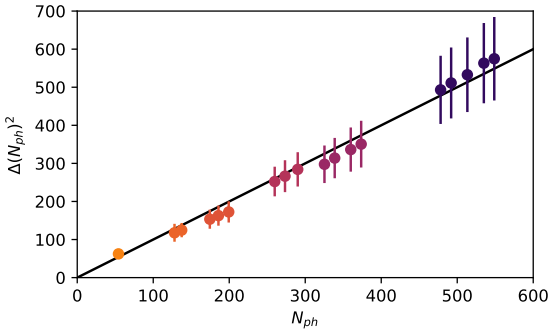

Figure 3.24: Number of photon variance as a function of the mean number of photons per pixel computed from around 60 images of the imaging beam alone. Every color set represents a different measurement performed increasing the imaging light intensity (from yellow to violet). The data points are binned and the error bar is the standard deviation. The spread of the points along the x axis within the same dataset (same color) is due to intensity inhomogeneities of the imaging beam. The Poissonian relationship between number variance and mean (linear with slope 1) allows us to calibrate the gain factor g, i.e. the conversion factor between CCD counts and number of photons.

The result of this optimization is shown in figure 3.25: in orange, we plot the variance of the optical density, while in gray the estimation of the photon shot noise variance. The

number of atom variance is easily obtained by subtracting the second quantity from the first. We notice that, outside the atom cloud region, the two quantities coincide while, inside the region, the photonic variance has only a small positive bump due to the decrease of photon count in the first image $C^1_{i,j,\mathrm{in}}$ because of absorption.

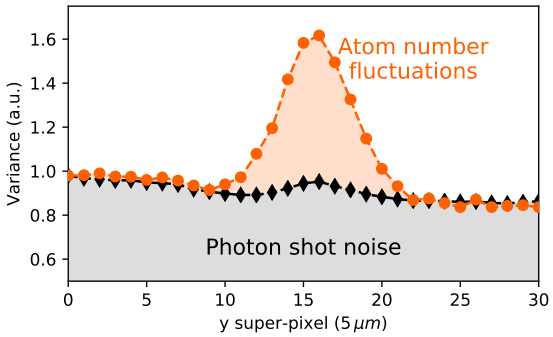

Figure 3.25: In orange the optical density fluctuations profile (integrated along the axial direction of the cloud). In black the variance associated with the photon shot noise of the imaging light, estimated by $1/(g\langle C^1\rangle)+1/(g\langle C^2\rangle)$, where $\langle C^1\rangle$ and $\langle C^2\rangle$ are the average CCD counts per super-pixel and g is the conversion factor from CCD count to number of photons. In the region outside the cloud region the number of atoms variance must be zero and all the optical density variance is fully given by photon shot noise.

CCD camera readout and dark noise

One last element which could contaminate the measurement of the number of atom variance is given by the CCD camera readout noise and dark noise, both contributing with a positive, constant offset. Such noise is mostly dependent on the quality of the CCD sensor that is being used. In our experiment, we use the Andor iXon3 X-9260 CCD camera, with the chip cooled down to $-70°$C. As we can see in the histogram plotted figure 3.26 the contribution of these CCD technical noise sources (in black) are negligible with respect to the one given by photon shot noise (in orange).

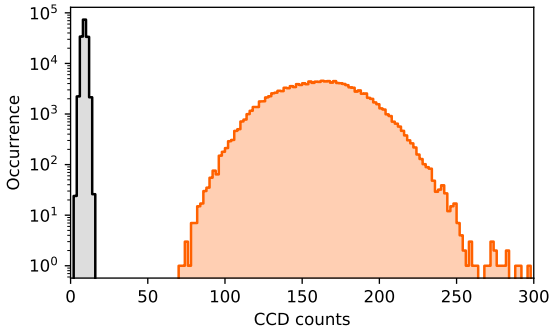

Figure 3.26: Occurrence of number of CCD counts per pixel. In black a background image, without imaging light. This signal is given by the camera readout noise and by its dark current. In orange, an acquisition with the typical illumination used in absorption imaging.

Recap

In conclusion estimate the number of atoms variance of a given sample:

- We acquire around 90 images under identical experimental conditions
- We filter the outliers with unusual total number of atoms
- We remove the Gaussian envelope to decrease the effect of total number of atoms fluctuation in the local variance
- We bin the images with super-pixels of size 5×5
- We calculate the variance of the binned optical densities $\Delta(\mathrm{OD}^k_{i,j}$
- We finally obtain the atom number variance by subtracting the photon shot noise component:

$$\Delta(N^{\mathrm{at}}_{i,j})^2 = \Delta(\mathrm{OD}^k_{i,j\,\mathrm{out}})^2 - \frac{1}{g\langle C^1_{i,j,\mathrm{out}}\rangle} - \frac{1}{g\langle C^2_{i,j,\mathrm{out}}\rangle} \tag{3.37}$$

, where g is the conversion factor between CCD counts and number of photons.

3.3.9 Fluctuation thermometry of an ideal Fermi gas

In order to validate the procedure, we employ to extract the atom number variance from a set of atomic density profiles we test it on a very well known system: the ideal Fermi gas. We used a $|1\rangle$-$|2\rangle$ mixture at 575 G, where the scattering length a_{12} is zero and the gas is completely non-interacting. The motivations for this choice are that we theoretically know the value of the spin density fluctuation and because we can independently measure the temperature of the system from the in-situ density distribution.
Following the procedure described in this section, we obtain $(\Delta N)^2_{ij}$, which is the atom number variance corresponding to the super-pixel (i, j). In Figure 3.28 we plot, for each pixel, the number variance as a function of the mean number of atoms. Here one can see the effect of Pauli principle at work in the atom number variance being much lower than the mean number. While for a classical gas one expects Poissonian fluctuations, i.e. $(\Delta N)^2 = N$, in a degenerate gas the number the number of possible configurations is reduced and so is the number variance and the ratio between $(\Delta N)^2$ and N can be directly linked to the temperature of the system [35]:

$$\frac{(\Delta N)^2_{i,j}}{N_{i,j}} = \frac{\mathrm{Li}_2(\xi_{i,j})}{\mathrm{Li}_1(\xi_{i,j})}, \tag{3.38}$$

where $\xi_{i,j} = \exp(\beta\mu_{i,j})$ is the local fugacity. As shown in Figure 3.27, by numerically solving this equation one can link the atom number variance directly to the temperature. In the center of the cloud we observe that the variance is about 30% of the mean atom number, which correspond (see orange line in Figure 3.27) to a temperature of $T = 0.14(5)T_F$.

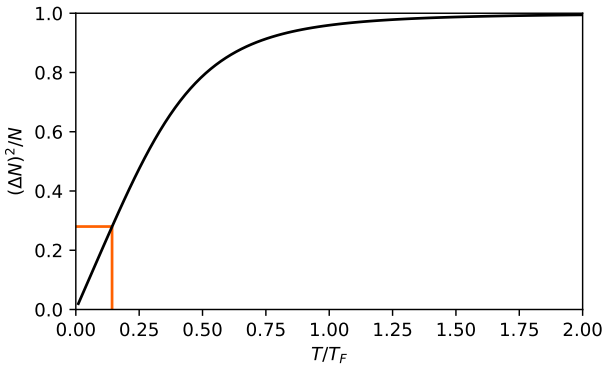

Figure 3.27: Normalized atom number variance as a function of the Fermi gas degeneracy. This result is corrected for the column integration resulting from the absorption imaging as described in Reference [35]. At high degeneracy the fluctuation increases linearly with the temperature. For higher temperature the normalized atom number fluctuations saturate to the classical limit: the Poisson distribution, i.e. $(\Delta N)^2 = N$. The orange lines points to the measured fluctuations in the center of the trap showed in Figure 3.28, from which we estimate the temperature of the cloud to be $T = 0.14(5)T_F$.

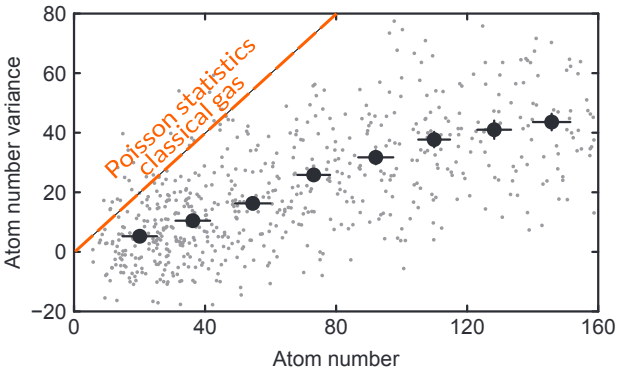

Figure 3.28: Each one of the gray dots correspond to the super-pixel i, j. On the y axis it shows the corresponding atom number variance, on the x axis the mean number of atoms. The black circles correspond to the same data binned for number of atoms. The error-bars show the standard deviation of the mean of all the points included in each bin. In the center of the cloud, the variance value is around 30% of the mean atom number, corresponding to a temperature of $T = 0.14(5)T_F$ as shown in Figure 3.27. The orange dashed line represents the Poissonian statistics of a classical gas: $(\Delta N)^2 = N$

In order to check the full procedure we followed we compare this temperature with the one obtained by fitting the density distribution of the atomic cloud with the polylogarithmic function:

$$n(n,y) = A\,\mathrm{Li}_2\left[-\xi\exp\left(\frac{(x-x_0)^2}{2\sigma_x^2} - \frac{(y-y_0)^2}{2\sigma_y^2}\right)\right]/\mathrm{Li}_2(-\xi), \tag{3.39}$$

from which we extract the fugacity ξ that allows us to calculate the reduced temperature as [83, 84]:

$$\frac{T}{T_F} = -\left(\frac{1}{6\mathrm{Li}_3(-\xi)}\right)^{1/3}. \tag{3.40}$$

The fitted temperature is $T = 0.17(1)T_F$ which is compatible, within the experimental uncertainty, with the result obtained measuring the density fluctuation. In Figure 3.29 we show the polylogarithmic fit on the density profile probed using our horizontal imaging.

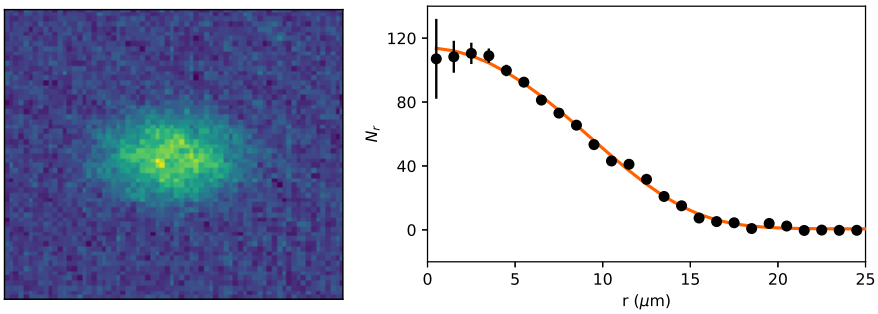

Figure 3.29: On the left the density profile of a non-interacting Fermi gas probed with our horizontal imaging with 6 ms of time of flight. On the right the azimuthally averaged density profile of the cloud (black circles) together with the best fit of equation 3.39 (orange line). The error-bars represent the standard deviation of the mean of the points contained in each azimuthal bin. The fitted temperature is $T = 0.17(1)T_F$

Since the temperature obtained with the two methods is consistent, we conclude that our analysis procedure is adequate to extract the atom number variance from a non-interacting sample. In Chapter 5 we will apply the same procedure to a Fermi mixture quenched to strong repulsion in order to estimate the heating in the system and the possible formation of spin domains.

Chapter 4

N+1: repulsive Fermi gas in the impurity limit

A common idea to approach phases of interacting quantum many-body systems is to start from the impurity limit: few particles immersed in a complex environment. This concept was introduced by Landau and Pekar [14, 15] and further elaborated by Fröhlich and Feynman [16, 17, 18, 85], in the context of condensed matter physics, to describe the interactions between electrons and atoms in solid materials. The idea is to condense the property of a particle interacting with a many-body system in a few key properties of a weakly interacting quasi-particle, the polaron. The study of the impurity problem (N+1) is often much simpler than the balanced (N+N) case but still provides qualitative and sometimes quantitative insight on the latter. Its simplicity arises from the fact that it can be described almost exactly by diagrammatic or variational theoretical approaches, making it particularly suited for the comparison between theories and experiments. In the last few

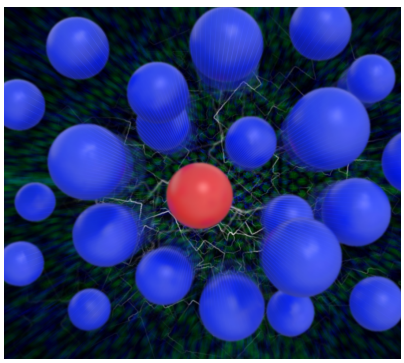

Figure 4.1: Pictorial representation of the repulsive polaron. The presence of a strongly repulsive impurity (red particle) modifies the local wavefunction of the bath (blue particles) effectively screening the interaction at large distances. The system comprising the impurity plus the surrounding particle can be considered as a weakly interacting quasi-particle.

years, in the context of ultra-cold atoms, the polaron problem has been experimentally addressed both in bosonic and fermionic systems [86, 87, 88, 89, 90, 91, 92, 93]. The work described in this chapter fits in this context by presenting the characterization of the Fermi polaron exploiting ultra-cold ^{6}Li atoms via pump-probe radio-frequency (RF) spectroscopy.

This chapter is organized as follows:

- I will give a short theoretical introduction to the polaron problem, showing the link between its properties and the radio-frequency spectroscopy signal.
- I will outline the experimental procedure employed to produce and probe a controllable impurity fraction in the system with a tunable interaction strength.
- I will present our characterization of the repulsive (and attractive) Fermi polaron showing, as a function of the interaction parameter, the behavior of its energy, effective mass, quasi-particle residue and lifetime.

Our measurements will confirm the existence of the upper branch of the repulsive Fermi gas up to very strong coupling, showing how the quasi-particle lifetime greater than $10\hbar/\varepsilon_F$ over a wide range of interactions, exceeding recent theoretical predictions [94, 95]. Moreover, in the strong coupling regime, our data will provide a clear signature of both a ferromagnetic and a thermodynamical instability of the Fermi impurity in the repulsive branch. All the results reported in this chapter are published in Physical Review Letters [19].

4.1 Theoretical introduction of the Fermi polaron

In this section I will briefly introduce the polaron problem by describing its basic properties from a theoretical point of view. I will then link these properties with physical observables measurable through radio-frequency spectroscopy, introducing the physical coupling between the quasi-particle and the RF field.

4.1.1 Properties of the Fermi polaron

A single spin-down atom (the $\downarrow$ "impurity") in an ideal Fermi gas of spin-up atoms forms a quasi-particle, commonly known as the "Fermi polaron" [96, 97, 88, 10]. In Figure 4.2 we

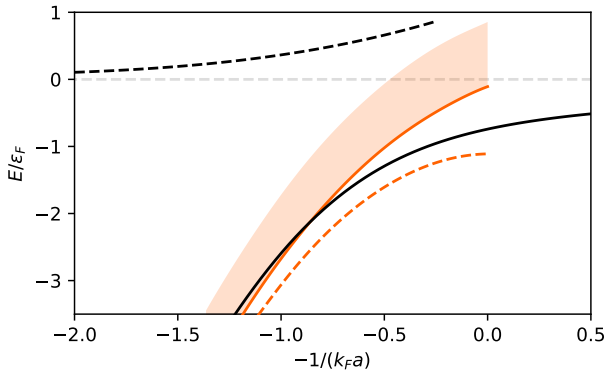

Figure 4.2: Energy spectrum of a zero-momentum impurity in a Fermi sea [10]. The dashed black line is the repulsive polaron energy and the solid black line the attractive polaron one. The orange dashed line represents the dimer energy in vacuum, the orange shaded area the continuum of dressed dimers. The minimum energy of the dressed dimer continuum (solid orange line) crosses the polaron around $1/k_F a \simeq -0.9$, after which the attractive polaron becomes the most energetically favored state.

sketch the energy landscape of the quasi-particle as a function of the interaction parameter. The microscopic interaction potential between ultra-cold atoms is always attractive, leading to negative energy for the ground-state polaron (black solid line). Beyond a critical attraction, the ground state of the mixture becomes a dressed molecule (orange solid line). Associated with this latter quasi-particle, a broad continuum appears in the impurity spectral function, since the impurity can bind to any fermion of the bath with kinetic energy ranging between 0 and E_F (orange shaded area). Moreover, all the approaches to the problem and various experiments revealed that an additional quasi-particle excitation termed "repulsive polaron", appears at positive energies, well separated from the attractive polaron even in the strongly interacting regime (dashed solid line) [56, 94, 95, 92, 93].
The Green's function for the impurity reads[1]:

$$G_{\downarrow}(\mathbf{p},\omega) = \frac{1}{\omega - \xi_{\mathbf{p}\downarrow} - \Sigma(\mathbf{p},\omega) + i0^{+}}, \tag{4.1}$$

where $\xi_{\mathbf{p}\sigma} = \varepsilon_{\mathbf{p}\sigma} - \mu_\sigma = p^2/2m_\sigma - \mu_\sigma$ is the kinetic energy of a σ atom measured with respect to its chemical potential. The effects of the interactions with the Fermi sea are contained in the retarded self-energy $\Sigma(\mathbf{p},\omega)$.
For well defined polarons one can expand the Green's function around the real part $E_\pm$ of the pole at $p = 0$, where $+$ $(-)$ refers to repulsive (attractive) polarons. The approximated Green's function at momenta $p \ll k_F$ reads

$$G_{\downarrow}(\mathbf{p},\omega) \approx \frac{Z_\pm}{\omega - E_\pm - \frac{p^2}{2m^*_\pm} + i\Gamma_\pm/2}, \tag{4.2}$$

This equation contains the full description of the polaron, which is fully characterized by 4 key quantities:

1. The effective mass $\mathbf{m}^*$, which takes into account the difference in the dispersion relation between the bare particle (non-interacting) and the polaron one. Intuitively the higher is the effective mass the more are the particles involved in the excitation, which corresponds to an higher energy for a given velocity. Its definition is:

$$m^*_\pm = \frac{m_\downarrow/Z_\pm}{1 + \mathrm{Re}[\partial_{\varepsilon_{\downarrow\mathbf{p}}}\Sigma(0, E_{\downarrow\pm})]} \tag{4.3}$$

2. The energy $\mathbf{E}_\pm$, which corresponds to the energy difference between the polaron and the bare particle. If it is positive we name the state repulsive polaron, which is an excited state. If it is negative we name it attractive polaron.

3. Quasi-particle residue $\mathbf{Z}_\pm$, which describes the coherence of the quasi-particle and corresponds to the squared overlap between the bare particle and the polaron wavefunctions:

$$Z_\pm = \frac{1}{1 - \mathrm{Re}[\partial_\omega\Sigma(0, E_{\downarrow\pm})]} \tag{4.4}$$

[1] In the following section we use the natural units: $\hbar = k_B = 1$, where $\hbar$ is the reduced Plank constant and k_B the Boltzmann constant.

4. Decay rate $\mathbf{\Gamma}$ of the quasi-particle's probability density, which describes the relaxation of the repulsive polaron into an attractive polaron (or into a dressed molecule / free particle):

$$\Gamma_{\pm} = -2Z_{\pm}\mathrm{Im}[\Sigma(\mathbf{p}, E_{\downarrow\pm})]. \tag{4.5}$$

In the following section we will report how these properties change as a function of the interaction strength by using two different theoretical approaches: the first based on ladder approximation [59, 10] and the second through the minimizing the energy over the "one-particle-hole" (1PH) variational Ansatz [96, 98].

4.1.2 Ladder approximation and one-particle-hole Ansatz

The calculation of the self-energy in presence of very strong interactions is in principle a formidable task. However it turns out that a very good approximation is obtained by summing only the so-called "ladder diagrams", describing forward-scattering in the medium [98]. Under this approximation and taking the quantization volume to one, the retarded self-energy of a single impurity in a zero-temperature Fermi sea close to a broad Feshbach resonance reads ($\hbar = k_B = 1$)

$$\Sigma(\mathbf{p},\omega) = \sum_{\mathbf{q}} f(\xi_{\mathbf{q}\uparrow})\, T(\mathbf{p}+\mathbf{q}, \omega+\xi_{\mathbf{q}\uparrow}) = \sum_{\mathbf{q}} \frac{f(\xi_{\mathbf{q}\uparrow})}{\frac{m_r}{2\pi a} - \sum_{\mathbf{k}} \left[\frac{1-f(\xi_{\mathbf{k}\uparrow})}{\omega-(\varepsilon_{\mathbf{p}+\mathbf{q}-\mathbf{k}\downarrow}+\varepsilon_{k\uparrow}-\varepsilon_{q\uparrow})+i0_+} + \frac{2m_r}{k^2} \right]}, \tag{4.6}$$

where $f(x) = 1/(\exp(x/T)+1)$ is the Fermi function, and $T(\mathbf{P},\Omega)$ is the T-matrix describing the scattering of an $\uparrow - \downarrow$ pair of atoms with total momentum $\mathbf{P}$ and total energy Ω. Furthermore, we have introduced the $\uparrow - \downarrow$ scattering length a, and the reduced mass $m_r = m_\uparrow m_\downarrow/(m_\uparrow + m_\downarrow)$. The quasi-particle properties obtained for the attractive polaron through this ladder approximation compare very favorably both with Quantum Monte-Carlo (QMC) calculations and with experiments [97, 88, 92, 10].
As far as the ground state properties of the system are concerned, solving the problem within the ladder (or non self-consistent T-matrix) approximation is equivalent to minimizing the energy over the "one-particle-hole" (1PH) variational Ansatz [96, 98]:

$$|\psi\rangle = \sqrt{Z}|\mathbf{p}\rangle_\downarrow\, |0\rangle_\uparrow + \sum_{q<\kappa_F}^{k>\kappa_F} \phi_{\mathbf{kq}} |\mathbf{p}+\mathbf{q}-\mathbf{k}\rangle_\downarrow\, c^\dagger_{\mathbf{k}\uparrow}\, c_{\mathbf{q}\uparrow}\, |0\rangle_\uparrow\,. \tag{4.7}$$

Equation 4.7 describes a $\downarrow$-impurity with momentum $\mathbf{p}$ in an ideal Fermi sea $|0\rangle_\uparrow$ of $\uparrow$-particles as a quasi-particle, whose dressing is composed by a superposition of particle-hole pairs.
Since it is analytically continued, the ladder calculation has, however, the additional advantage of being able to investigate excited states of the mixture, such as the repulsive polarons discussed in this work. For the repulsive polaron case, such an approach is found in relatively good agreement with QMC simulations [59, 10], despite a more sizable mismatch compared to the attractive case. Nonetheless, the ladder approximation accurately reproduced the experimental results obtained in a ^{6}Li-^{40}K mixture at a relatively narrow Feshbach resonance [92]. The basic properties of the attractive and repulsive polarons,

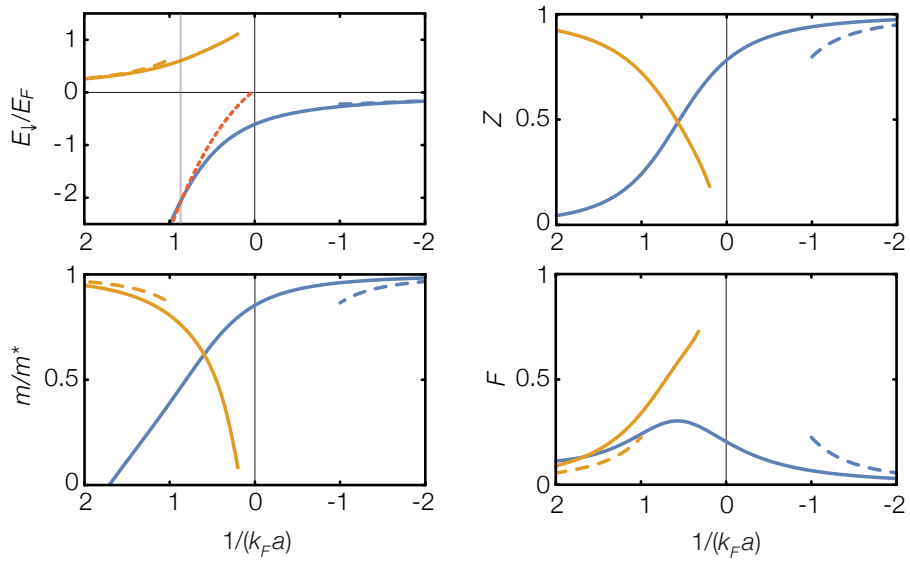

Figure 4.3: Polaron properties calculated in the ladder approximation for the mass-balanced case: energy $E_\downarrow$, residue Z, inverse effective mass m/m^* and Landau parameter F. Blue and orange lines depict, respectively, the attractive and the repulsive polaron. The dotted red line is the energy of a dressed molecule, and the thin vertical line at $k_Fa \simeq 1.15$ indicates the polaron/molecule transition in the attractive branch [97, 99]. The dashed lines are the perturbative results to $O(k_Fa)^2$, as given in Refs. [100, 101, 102].

such as their energies, quasi-particle residues, effective masses, and Landau parameters F obtained by means of the ladder approximation, are summarized in Figure 4.3 and will be used as a cross-validation tool by comparing them with our experimental results described in the following section.

4.1.3 Coupling with the radio-frequency field

In order to extract the energy and the effective mass of the polaron we rely on the so-called reverse radio-frequency (RF) spectroscopy. The minority gas is prepared in state $|2\rangle$, weakly interacting with the majority component. We then apply a RF pulse to transfer the atoms to the empty state $|3\rangle$, which is resonantly interacting with the atoms of the bath. For a homogeneous system and within linear response theory, the RF signal is given by (see e.g. Reference [103])

$$I(\omega) \propto \int \frac{\mathrm{d}\mathbf{k}}{(2\pi)^3} f(\xi_{k,2})\, A_3(\mathbf{k}, \xi_{k,3} + \omega), \tag{4.8}$$

where $A_3(\mathbf{k}, \omega) = -2\,\mathrm{Im}G_3(\mathbf{k}, \omega)$ is the spectral function for the minority gas in state $|3\rangle$. Since the RF pulse has a finite duration, the previous result has to be convoluted in frequency as

$$I_{exp}(\omega) = \int \frac{d\varepsilon}{2\pi}\, g(\omega - \varepsilon)\, I(\varepsilon), \tag{4.9}$$

where $g(\omega)$ can be well approximated by a Gaussian whose width is inversely proportional to the duration of the RF pulse.

When the spectrum contains a well-defined quasi-particle with zero-momentum energy $E_\pm$, the main contribution to the spectral function comes from the quasi-particle pole, i.e., $A_3(\mathbf{k},\varepsilon) = 2\pi Z\,\delta(\varepsilon - E_\pm - k^2/2m^*)$, and the RF signal reads

$$I_{exp}(\omega) \propto \int \frac{\mathrm{d}\mathbf{k}}{(2\pi)^3} f(\xi_{k,2})\, g(\Delta_k - \omega), \tag{4.10}$$

with

$$\Delta_k = E_\pm + \frac{k^2}{2m}\left(\frac{m}{m^*_\pm} - 1\right). \tag{4.11}$$

Therefore the first moment $\bar{\omega}$ of the RF signal is given by the average over the Fermi distribution of Δ_k, i.e.

$$\bar{\omega} = \frac{\int d\omega\; \omega\, I_{exp}(\omega)}{\int d\omega\; I_{exp}(\omega)} \propto \frac{\int \mathrm{d}\mathbf{k}\; \Delta_k f(\xi_{k,2})}{\int \mathrm{d}\mathbf{k}\; f(\xi_{k,2})} = E_\pm + \langle \frac{k^2}{2m} \rangle \left(\frac{m}{m^*_\pm} - 1\right). \tag{4.12}$$

In our experiment, the signal $I_{exp}(\omega)$ is essentially Gaussian, so that its peak value coincides with $\bar{\omega}$.
Our system is however not homogeneous, since the atoms feel a harmonic trapping potential $U(\mathbf{r}) = m(\omega_x x^2 + \omega_y y^2 + \omega_z z^2)/2$. If μ_i is the chemical potential of the impurity atoms in state $|i\rangle$ the RF peak is located at $\mu_3 - \mu_2$. Within LDA at $T = 0$ we can write

$$\mu_2 = \frac{(6\pi^2\, n_2(\mathbf{r}))^{2/3}}{2m} + U(\mathbf{r})\,, \tag{4.13}$$

$$\mu_3 = \frac{(6\pi^2\, n_3(\mathbf{r}))^{2/3}}{2m^*_\pm(\mathbf{r})} + E_\pm(\mathbf{r}) + U(\mathbf{r})\,. \tag{4.14}$$

To estimate the polaron parameter we average the difference $\mu_3 - \mu_2$ on the non-interacting density n_2 on a finite region V. Since the variance of the majority Fermi momentum over the integration region V is only around 1% of its mean value κ_F, we may safely approximate the average values of the polaron parameters by their values computed at κ_F. Assuming furthermore that in such a region n_3 does not differ too much from n_2, we obtain

$$\Delta_\pm = \langle \mu_3 - \mu_2 \rangle = \\ \frac{1}{\mathcal{N}_2}\int_V \mathrm{d}\mathbf{r}\left(\frac{(6\pi^2 n_3(\mathbf{r}))^{2/3}}{2m^*_\pm(\mathbf{r})} - \frac{(6\pi^2 n_2(\mathbf{r}))^{2/3}}{2m} + E_\pm(\mathbf{r})\right) n_2(\mathbf{r}) \simeq E_\pm(\kappa_F a) + \bar{\varepsilon}\left(\frac{m}{m^*_\pm(\kappa_F a)} - 1\right), \tag{4.15}$$

with $\mathcal{N}_2 = \int_V \mathrm{d}\mathbf{r}\; n_2(\mathbf{r})$. With similar arguments, one can write the contribution due to the Landau polaron-polaron interaction by adding to Equation 4.15 the following term:

$$\Delta_{\mathrm{int}} = \frac{6}{5}\,\alpha\,\varepsilon_F\, F(\kappa_F a)\,\bar{x} \tag{4.16}$$

where $\alpha = (\bar{n}_2/\bar{n}_1)/\bar{x}$ is a factor smaller than 1. Here, $\bar{x}$ and $\bar{n}_i$ are the concentration and the density of state-$|i\rangle$ atoms averaged over the integration region. In our temperature and concentration regime ($\bar{x} < 0.5$), we find α to significantly reduce the effect of the polaron interaction with respect to the naive expectation $\varepsilon_F\, F(\kappa_F a)\,\bar{x}$. Although we refrain from providing a quantitative estimate, such an effect could motivate the absence of polaron-polaron interaction effects in our measurements.

4.2 Experimental procedure

In order to explore strong impurity-bath interactions, we exploit the magnetic field difference between the Fano-Feshbach resonances of $|1\rangle$-$|2\rangle$ states and $|1\rangle$-$|3\rangle$ states. As shown in Figure 4.4 if the bias magnetic field ranges between 600-700 G the scattering length $a_{13} \gg a_{12}$. We can, therefore, regard the initial $|1\rangle$-$|2\rangle$ mixture as a weakly interacting gas while we can finely tune the interactions between states $|1\rangle$ and $|3\rangle$ from the weakly repulsive regime up to the unitary limit.

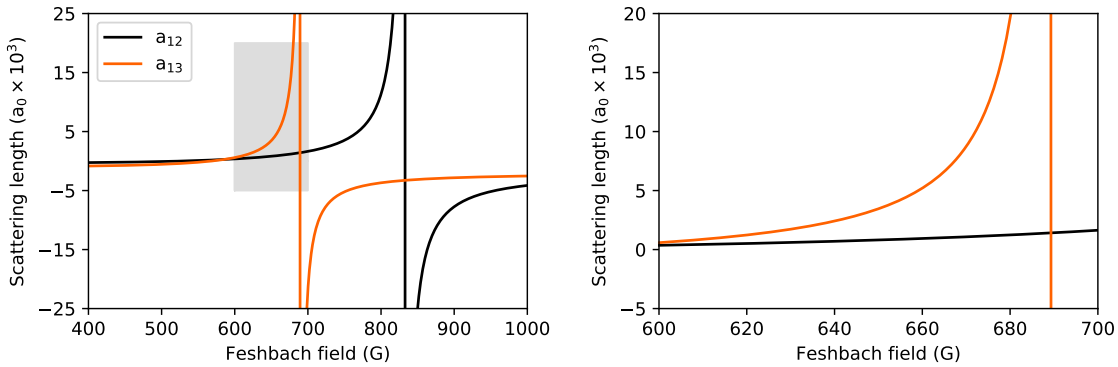

Figure 4.4: $|1\rangle$-$|2\rangle$ (black line) and $|1\rangle$-$|3\rangle$ (orange line) Fano-Feshbach resonances in ^{6}Li. The data points are taken from the supplementary material of reference [44]. The right plot shows the zoom of the data from 600 to 700 G (gray region in the left plot). In this region the scattering length a_{12} is very small compared to the scattering length a_{13}, therefore, one can treat the 1-2 mixture as almost non interacting while controlling the 1-3 mixture interaction strength up to the unitary regime by changing the bias magnetic field.

4.2.1 Preparation

The starting point of the experiments is a weakly interacting balanced mixture of about 2×10^5 ^{6}Li atoms occupying the lowest and the third-to-lowest hyperfine atomic states $|1\rangle$ and $|3\rangle$, characterized at low magnetic field by quantum numbers $|F = 1/2,\ m_F = +1/2\rangle$ and $|F = 3/2,\ m_F = -3/2\rangle$. The gas is confined in a cylindrically-shaped optical dipole trap with corresponding harmonic axial and radial frequencies $\omega_{\text{ax}} = 2\pi \times 19.7(2)$ Hz and $\omega_\perp = 2\pi \times 233(5)$ Hz. The temperature is set to $T = T_F \times 0.10(2)$, where T_F is the Fermi temperature defined by the Fermi energy $E_F = k_B T_F$.
In order to create an unbalanced mixture of the two lowest hyperfine atomic states $|1\rangle$ and $|2\rangle$ and control the initial **impurity concentration**, i.e. the ratio $x = N_2/N_1$ between the populations of these two states, we first adiabatically ramp the Feshbach field to 585 G, where the scattering length a_{12} crosses the scattering length 1-3: $a_{13} \simeq a_{12} \simeq +300a_0$. We then apply a radio-frequency (RF) pulse resonant to the $|3\rangle \to |2\rangle$ transition, transferring part of the atoms into the $|2\rangle$ state. Immediately after, we remove all remaining state-$|3\rangle$ atoms via a resonant optical blast. The duration and the power of the blast are chosen such that it can completely clean the state-$|3\rangle$ atoms without at the same time causing appreciable heating on the remaining $|1\rangle$-$|2\rangle$ sample. The impurity concentration x is controlled by changing the duration of the radio-frequency pulse. We then adiabatically ramp the bias magnetic field to a target value to set the interaction parameter $\kappa_F a$ of the

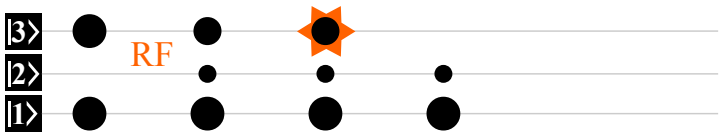

Figure 4.5: Initialization scheme for the $|1\rangle$ - $|2\rangle$ atomic mixture with controlled impurity concentration x. **(a)** Start with balanced $|1\rangle$ - $|3\rangle$ mixture. **(b)** Sweep to 858 G (where the scattering length $a_{13} \simeq a_{12}$). **(c)** Transfer a controlled amount of atoms from state-$|3\rangle$ to state-$|2\rangle$ adjusting the duration of a resonant RF pulse. **(d)** Blast the remaining state-$|3\rangle$ atoms with resonant light.

experimental run. The Fermi wave-vector κ_F, averaged over the central region of the cloud as described in the next section, is calculated from the measurement of the total number of atoms in the state-$|1\rangle$ N_1, and the trap frequencies ω_x, ω_y and ω_z:

$$\kappa_F = \eta_k \times \sqrt{\frac{2m(\omega_x\omega_y\omega_z)^{1/3}}{\hbar}}(6N_1)^{1/6}, \tag{4.17}$$

where η_k is a correction introduced to keep into account the density inhomogeneities given by the harmonic trapping potential.

4.2.2 Effective Fermi energy and Fermi wave-vector

The interaction strength between the state-$|1\rangle$ and state-$|3\rangle$ is parametrized using the dimensionless parameter, $k_F a$, that is the product of the Fermi wave-vector and the scattering length, which depends on the atomic density and on the bias magnetic field. Since our sample is harmonically trapped the density is not homogeneous, hence the inter-atomic interactions are not constant across the cloud. In order to reduce this effect we extract the spectroscopy signal only from the central part of the column density, contained in a rectangular region $\mathcal{R}$ of size $30\mu\text{m} \times 70\mu\text{m}$ along the transverse and axial directions of the cloud, respectively, as shown in Figure 4.6.

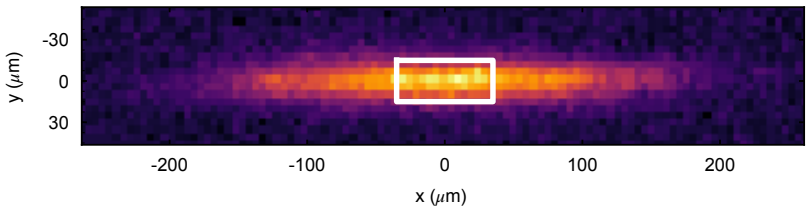

Figure 4.6: Example of the Fermi gas profile. The white rectangle corresponds to the region $\mathcal{R}$ from which the spectroscopy signal is extracted in order to reduce the effect of density inhomogeneities due to the trapping potential. The center of the rectangle is set to be the center of the atomic cloud. The size of the rectangle is fixed to $30\mu\text{m} \times 70\mu\text{m}$.

Within this region we define the effective Fermi wave-vector κ_F and the effective Fermi energy ε_F are the average value of the local Fermi wave-vector $k_F(\mathbf{r}) = (6\pi^2 n(\mathbf{r}))^{1/3}$ and of the local Fermi energy $E_F(\mathbf{r}) = \hbar^2/(2m)k_F(\mathbf{r})^2$. We obtain these two quantities by considering the finite-temperature density distribution $n(\mathbf{r})$ of an ideal Fermi gas, using

the experimental T/T_F, trap frequencies and total atom number N:

$$n(\mathbf{r}) = -\left(\frac{mk_BT}{2\pi\hbar^2}\right)^{3/2} \mathrm{Li}_{\frac{3}{2}}\left(-\exp(\beta(\mu - U(\mathbf{r})))\right), \tag{4.18}$$

where $\mu \equiv \mu(T/T_F, N)$ is chemical potential in the center of the trap, $U(\mathbf{r})$ is the trapping potential, $\beta \equiv 1/(k_BT)$ is the coldness, and $\mathrm{Li}_{3/2}$ is the polylogarithm function of order 3/2. The effective Fermi energy and effective wave vector are obtained by averaging inside the density region $\mathcal{R}$:

$$\varepsilon_F = \frac{\hbar^2}{2m}\int_{\mathcal{R}} d\mathbf{r}(6\pi^2 n(\mathbf{r}))^{2/3} n(\mathbf{r}) \Big/ \int_{\mathcal{R}} d\mathbf{r}\; n(\mathbf{r}) \tag{4.19}$$

and

$$\kappa_F = \int_{\mathcal{R}} d\mathbf{r}(6\pi^2 n(\mathbf{r}))^{1/3} n(\mathbf{r}) \Big/ \int_{\mathcal{R}} d\mathbf{r}\; n(\mathbf{r})\;, \tag{4.20}$$

Numerically solving these equations we find the numerical factors η_E and η_k that link the averaged quantities with the corresponding peak values, i.e. $E_F \equiv E_F(\mathbf{r}=0) = \hbar\omega_{h.o.}(6N)^{1/3}$ and $k_F \equiv k_F(\mathbf{r}=0) = (2mE_F)^{1/2}/\hbar$, where $\omega_{h.o.} = (\omega_x\omega_y\omega_z)^{1/3}$ is the geometrical mean of the harmonic oscillator trap frequencies:

$$\varepsilon_F = \eta_E E_F \quad \text{and} \quad \kappa_F = \eta_k^{1/2} k_F \tag{4.21}$$

For typical experimental parameters we find correction factors $\eta_k = 0.72(1)$ and $\eta_E = 0.51(1)$. From here on when we mention the Fermi energy or the Fermi wave-vector, we will implicitly refer to the rescaled quantities κ_F and ε_F.

4.2.3 Reverse spectroscopy

Let us now discuss the radio-frequency spectroscopy scheme employed to probe the energy spectrum on the many body system. As described in section 4.2.1 we start from a $|1\rangle$ - $|2\rangle$ weakly repulsive gas with impurity concentration x. The final-state interaction strength state-$|1\rangle$ and state-$|3\rangle$ atoms is set by the Feshbach magnetic field. We spectroscopically probe the $|2\rangle \to |3\rangle$ transition applying a near resonant RF rectangular pulse and measuring the spectroscopy signal defined as:

$$\frac{N_3}{N_2 + N_3}, \tag{4.22}$$

where N_2 and N_3 are the number of atoms measured in the rectangular region of size $70 \times 30\,\mu$m in the center of the atomic cloud, as shown in Figure 4.6). This normalization requires to measure two different spin state in the same experimental run (see 3.3.5), but drastically improves the signal to noise ratio of the spectroscopy signal by decreasing the effect of the shot-to-shot total number of atoms fluctuations. By scanning the frequency of the RF pulse we measure $N_3/(N_2+N_3)$ as a function of the detuning Δ, which is defined as:

$$\Delta = \nu - \nu_0, \tag{4.23}$$

where ν is the RF frequency and ν_0 the resonance frequency corresponding to the $|2\rangle \to |3\rangle$ bare transition, which is obtained by measured on a spin-polarized Fermi gas as described

in section 3.2. The spectroscopy pulse has a rectangular shape and its duration ranges from 0.5 ms to 1 ms, which is the best compromise we found to balance our time and spectral resolution: the longer is the duration, the higher is the frequency resolution but undesired dynamical effects taking place during the pulse become more relevant, e.g. $|2\rangle$-$|3\rangle$ interactions which arise when the superpositions between these two states are driven by impurity-bath collisions into statistical mixtures after a sufficient decoherence time.
In the following section, this procedure will allow us to study the properties of the repulsive polaron by varying both the initial impurities concentration and the interaction parameter.

4.2.4 Repulsive polaron spectra

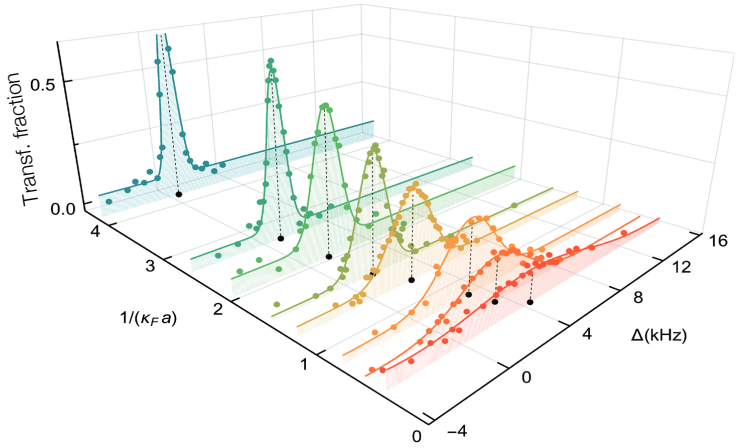

Figure 4.7: Repulsive polaron spectra for different interaction parameters $k_F a$. The frequency shift Δ is the energy difference between the polaron peak and the bare Breit-Rabi transition. The shifts and the spectral widths grow with $k_F a$ because of the increasing repulsive energy between the impurities and the particles in the bath and because of the collisional broadening respectively.

In Figure 4.7 we plot several repulsive polaron spectra for different interaction parameters. The solid line is a Gaussian fit employed to extract the position and the width of the spectroscopy peaks. For increasing interaction strength kFa we observe that:

- The radio-frequency shift Δ increases monotonically, due to the interaction energy given by the repulsion between the impurities and the surrounding Fermi sea and to the impurity momentum k.
- The spectral width gets wider mainly because of collisional broadening.

In order to compare the polaron energy plotted in Figure 4.2 with the measured frequency shift Δ we need to take into account the momentum and the concentration of the impurities. While theoretical value is calculated considering a zero-momentum single impurity, experimentally their number is finite, which introduces two different effects: first, the average momentum is modified by the Pauli pressure, second, when the density of the impurities is non-negligible, one can expect the presence of polaron-polaron effective interactions. In order to understand the effect of the finite impurities momentum on the spectroscopy signal we can consider that, due to the difference in the effective mass, the dispersion relation of the initial state differs from the final one. As shown in figure 4.8

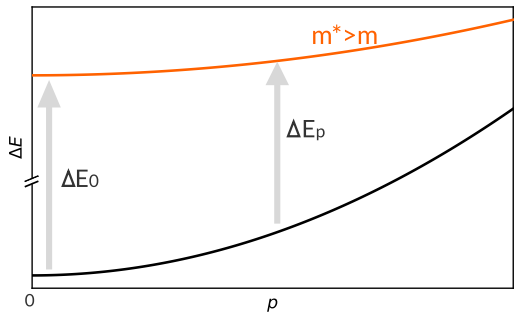

Figure 4.8: Sketch of the dispersion relations of non interacting particle (bottom black solid line) compared to a quasi-particle with effective mass $m^* > m$ given by the interaction with the bath (top orange solid line). Since the spectroscopy protocol transfers the impurities from the non-interacting state to a resonantly interacting one without changing their momentum, the resonant frequency will be momentum dependent.

the dispersion curvature relative to the quasi-particle (with effective mass m^*) is smaller than the one associated with the bare particle. Since the RF spectroscopy pulse does not exchange momentum with the particles[2], the measured energy shift depends of the initial momentum of the impurity: the higher the momentum, the smaller is the shift. As we have previously calculated (equation 4.11), the difference between the zero-momentum shift and the finite-momentum one can be expressed as :

$$\Delta_k(p) = -\frac{p^2}{2m}\left(1 - \frac{m}{m^*}\right) \tag{4.24}$$

At a fixed temperature $T \simeq 0.1T_F$, the mean kinetic energy per impurity $\bar{\varepsilon}$ grows with the impurity concentration x given the increase of the Fermi pressure. In order to estimate the zero-momentum polaron energy, we perform several spectroscopy runs by varying the impurity concentration. We then plot the RF shift against $\bar{\varepsilon}$ and finally, we extrapolate the zero-energy shift. The dependence between impurity concentration and energy in the region of interest $\mathcal{R}$ (see Figure 4.6) can be computed by averaging the energy of the non-interacting impurities using the local density approximation (LDA) and assuming the thermal equilibrium with the bath:

$$\bar{\varepsilon}(x) \equiv \bar{\varepsilon}_2(x) = \frac{4\pi}{(2\pi\hbar)^3 N_2(x)} \int_{\mathcal{R}} \mathrm{d}\mathbf{r} \int_0^\infty dp\, p^2 \frac{\varepsilon_{\mathbf{p},\mathbf{r}}}{e^{\beta(\varepsilon_{\mathbf{p},\mathbf{r}} - \mu(x))} + 1}, \tag{4.25}$$

where N_2 is the number of impurity in the region $\mathcal{R}$, $\mu(x)$ is the chemical potential of the impurity and $\varepsilon_{\mathbf{p},\mathbf{r}}$ is the single particle energy given by:

$$\varepsilon_{\mathbf{p},\mathbf{r}} = \frac{p^2}{2m} + U(\mathbf{r}), \tag{4.26}$$

and $U(\mathbf{r})$ is the harmonic trapping potential. Analytically integrating over the momentum one obtains:

$$\bar{\varepsilon}(x) = -\frac{1}{N_2(x)}\left(\frac{mk_BT}{2\pi\hbar^2}\right)^{3/2} \int_{\mathcal{R}} \mathrm{d}\mathbf{r} \left(\frac{3}{2} k_B T \,\mathrm{Li}_{\frac{5}{2}}\left(-e^{\beta(\mu(x) - U(\mathbf{r}))}\right) + U(\mathbf{r})\,\mathrm{Li}_{\frac{3}{2}}\left(-e^{\beta(\mu(x) - U(\mathbf{r}))}\right)\right). \tag{4.27}$$

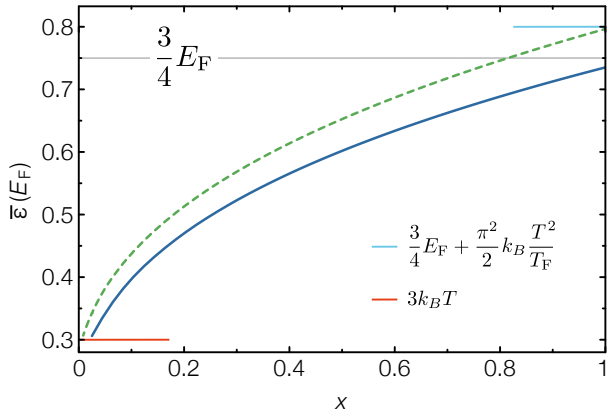

Figure 4.9: Mean energy per particle in the experimental spectroscopy integration region V. The solid blue line is the result of Equation 4.27 for $T/T_F = 0.1$. For comparison, the result of Equation 4.27 when V is set to the full trap volume is plotted as a dashed green line.

The mean energy as a function of the impurity concentration is shown in Figure 4.10 as the blue solid curve. For comparison, we also show the result obtained by extending the integration region to the whole atomic cloud as the dashed green curve. Using this result we can express the mean impurity energy as a function of the concentration and plot it as a function of the measured radio-frequency shift in Figure 4.10. We observe a linear dependence between $\bar{\varepsilon}$ and Δ which strongly indicates that polaron-polaron interactions are negligible even for impurities concentration of the order of 0.4. Their presence would, in fact, lead to a non-linear dependence between the shift and the mean impurity energy: $x \sim \bar{\varepsilon}^{3/2}$ [104, 105, 106]. Moreover, they would introduce an additional spectral broadening which we do not detect in the spectroscopy signal.
By linear fitting the shift and the mean impurity energy we obtain both the effective mass m^* and the zero-momentum energy E_+. In order to take into account for the small but finite interaction of the $|2\rangle$-state impurities in the fit, we introduce a small mass renormalization of the initial state as an offset:

$$\Delta_+ = E_+(k_F a_{13}) - E_+(k_F a_{12}) + \left(\frac{m}{m^*(k_F a_{13})} - \frac{m}{m^*(k_F a_{12})}\right)\bar{\varepsilon} \tag{4.28}$$

where $E_+(k_F a_{12})$ and $m^*(k_F a_{12})$ are estimated by means of a second-order perturbation theory. In Figure 4.11 we plot the repulsive polaron energy and its effective mass for different interaction parameters. The results show a reasonable agreement with recent theoretical predictions based on different methods: variational wave function approach[56], on diagrammatic calculations within the ladder approximation[94], on the functional renormalization group [95] and on quantum Monte Carlo simulations [59].
The data shown in Figure 4.11 provides a strong hint on the existence of a ferromagnetic instability of the repulsive Fermi liquid encouraging us to study the balanced repulsive Fermi gas described in the next chapter. The repulsive polaron energy becomes larger than the Fermi energy ε_F for $1/(k_F a) < 0.6$, which indicates that a phase separated

[2]The momentum transfer is finite but completely negligible: a 80 MHz radio-frequency photon carries a momentum given by $k = 2\pi\nu/c \simeq 5 \times 10^{-7} k_F$, where k_F is the Fermi momentum, which is the relevant momentum scale in the system.

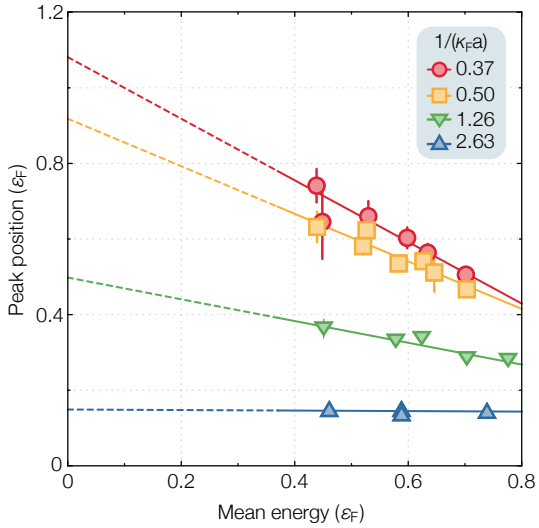

Figure 4.10: Repulsive energy shift as a function of the mean impurity energy for different interaction parameter. The lines are the best linear fits on the data. The dashed part of the lines represents the extrapolation to zero impurity concentration, which is used to extract the zero momentum polaron energy. The error-bars denote the standard errors of the repulsive polaron peak position estimated with a Gaussian fit. The linearity between energy shift and mean impurity energy rules out the presence of polaron-polaron interactions and fits with the renormalization of the polaron mass alone.

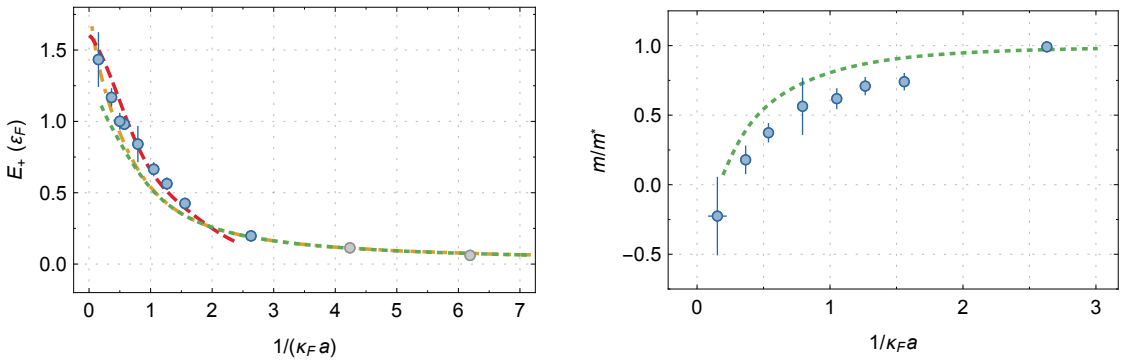

Figure 4.11: **On the left** the repulsive polaron energy E_+ as a function of the interaction parameter. The experimental points are compared with different theoretical prediction: (dot-dashed yellow line) variational wave function approach [56], (dotted green line) diagrammatic calculations within the ladder approximation [94] and (dashed red line) functional renormalization group [95]. Gray symbols denote points obtained by averaging measurements at different impurity concentration instead of zero impurity energy extrapolation, since at these very low interaction strengths the renormalized mass is compatible with the bare particle mass within the error bars, making the extrapolation meaningless. **On the right** the ratio between the bare particle mass and the polaron effective mass as a function of the interaction parameter. The dotted green line shows the theoretical prediction of reference [94]. In both panels the error bars combine the linear fit parameter errors with the standard error of the mean (s.e.m.) of binned data.

state becomes energetically favored with respect to the Fermi liquid of repulsive polarons [56, 59, 94, 10]. Also the behavior of the effective mass points to a thermodynamical

instability of the Fermi liquid: for the highest measured interaction strengths, the ratio between the bare and the effective polaron mass drops to zero and even turns negative [10].

4.2.5 Polaron lifetime

Another very important parameter characterizing the repulsive polaron is its lifetime. This is a key quantity both to define the stability of the particle and to test the applicability of the Landau's quasi-particle theory. If the lifetime is short with respect to the coherence time, the quasi-particle itself is ill defined and the Landau's description inappropriate. Experimentally the lifetime is measured with a pump-probe spectroscopy scheme which consists in two radio-frequency spectroscopy pulses separated by a variable holding time Δt. The first pulse is resonant with the repulsive polaron peak, its power is set to the maximum allowed by our experimental setup and its duration is set by optimizing the transfer from the state-$|2\rangle$ impurities to the state $|3\rangle$, into the upper branch. The second pulse is identical to the first one and selectively brings the repulsive quasi-particle back to the weakly interacting state. The number of $|2\rangle$ atoms after this second RF pulse quantifies the number of repulsive quasi-particles in the system surviving after the holding time Δt. The decay rate Γ of the repulsive polaron is extracted for different interaction strengths via a simple exponential fit:

$$\frac{N_2}{N_2 + N_3}(\Delta t) = \text{off} + A\, e^{-\Gamma\, \Delta t}, \tag{4.29}$$

In Figure 4.12 we show the decay of the population of repulsive polarons for three different interaction parameters.

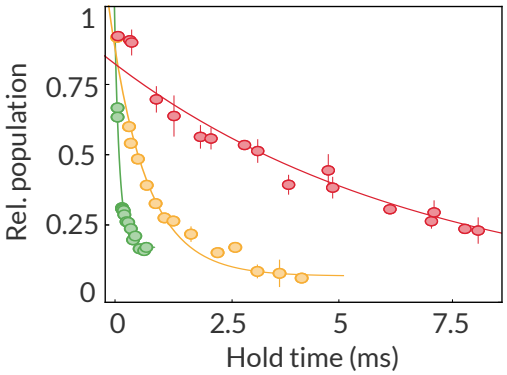

Figure 4.12: Examples of the decay of the repulsive polaron population for three different interaction parameters: $k_F a \simeq 1$ (red), $k_F a \simeq 1.3$ (yellow) and $k_F a \simeq 3$ (green). The solid line shows the best fit of the decay using equation 4.29.

The decay rate for different interaction parameters is shown in Figure 4.13
One can observe that the decay rate Γ strongly depends on the interaction parameter and spans almost four orders of magnitude in the range $0.3 < 1/(k_F a) < 2.7$. For weak coupling, $1/(k_F a > 1)$, the repulsive polaron lifetime is well described by the three-body recombination process triggered by the collision with two fermions from the state-$|1\rangle$ bath as described in Reference [63] by the equation:

$$\Gamma_3 = \frac{148\,\hbar\, a^4}{m} \frac{\bar{\epsilon}}{\epsilon_B}\, n_{|1\rangle}^2\,. \tag{4.30}$$

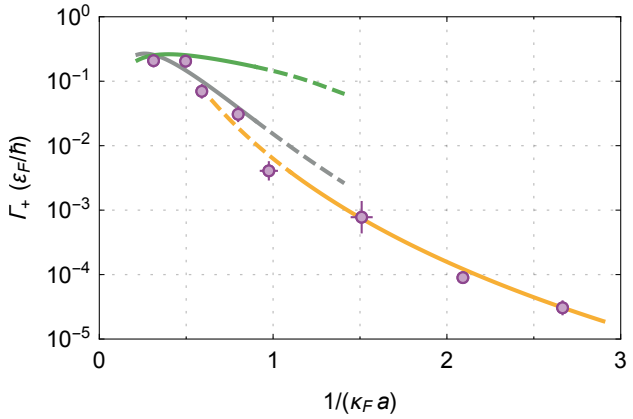

Figure 4.13: Decay rate Γ of the repulsive branch population as a function of the interaction parameter $1/(k_F a)$. Together with the experimental data (purple circles) we show the theoretical predictions for 3-body recombination [63] (orange line), repulsive to attractive polaron decay [94] (green line) and polaron to bare atom (gray line).

Here, $n_{|1\rangle}$ is the density of the bath, ϵ_B is the molecule binding energy, and $\bar{\epsilon}$ is the mean collision energy, which in turn corresponds to the mean kinetic energy of a fermion of the bath. We neglect the collision energy contribution from the impurity, which is small when $x \ll 1$. We set $\epsilon_B \approx \hbar^2/(ma^2) + \varepsilon_F$, which accounts for the removal of one fermion from the bath once a molecule is formed, while it neglects atom-dimer interactions and non-trivial medium effects. From this we obtain:

$$\frac{\hbar\Gamma_3}{\varepsilon_F} = 0.298\,\frac{148}{(6\pi^2)^2}\,\frac{(\kappa_F a)^6}{1+\frac{1}{2}(\kappa_F a)^2}\,, \tag{4.31}$$

where the numerical factor 0.298 results from averaging the kinetic energy and the squared density of the bath over the integration region. The decay rate Γ_3 is plotted as an orange solid line in Figure 4.13.

For higher interaction parameter two other decay channels become available: the two-body inelastic decay onto attractive polaron and the one onto the bare particle. The former case is described in References [94, 10] using the ladder approximation and corresponds to the transition between the repulsive polaron to the ground state of the system for $k_F a \geq 1.15$ which is an attractive polaron. The theoretical prediction Γ_{PP}, plotted in green in Figure 4.13, matches the experimental data only for very high interaction strength close to the unitary regime, while for weaker interactions it underestimate the lifetime by more than one order of magnitude. The latter decay mechanism, shown in gray, corresponds to the annihilation of the repulsive polaron into a bare particle and quantitatively agrees with experimental data for a much wider range of interaction down to almost $k_F a = 1$. We can calculate Γ_{PF} by assuming that the repulsive polaron decays into a bare impurity with a weight $1 - Z_+$ and with an effective mass well approximated by the bare mass. Within this limit the self-energy (see section 4.1.1) reads:

$$\tilde{\Sigma}(\mathbf{p},\omega) = \sum_{\mathbf{q}} \frac{f(\xi_{\mathbf{q}\uparrow})}{\frac{m}{4\pi a} - (1-Z_+)\sum_{\mathbf{k}}\left[\frac{1-f(\xi_{\mathbf{k}\uparrow})}{\omega-(\varepsilon_{\mathbf{p}+\mathbf{q}-\mathbf{k}\downarrow}+\varepsilon_{k\uparrow}-\varepsilon_{q\uparrow})+i0_+} + \frac{m}{k^2}\right]}\,, \tag{4.32}$$

and the polaron-to-bare particle population decay Γ_{PF} rate is finally given by

$$\Gamma_{\mathrm{PF}} \equiv -2Z_+ \mathrm{Im}[\tilde{\Sigma}(0, E_+)]\,. \tag{4.33}$$

4.2.6 Polaron coherence

The last property we need to fully characterize the repulsive polaron is its coherence, which is quantified by the quasi-particle residue Z [10] i.e. the squared overlap between the wavefunction of the polaron and the one of a non-interacting bare particle. In order

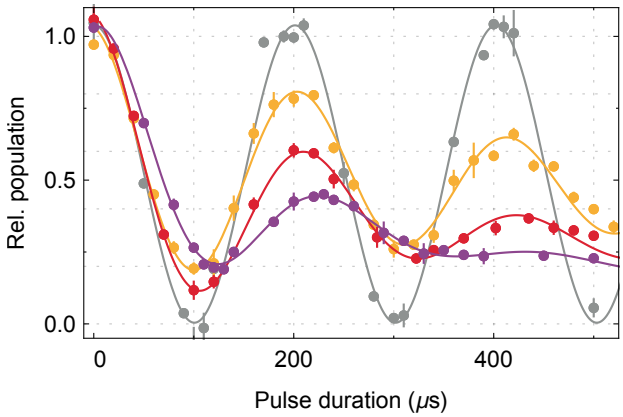

Figure 4.14: Examples of Rabi oscillation of the repulsive polaron for four different interaction parameters: $k_F a \simeq 0$ (gray circles), $k_F a \simeq 1.1$ (yellow squares), $k_F a \simeq 1.3$ (red circles) and $k_F a \simeq 3$ (purple diamonds). The solid lines shows the fit of the data using equation 4.38.

to experimentally probe this quantity we drive Rabi oscillations between the atomic state $|2\rangle$ and $|3\rangle$ with a resonant RF field. As shown in Figure 4.14, the populations of the two states will coherently oscillate at the frequency Ω, which is connected to the bare Rabi frequency Ω_0 and the quasi-particle residue by the equation [10]:

$$\Omega^2 \simeq \Omega_0^2 \left|\langle \Psi_2 | \Psi_3 \rangle\right|^2 \simeq \Omega^2 Z \tag{4.34}$$

The $\simeq$ symbol is not a strict equality because of the finite interaction between the atoms in state-$|1\rangle$ and state-$|2\rangle$. For $k_F a_{12} \ll 1$ we can estimate the contribution of the finite repulsion in the quasi-particle residue by means of the single particle-hole Ansatz (see Equation (4.7)). Using the explicit expression for the particle-hole terms

$$\phi_{\mathbf{qk}} = \sqrt{Z}\,\frac{T(\mathbf{p}+\mathbf{q}, E_\downarrow + \xi_{\mathbf{q}\uparrow})}{E_\downarrow - E_{\mathbf{pkq}}}, \tag{4.35}$$

we can write the overlap $\langle \Psi_2 | \Psi_3 \rangle = \Omega^2/\Omega_0^2$ as

$$Z_2 Z_3 \left(1 - \sum_{|q|<k_F} T^*(\mathbf{p}+\mathbf{q}, E_{\downarrow 3} + \xi_{\mathbf{q}\uparrow}) T(\mathbf{p}+\mathbf{q}, E_{\downarrow 2} + \xi_{\mathbf{q}\uparrow}) \frac{\Pi^*(\mathbf{p}+\mathbf{q}, E_{\downarrow 3}+\xi_{\mathbf{q}}) - \Pi(\mathbf{p}+\mathbf{q}, E_{\downarrow 2}+\xi_{\mathbf{q}})}{E^*_{\downarrow 3} - E_{\downarrow 2}}\right), \tag{4.36}$$

with the retarded pair propagator

$$\Pi(\mathbf{p}+\mathbf{q}, E_\downarrow + \xi_q) = \sum_{\mathbf{k}} \left(\frac{\theta(k-k_F)}{E_{\downarrow 3} - E_{\mathbf{pkq}} + i0_+} + \frac{2m_r}{k^2} \right) \tag{4.37}$$

The symbols Π^* and T^* denote instead the advanced pair propagator and T-matrix, respectively, while Z_2 and Z_3 denote the residues of state-$|2\rangle$ and $|3\rangle$ quasi-particles. This expression reduces correctly to two known limits. In particular when $a_{12} \to 0$ one gets the simple result $|\Omega/\Omega_0| = \sqrt{Z_3}$ [92]. For $a_{12} \to a_{13}$, instead, using the definition of the residue Z one obtains that $|\Omega/\Omega_0| = 1$.
Experimentally we can measure Ω by fitting the Rabi dynamics showed in Figure 4.14 with a damped sinusoidal function defined as:

$$\frac{N_2}{N_2 + N_3}(t) = \text{off} + A\cos(\Omega t)e^{-\gamma_R t} + Be^{-\Gamma t}, \tag{4.38}$$

where γ_R is the damping rate and Γ the quasi-particle decay. We finally obtain $|\Omega/\Omega_0|$ by normalizing the result by the base Rabi frequency measured by driving the $2 \to 3$ transition in absence of the state-$|1\rangle$ bath. The result is shown in Figure 4.15 as a function of the interaction parameter, together with the theoretical prediction given by (solid blue line). We can notice that the theory can qualitatively describe the reduction of the Rabi frequency up to relatively strong coupling.

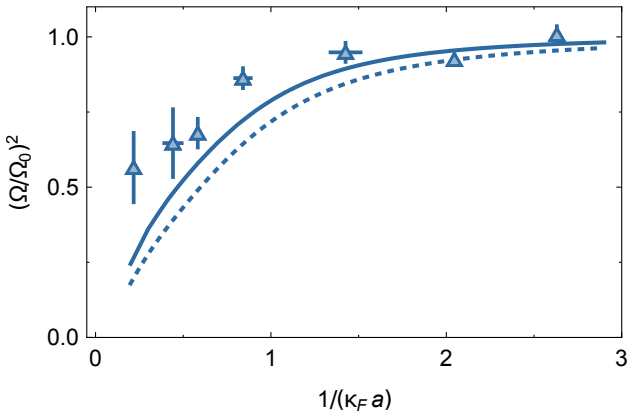

Figure 4.15: Ω^2/Ω_0^2 for the repulsive polaron as a function of the interaction parameter $1/(k_F a)$. The solid curve shows the prediction obtained within the ladder approximation (see equation). The dashed line shows the lowest order result $\sqrt{Z_2 Z_3}$

4.3 Conclusions

In this chapter we presented our experimental study of the repulsive Fermi polaron, a fermionic impurity interacting with a fermionic bath through a broad Feshbach resonance. We characterized the quasi-particle for a wide range of interaction parameter, from the unitary limit to the weakly interacting case. We measured its energy and effective mass, highlighting two instabilities of the many-body system for strong repulsion ($k_F a \sim 1$):

- The energy of the repulsive polaron exceeds the Fermi energy for $1/k_F a < 0.6$, which means that a spatial phase separation between the impurity and the bath is energetically favored with respect to the creation of the repulsive Fermi polaron, a clue of the presence of a ferromagnetic instability in the repulsive Fermi gas for strong interactions.

- The effective mass diverges and even changes sign when the interactions approach the unitary limit meaning that the Fermi liquid becomes thermodynamically unstable.

Finally, with lifetime and coherence measurements, we showed that the repulsive polaron it's well defined and remains coherent even at very large coupling strength. This motivated us to study the repulsive branch in a balanced mixture, which is the topic of the next chapter.

Chapter 5

N+N: many-body dynamics of the Repulsive Fermi gas

This is the main chapter of this thesis. Here we will describe a set of measurements we performed to understand the repulsive Fermi gas in a balanced mixture. Thanks to the spectroscopic technique described in the previous chapter we are able to quench strong repulsion on an initially weakly interacting Fermi gas, pushing the system out of equilibrium and populating the so-called repulsive branch of the many-body system. A soon as the interaction strength gets sufficiently high, $k_F a \sim 1$, the repulsive gas becomes extremely unstable and in a timescale of few Fermi times[1] it evolves to find a more energetically favored state. We observed that two different instabilities compete at the same time: on the one hand pairing processes bring the system in a molecular state, the ground state of many body-system also known as attractive branch. On the other hand, strong repulsion between different fermion pushes them away from each other driving the system into an anti-correlated state, possibly favoring the development of ferromagnetic spin domains. We probed this competition via pump-probe RF spectroscopy and density fluctuations measurement for a wide range of timescales finding out that both the two instabilities are participating together to the evolution of the system, the one affecting the other. Moreover, we found out that even after an evolution time of thousands of Fermi time the anti-correlated state formed in the initial stage of the dynamics still survives, preventing the system to completely reach the paired ground-state. The anti-correlation between the two fermionic populations corresponds in fact to a minimal overlap of the two wavefunctions respectively which drastically slows down the molecular formation.
The structure of this chapter can be described in these six points:

- Characterization of the upper branch of the many-body system in the balanced case: we spectroscopically measure the energy of the repulsive branch using RF spectroscopy. We found out that this branch is well defined up to very strong interaction, $k_F a \sim 2$, and for relatively low degeneracy, $T \sim 0.8 T_F$.

- In analogy with ultrafast pump-probe experiments in solid state [12, 13] we use two RF pulses to first quench the system out-of-equilibrium into the repulsive branch and then to probe its evolution in time. This technique allowed us to probe the

[1] The Fermi time is namely the minimum collective response time in interacting fermionic systems [64] and it is defined as $\tau_F = \hbar/\varepsilon_F$. In the context of this thesis the typical Fermi energy of the system is around 8 kHz in h units, which correspond to a Fermi time of $\sim 20\,\mu$s.

very fast dynamics of the system (few Fermi times) and measure the pairing and ferromagnetic rate for different repulsion strengths. Contrary to previous theoretical and experimental studies [5] we observed an interaction window, for $k_F a > 0.8$, in which the ferromagnetic instability is faster than the molecular formation.

- We probed the many-body system after tens of milliseconds of evolution time (thousands of Fermi time). Anti-correlations are found to survive, compatibly with the development of ferromagnetic micro-domains in the system. We exclude the role of the temperature to be dominant in the dynamics by studying the coherence property of the gas, probing the frequency of the Rabi oscillation and the spectral broadening in the probe spectroscopy.

- We monitored the density overlap between the unpaired atoms and dimers in the system, excluding the presence of macroscopic phase separation. Moreover, using the thermal gas of dimer as a thermometer, we are able to provide an upper-bound for the temperature increase of about a factor of four.

- We exploit atom number fluctuations and density-density correlations to set an upper-bound both on the domain size and on the temperature increase of the system. We observed a two-fold temperature increase and we exclude ferromagnetic domains with a size larger than few inter-particle spacings.

- We present the result of some extra measurements we performed to exclude trivial scenarios and to strengthen our understanding of the repulsive gas. We probed the effect of the presence of a third spin in the spectroscopy signal, the spatial dependence of the radio-frequency signal, and finally, we show a non-trivial behavior of the unpaired atomic population with respect to modifications of the bias magnetic.

5.1 Probing the upper branch in a balanced mixture

The starting point of this measurement is a $|1\rangle$-$|2\rangle$ Fermi mixing of about 2×10^5 atoms at a temperature of $T = 0.12(2)T_F$. The gas is confined by the cylindrical shaped optical dipole trap, described by harmonic frequencies of $\omega_x = 2\pi \times 19.7(2)$ Hz and $\omega_\perp = 2\pi \times 233(5)$ corresponding to the axial and radial directions respectively. Analogously to the polaron case described in the previous chapter, we probe the many-body energy spectrum of the system via radio-frequency spectroscopy, by transferring the atom from the hyperfine state-$|2\rangle$ to the state-$|3\rangle$.
The measurement sequence can be recapped in the following key points:

1. **Set the bias Feshbach field**, which define the interaction parameter of the $|1\rangle$-$|3\rangle$ mixture, $k_F a_{13} \equiv k_F a$. Scanning the magnetic field in a region between 600 and 700 G, we can control the repulsion strength from the non-interacting case to the unitary resonant one.

2. **Calibrate the zero energy** of a non-interacting Fermi gas, which corresponds to the Breit-Rabi splitting at the given field. The calibration consists in preparing a spin-polarized gas in the state-$|2\rangle$ by optically blasting away the state-$|1\rangle$ and performing a radio-frequency spectroscopy scan to find the resonance frequency between the states $|2\rangle$ and $|3\rangle$. As described in section 3.2.2 the duration of the RF pulse is 500 μs and its power is set to be a 0.8π-pulse. An example of this measurement is pictured as

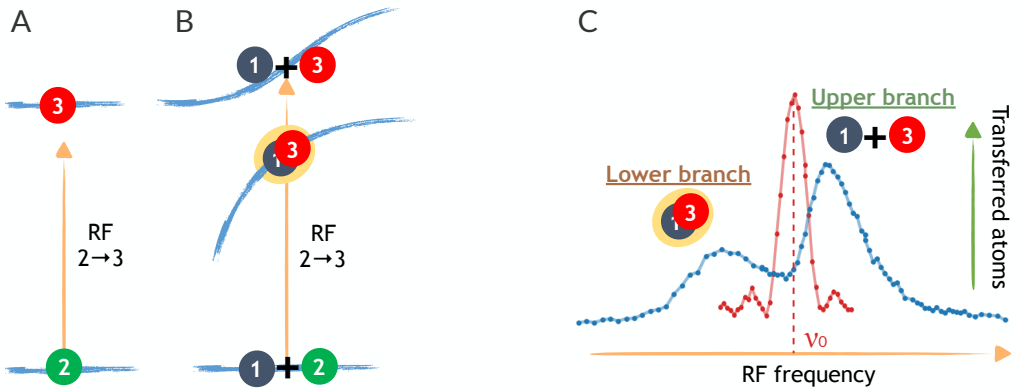

Figure 5.1: Sketch of the radio-frequency measurement scheme. **Panel A**: we first calibrate the Breit-Rabi splitting by performing an RF spectroscopy on a spin-polarized Fermi gas finding the non-interacting resonance frequency ν_0 (red data in **panel C**). **Panel B**: we then probe the energy spectrum of the many-body system by transferring the weakly interacting $|1\rangle$-$|2\rangle$ mixture to the resonantly interacting $|1\rangle$-$|3\rangle$. The spectroscopy signal (blue data in **panel C**) features two different peaks: the first, at negative detuning, correspond to the incoherent molecular association peak, while the second, at positive detuning, correspond to the repulsive atomic peak. The two peaks are a probe of the lower and the upper branch respectively.

the red curve in panel C of Figure 5.1. The resonance frequency, ν_0, is obtained by fitting the data via a Gaussian function[2].

3. **Probe the repulsive branch** of the $|1\rangle$-$|3\rangle$ many-body system via RF spectroscopy, starting from the weakly interacting $|1\rangle$-$|2\rangle$ mixture and scanning the frequency around ν_0. Any deviation from the non-interacting case is caused by interactions and represents the energy spectrum of the system. An example of a spectroscopy run is shown in blue in panel C of Figure 5.1 for an interaction parameter $k_F a \simeq 2.3$. In the signal one can identify the first two energy levels of the many-body system: at negative frequency, $\nu < \nu_0$, the attractive branch, at positive one, $\nu > \nu_0$, the repulsive one.

In order to extract the energy of the upper branch $\Delta_+ = \nu_+ - \nu_0$, we fit the repulsive peak position ν_+ through a Gaussian function. For very high interaction parameter, like the case shown in Figure 5.1, the molecular peak (lower branch) partially overlaps with the repulsive peak, therefore, we use a Gumbel function[107] to serve as a background. The full fitting function becomes:

$$S(\delta) = A_a \exp\left[\frac{(\delta - \delta_{0a})^2}{2\sigma_a^2}\right] + A_d \exp\left[-\frac{\delta - \delta_{0d}}{b} - a \times e^{-\frac{(\delta-\delta_{0d})}{ab}}\right], \tag{5.1}$$

where A_a and A_d are the amplitudes of the atomic and molecular peak respectively, δ_{0a} and δ_{0d} their center frequency, σ_a^2 is the atomic peak spectral width, finally a and b are phenomenological parameters of the Gumbel function which set its width and skewness.

[2]In order to fit the spectroscopy peak position, a Gaussian function is chosen over a the *sinc* function described in Section 3.2 because it is found to be more robust to noise and to give the same results within the fit uncertainty.

The Gumbel function is a well suited to phenomenological fit the incoherent molecular peak since it can catch its asymmetry with only one additional parameter with respect to a simple Gaussian.

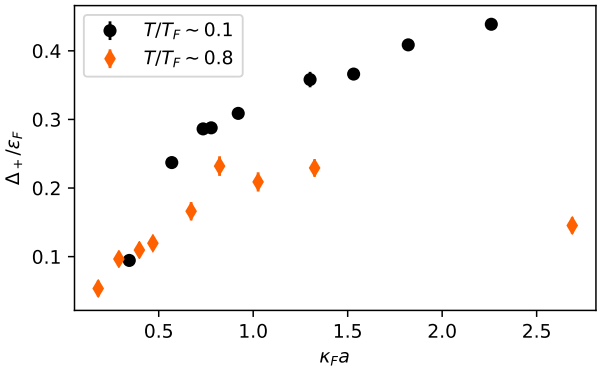

Figure 5.2: Upper branch energy as a function of the interaction parameter for two different initial temperature: $T = 0.12(2)T_F$ (black) and $T = 0.8(1)T_F$ (orange).

By repeating the measurement for different target bias magnetic field, we probe the upper branch energy as a function of the interaction parameter $k_F a$, normalized by the Fermi energy $\varepsilon_F/h \sim 8\,\mathrm{KHz}$. In Figure 5.2 we show the results obtained for two different initial temperatures: $T = 0.1T_F$ (in black) and $T = 0.8T_F$ (in orange). Very similarly to the impurity limit case, the repulsive energy increases monotonically with the interaction parameter and its slope decreases for $k_F a > 1$. In conclusion, we probed the existence of the upper branch for a balanced Fermi gas mixture up to very high interaction strength $k_F s \sim 2.6$ and we found that it exists even for a relatively low degree of degeneracy, at a temperature of $0.8T_F$.

5.2 Pump-probe spectroscopy

In this section I will describe how we study the evolution of the upper branch through pump-probe spectroscopy scheme. The technique consists in two different radio-frequency pulses: the first one quenches the system out of equilibrium into the upper branch, the second one, performed after a variable evolution time ΔT, studies the evolution of the system, monitoring both the decay into the lower branch and the interaction energy over time. By fitting the amplitude $A(t)$ and the shift $\Delta_+(t)$ of the atomic peak in the probe spectroscopy signal one can estimate the molecular fraction of the system and the presence of spin anti-correlations. For contact interactions, the RF shift is directly linked to the local pair correlator at zero distance $\langle \psi_1^\dagger(\mathbf{r})\psi_3^\dagger(\mathbf{r})\psi_3(\mathbf{r})\psi_1(\mathbf{r})\rangle$, where ψ_σ is the fermionic annihilation operator related to the state-σ [108]. Moreover, $\Delta_+(t)$ is proportional to the contact C [108], that quantifies the number of fermion pairs at short distance also in out-of-equilibrium systems [109, 110]. Therefore the RF shift is sensitive both to the development of short range anti-correlations and to the presence of magnetic domains in the system.

The pump pulse

The purpose of the pump pulse is to drive the system from the weakly interacting $|1\rangle$-$|2\rangle$ mixture to the repulsively interacting $|1\rangle$-$|3\rangle$ one. The RF frequency is set to match the

resonance between the $|2\rangle \rightarrow |3\rangle$ transition for each interaction strength, as described in the previous section. The RF power is set to the maximum experimentally available in order to minimize its duration and maximize the fraction of atom transferred from the state-$|2\rangle$ to the state-$|3\rangle$.

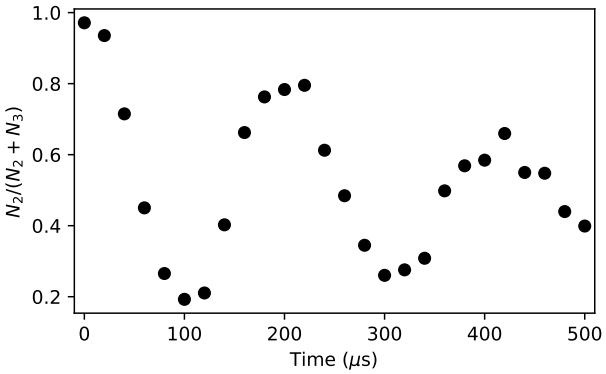

Figure 5.3: Rabi dynamics between the state-$|2\rangle$ and state-$|3\rangle$ population as a function of the pump RF pulse duration for $k_F a \sim 1.4$. The optimum pump duration is set to match the first minimum, in order to maximize the transfer efficiency.

In Figure 5.3 we show the population dynamics taking place when changing the duration of the RF pulse. The duration of the pump pulse is set to match the first minimum. The transfer efficiency is greater than 99% for low interaction parameter, but drops to around 70% for the highest probed $k_F a$ because of a higher collisional rate between state-$|1\rangle$ and state-$|3\rangle$ which causes appreciable damping of the Rabi oscillation. Moreover, similarly to the polaron scenario discussed in the previous chapter, the increased dressing of the repulsive quasi-particles reduces the Franck-Condon overlap between the initial and the final state reducing the associated Rabi coupling. The choice of reducing as much as possible the pump pulse length is motivated by the fact that part of the Rabi oscillation damping is independent on the RF power, hence, short high power pulses correspond to larger transfer efficiency. Moreover, if the pulse is too long, part of the evolution might take place already during the pulse itself and it would introduce an error in the definition of the zero time of the dynamics. In order verify that such an effect does not take place for the pulse settings we performed several spectroscopy measurements of the upper branch by keeping the interaction parameter fixed and varying the duration of the probe pulse from a minimum of 100 μs to a maximum of 2 ms. While the spectral width of the peak decreases increasing the probe time, given the smaller Fourier broadening, the position of its center does not change within the error of the Gaussian fit. In other words, we can not detect any evolution of the system happening during the pump pulse if its length is set under 2ms, which is always a fulfilled condition for the measurements presented in this work. As soon as the pump pulse is over we remove the remaining atoms in the state-$|2\rangle$ via a resonant optical blast. The blast does not change the short time evolution of the system[3] (within the first few ms), but avoid the three-body losses which deplete the atomic population at longer evolution time.

[3]This is confirmed by checking that the evolution of the repulsive peak (described in Section 5.4.1) is analogous both with or without the optical blast.

The probe pulse

Once we pumped the state-$|2\rangle$ atoms into the $|3\rangle$ state, the system populates the upper branch of the many-body energy spectrum. The $|1\rangle$-$|3\rangle$ mixture is interacting repulsively and the system evolves to minimize the repulsive energy. As already discussed in the introduction there are two possibilities: the first one is to create pairing correlations, forming molecules and reaching the lower branch, i.e. the ground state of the system. The second possibility is to build up anti-correlation between the $|1\rangle$ and the $|3\rangle$ atoms instead, lowering the spatial overlap between the two fermions, hence decreasing the interaction energy. We study the competition between these two phenomena by spectroscopically probing the $|3\rangle \rightarrow |2\rangle$ transition after waiting a delay time Δt from the end of the pump pulse. As shown in Figures 5.4 and 5.5 two things happen at the same time:

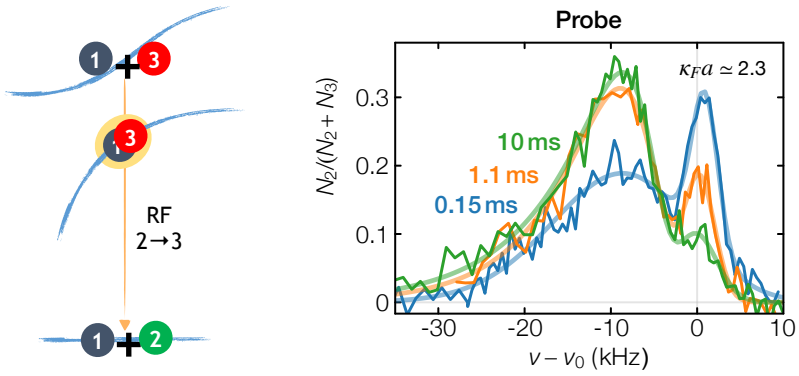

Figure 5.4: Probe signal at different evolution time Δt. The x-axis represents the detuning $\nu - \nu_0$, where ν_0 is the resonance frequency for a non-interacting Fermi gas. We show here spectra with high interaction parameter, $k_F a \simeq 2.3$, in order to have a good signal from the molecular dissociation. At lower values of $k_F a$, the binding energy of the dimers is much larger, shifting the peak to lower frequency and reducing drastically the transfer efficiency. In blue, we plot the spectra taken at the shortest evolution time, $\Delta t = 150\,\mu$s. The right peak corresponds to the $|3\rangle$ unpaired fermions, repulsively interacting with the state-$|1\rangle$ bath, which are transferred in the $|2\rangle$ weakly interacting state. The broad continuum on the left side corresponds to the incoherent dissociation of $|1-3\rangle$ dimers in $|1\rangle + |2\rangle$ free atoms. At longer evolution times, orange and green curves, the atomic peak decreases while the molecular one increases: the repulsive $|1\rangle + |3\rangle$ gas populating the upper branch is decaying in the lower branch forming $|1-3\rangle$ molecules. The solid darker lines connect the experimental points. The lighter lines show the fit of the data to the phenomenological model given by the sum of a Gaussian and a Gumbel function.

- The atomic peak at positive detuning decreases in time and a broad molecular continuum appears and grows at negative detuning. As one can see in the right panel of Figure 5.4, the spectra, similarly the one related to the pump pulse described in the previous section, presents two distinct features: thew incoherent broad molecular dissociation peak at negative detunings ($\nu < \nu_0$) and the repulsive atomic peak at positive ones ($\nu > \nu_0$). The three lines show different evolution times. For increasingly longer times the amplitude of the atomic peak decreases while the molecular one increases, signaling the decay of the population occupying the upper branch of the many-body system into the lower branch of $|1-3\rangle$ dimers.

- The atomic peak detuning $\Delta_+ > 0$ decreases in time, signaling the drop of the repulsive interaction energy felt by the state-$|3\rangle$ atoms. This drop might come from different physical mechanism: on the one hand, it could be explained in a mean-field framework, in which the atomic density of state-$|1\rangle$ and state-$|3\rangle$ atoms are locally constant and homogeneous, by the drop of the interaction parameter $k_F a$. While the scattering length a is fixed by the Feshbach magnetic field, the Fermi wave-vector depends on the atomic density ($k_F \propto n^{1/3}$), which is decaying because of the molecular formation. This hypothesis is completely ruled out in section 5.2.3, where we will show that the drop of atomic density is not nearly enough to justify the observed energy shift. A second possibility to explain the observed drop of energy is to release the mean-field hypothesis of constant and homogeneous density and allows the presence of spatial correlations between state-$|1\rangle$ and state-$|3\rangle$ atoms. In this new framework, even if the atomic density remains constant in time, the energy shift can be originated by a local spatial separation between the two states, which effectively gradually separates the system into two non-interacting Fermi gases, either via the development of spin anti-correlations or by the formation of magnetic domains.

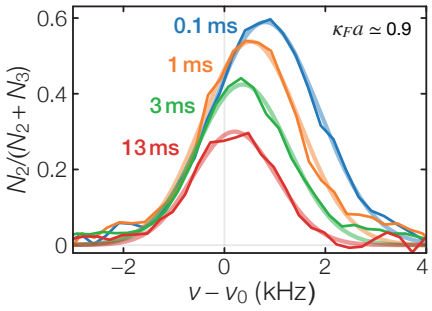

Figure 5.5: Evolution of the probe signal at $k_F a \simeq 0.9$. The repulsive atomic peak shows two kind of dynamics at the same time: its amplitude decreases, because of molecular formation (see Figure 5.4), and its center shift towards smaller frequency, which corresponds to a decrease of the interaction energy. The solid darker lines connect the experimental points. The lighter ones show the Gaussian fits to the data.

Extracting energy shift and relative atomic population from spectra

In order to quantify the timescales related to these two dynamics, we measure the evolution of the energy shift and of the unpaired atomic population. As for the pump, the atomic energy shift is quantified by performing a Gaussian fit of the repulsive peak to extract the frequency detuning $\Delta(t) = \nu - \nu_0$, with respect to the bare $|3\rangle \rightarrow |2\rangle$ transition, and the amplitude $A(t)$. For the highest interaction parameters probed, $k_F a > 1.6$, we again used a Gumbel function to remove the background given by the molecular peak while performing the Gaussian fit.
In order to connect the amplitude $A(t)$ of the atomic peak with the unpaired fermionic relative population, we need to consider that the probe spectroscopy pulse can not fully transfer all the atomic population from state-$|3\rangle$ to state-$|2\rangle$. This finite efficiency comes mainly from two reasons:

- The RF pulse time is set to match $\sim 0.8\pi$-pulse for a spin-polarized gas[4]. Hence,

[4]The choice of a pulse length of about 0.8π-pulse is made to avoid the risk of probing the system for

even without any molecule in the system, the amplitude of the atomic peak would be below one.

- The Rabi oscillation between the atomic population $|3\rangle$ and $|2\rangle$ is partially damped, which again would produce a signal < 1.

Because of this, in order to extract the actual fraction of unpaired atom, we need to calibrate the efficiency of the probe RF pulse for any given field. We introduce the efficiency calibration factor $\eta(k_F a)$, which is obtained by measuring the efficiency of a pump pulse ($|1\rangle - |2\rangle \rightarrow |1\rangle - |3\rangle$) where the RF pulse power and duration are chosen to match the 0.8π-pulse of the probe spectroscopy. The relative unpaired population $n(t)/n(0)$ at any given time is then calculated as the ratio between the peak amplitude of the repulsive atomic peak in the spectroscopy signal and the efficiency factor $\eta(k_F a)$:

$$\frac{\overline{n}(t)}{\overline{n}(0)} = \frac{A(t)}{\eta(k_F a)}, \tag{5.2}$$

In Figure 5.6 we plot the comparison between the decay of the RF shift (normalized by the Fermi energy) $\Delta_+(t)/\varepsilon_F$ and the one of the unpaired population $\overline{n}(t)/\overline{n}(0)$ for three different interaction parameters.

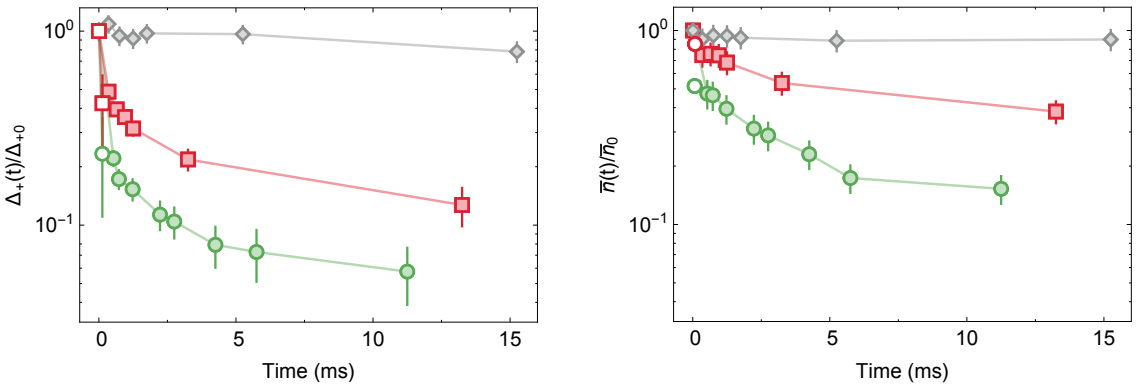

Figure 5.6: Evolution of the energy shift (**left panel**) and of the atomic unpaired population (**right panel**) for three increasing interaction parameters: $k_F a \simeq 0.35$ (gray diamonds), $k_F a \simeq 0.78$ (red squares) and $k_F a \simeq 1.53$ (green circles). The shift is normalized to the Fermi energy ε_F, while the fermionic population by the population transferred by the pump pulse in the $|3\rangle$ state. For low interaction strength, gray dataset, neither $\Delta_+(t)/\varepsilon_F$ nor $\overline{n}(t)/\overline{n}(0)$ evolve in time: the weakly repulsive $|1\rangle$-$|3\rangle$ mixture is practically stable. For higher interaction strength, red and green datasets, the population of uncoupled atoms drops and reaches an almost steady state of about $15 - 20\%$ of its initial value. The energy shift decreases even faster, dropping below $0.1\varepsilon_F$ within the first millisecond of evolution time.

For low interaction strength, the evolution is really slow, and the system is basically stable in the weakly $|1\rangle$-$|3\rangle$ mixture. For increasingly larger $k_F a$s the upper branch becomes instead very unstable: the unpaired fermionic population drops because of pairing and the energy shift decreases with an even faster rate. In order to better compare the very initial dynamics taking place at different interaction strengths, we will now focus on the first few Fermi times of evolution and extract both a pairing and a ferromagnetic rate.

a time longer than a π-pulse, which causes a distortion in the spectroscopy signal shape, degrading the quality of the fit.

5.2.1 Short time pairing vs anti-correlations

For interaction parameters $k_F a > 1$, the evolution of the atomic peak is really fast: the energy shift and the atomic density changes drastically already within the first few Fermi times. Our standard spectroscopy pulse has a duration of 500 μs, which has a limited time resolution if compared to the evolution timescales of the system after the quench, which are of the order of the Fermi time τ_F ($\sim 20\,\mu$s in our system). Employing a relatively long RF pulse we can not be sure that the dynamics of the system is completely frozen as soon as the probe pulse begins or if it continues to evolve during a fraction of it. Since our goal is to extract the evolution rate Γ of the generic quantity S[5], which is estimated as the first derivative of S with respect to the evolution time Δt,

$$\Gamma = \frac{\Delta S}{\Delta t}, \tag{5.3}$$

to minimize the experimental error on Γ, we need to balance the relative error on ΔS and on Δt. In order to improve the time resolution, we adjusted our spectroscopy protocol by reducing the probe RF pulse duration. This comes with a price both on the spectral resolution and on the signal to noise ratio, increasing the experimental error on the estimation of S. The reason is that a shorter pulse, on the one hand, introduces a larger Fourier broadening and on the other, even using the maximum RF power available in our setup, causes a substantial reduction of the transfer efficiency from the state-$|3\rangle$ to the state-$|2\rangle$. The best compromise we found is to adopt RF pulses durations between 50 μs and 100 μs. Within this range we achieve transfer efficiency for the probe spectroscopy as large as 15% and a spectral width of 10 KHz as shown in Figure 5.7. The combination of these two effects corresponds to a fitting error in the determination of the peak frequency of about 350 Hz, which is 5 times bigger if compared with our standard scheme corresponding to probe pulses ranging from 250 and 500 μs.

Using this probe procedure, we study the very short time evolution of the system as a function of the interaction parameter. In this set of measurement we limit the interaction strengths from $k_F a \simeq 0.4$ to $k_F a \simeq 1.6$ because, for higher interaction strengths, the poor signal and the low spectral resolution do not allow us to clearly resolve the atomic spectral contribution from the molecular one, making unfeasible a precise determination of the position of the peaks. In order to quantify the relative speed of the pairing processes compared to the formation of anti-correlations, we perform a linear fit both on the evolution of the relative unpaired population, $\overline{n}(t)/\overline{n}(0)$ and on the evolution of the energy shift $\Delta_+(t)/\varepsilon_F$. The slope obtained by the fit, Γ_{pairing} and Γ_{FM}, estimate the first derivative of $\overline{n}(t)$ and $\Delta_+(t)$ within the first Fermi time of evolution and allows to quantitatively compare the speed of the two processes[6].

In Figure 5.8 we plot the obtained pairing and ferromagnetic rates expressed in the unit of the inverse of the Fermi time $\tau_F^{-1} = \varepsilon_F/\hbar$. For low interaction parameters, they both are

[5] S can can be any observable in the system, e.g. the frequency shift or the amplitude of the spectroscopy signal relative to the repulsive peak

[6] The choice of linear fitting over other possible decay models, such as e.g. exponential, is motivated by the fact that it provides model-independent rates. An exponential fit to data at all times would greatly underestimate the initial rates, characterizing the extremely fast initial dynamics at strong coupling. Moreover it would imply the existence of only one relevant timescale in the evolution, which is not the case because of the interplay between the growth of anti-correlations and the pairing: on the one hand the anti-correlations slow down the pairing process reducing the spatial overlap between $|1\rangle$ and $|3\rangle$ particles wave-function, hence reducing the coupling probability.

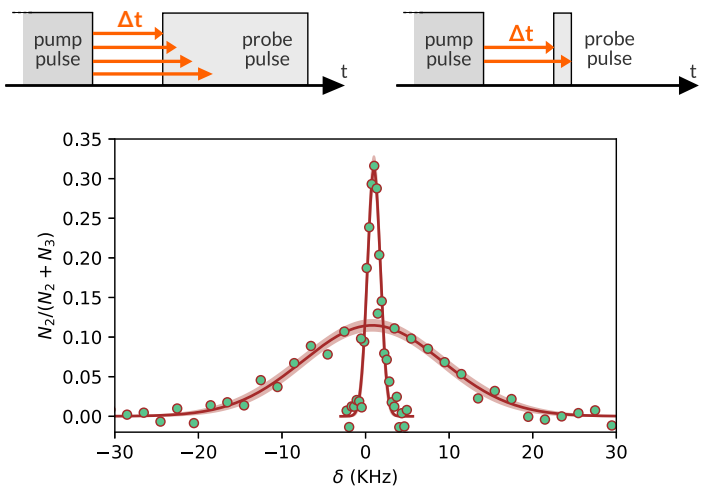

Figure 5.7: Sketch of the trade-off between time and spectral resolution for different durations of the probe pulse. **On the top panel** the intuitive illustration of the reason why a shorter RF probe pulse reduces the uncertainty on the waiting time. The dynamics of the many-body system is not necessary frozen already at the beginning of the probe but might continue for a fraction of it. **On the bottom panel** the comparison between the spectroscopy signal obtained with a $50\,\mu$s and a $500\,\mu$s long probe RF pulse. The red curves show the Gaussian fit on the experimental data, together with the fit 95% confidence interval (shaded region). Because of the short duration of the probe, the width of the peak is greater than 8 KHz (Gaussian σ^2) due to Fourier broadening. The fitting error of the peak center is of the order of 350 Hz, more then 5 times less accurate if compared with the 50 Hz uncertainty given by the standard spectroscopy procedure.

very small, describing a system that is almost stable. As soon as $k_F a$ approaches one, both Γ_{pairing} and Γ_{FM} increase and, in a window between $k_F a = 0.8$ and $k_F a = 1.3$ the latter becomes twice as big as the first one. In this interaction window, the short-time dynamics is dominated by the formation of anti-correlation, corresponding to a very fast drop of the interaction energy $\Delta_+(t)/\varepsilon_F$ already in the first $50\,\mu$s of evolution time.

It is important to notice that with a probe RF pulse length of $50\,\mu$s and a minimum waiting time of $10\,\mu$s, the highest measurable rate with a linear fit is $\Gamma_{\text{max}} \sim 0.4\tau_F^{-1}$, which corresponds to the hypothetical slope which would be measured if the energy shift or the atomic unpaired population were already zero after $60\,\mu$s. When the fitted rates approach this value, they should be regarded as the lower bound to the actual one. The extracted rate for the pairing process is found to be in really good agreement with the three-body recombination theory introduced in Reference [63], which, adapted for the case

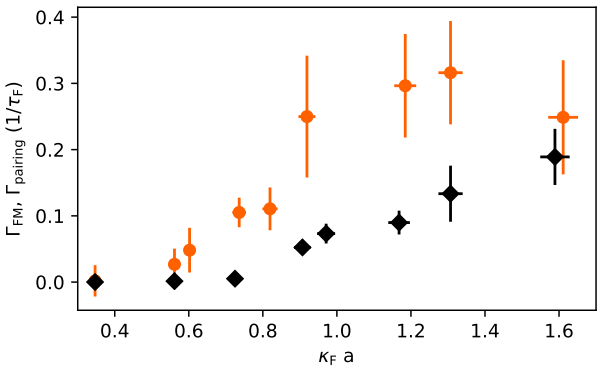

Figure 5.8: The pairing (black diamonds) and ferromagnetic (orange circles) rates as a function to the interaction parameter $k_F a$. The vertical error bars combine the standard error of the linear fit with the uncertainty in determining the Fermi time τ_F.

of a balanced mixture, predicts a pairing rate given by[7]:

$$\tau_F \Gamma_3 = 2 \times 0.806 \times \frac{148}{(6\pi^2)^2} \frac{(k_F a)^6}{1 + (k_F a)^2}. \tag{5.8}$$

As shown in Figure 5.9 this theory and our experimental data match for almost 4 decades without the need of any adjustable parameter. Moreover, the ferromagnetic rate qualitatively agrees with the results obtained for a zero-temperature homogeneous Fermi gas via

[7]The three-body recombination process is a scattering event involving three particles, two of which in a different spin state with respect to the third. In the initial state all the particles are free, the final state consists in a dimer plus a free particle which carries out the excess of kinetic energy to ensure total energy and momentum conservation. In the limit of weak interactions, $K_F a \ll 1$, in which the mean collision energy of the particles remains lower than the binding energy of the molecule, the three-body recombination process can be described by the theoretical approach developed by Petrov in Reference [63]. In the limit of equal masses and broad Feshbach resonance of our system, one can write the number of recombination events ($\uparrow + \uparrow + \downarrow \rightarrow \uparrow\downarrow + \uparrow$ or $\uparrow + \downarrow + \downarrow \rightarrow \uparrow\downarrow + \downarrow$) per unit of time and volume as:

$$\alpha_{\uparrow\downarrow\downarrow} n_\uparrow^2 = \alpha_{\uparrow\uparrow\downarrow} n_\uparrow^2 = \alpha n_\uparrow^2 = 148 \frac{\hbar a^4}{m} \frac{\bar{\varepsilon}}{\varepsilon_r} n_\uparrow^2, \tag{5.4}$$

where $n_\uparrow$ is the density of $\uparrow$ (or $\downarrow$) fermions, ε their kinetic energy and ε_r the energy gained by the recombination into a dimer, which for a balanced gas can be expressed as $\varepsilon_r = 2/(ma^2) + 2\varepsilon_F$. If that all the atoms remain trapped after the collision we can write a rate equation for the unpaired fermionic density $n(t) = n_\uparrow(t) = n_\downarrow(t)$:

$$\dot{(n(t))} = \frac{dn(t)}{dt} = -2 \times 148 \frac{\hbar a^4}{m} \frac{\bar{\varepsilon}}{\varepsilon_r} n^3, \tag{5.5}$$

which at short times reads $\dot{(n(t))} \simeq -\Gamma_3 n(t)$, where we introduced the three-body recombination rate Γ_3:

$$\Gamma_3 \simeq 2 \times 148 \frac{\hbar a^4}{m} \frac{\bar{\varepsilon}}{\varepsilon_r} n_0^2, \tag{5.6}$$

where $n_0 \simeq n(t)$ at short time. By finally expressing the fermionic density in terms of the Fermi wave-vector and normalizing the recombination rate by the Fermi time we can rewrite Γ_3 as:

$$\tau_F \Gamma_3 = 2 \times 0.806 \times \frac{148}{(6\pi^2)^2} \frac{(k_F a)^6}{1 + (k_F a)^2}, \tag{5.7}$$

where the numerical factor 0.806 results from averaging the kinetic energy and the squared fermion density over the integration region as described in Section 4.2.2.

a T-matrix approach developed in Reference . The same agreement is not found in the pairing rate predicted using the same method, which is much faster than the measured one. A possible reason for the mismatch between the theoretical and experimental results is the difference in the quench protocol used to introduce the interaction in the system. While the experimental quench is spectrally selective, i.e. the system is initially pumped only in the upper branch, the quench used in Reference is an instantaneous projection of a non-interacting Fermi gas onto all available (both atomic and molecular) many-body states. Therefore, even at zero evolution time, the molecular population is already different from zero. This contrasts with the experimental procedure and does not take into account the possibility that the anti-correlations can effectively slow down the molecular formation by reducing the contact, i.e. the wave-function overlap between the state-$|1\rangle$ and the state-$|3\rangle$ fermions.

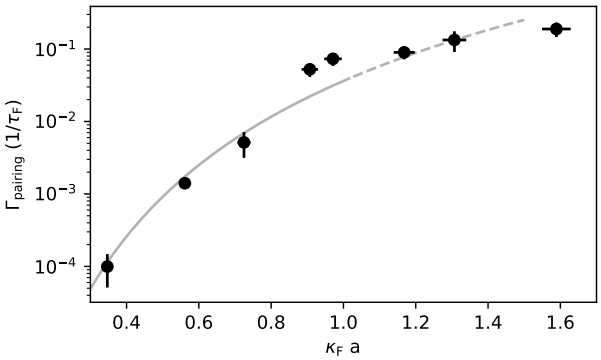

Figure 5.9: Comparison between the measured pairing rate (black dots) and the three-body recombination theory developed in reference [63] (gray line).

5.2.2 Long time evolution

The short time analysis described in the previous section showed us that the pairing and the ferromagnetic instabilities of the upper branch participate to the evolution of the system with similar timescales. We will now focus on how the interplay between them affects the properties of the many-body system at longer evolution time. As one can see in Figure 5.6, for $t \gg \tau_F$ the dynamics of the unpaired atomic population and of the energy shift slows down and almost halts, leaving the system in a metastable state.
In order to compare the evolution corresponding to different interaction parameters, we introduce two new quantities, Δ_{+LT} and n_{+LT}, the average in the time window between 10 and 30 ms ($\sim 500 - 1500\tau_F$) of Δ_+ and n_+ respectively. In Figure 5.10 we plot them, normalized by their correspondent value at zero evolution time, Δ_{+0} and n_{+0}.
For interaction strengths $k_F a > 1$ the energy shift is found to drop by more than 90% of its initial value, while more than $15 - 20\%$ of the uncoupled atomic population survives. In order to understand this behavior we will consider four different scenarios which can possibly explain why the energy shift remains very low in the long evolution time limit:

- Due to the initial repulsion the system develops anti-correlations (or spin-polarized micro-domains) which survive in time in a sort of emulsion metastable state of atoms and dimers.

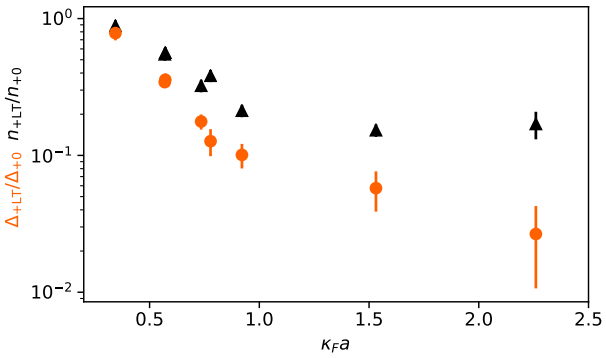

Figure 5.10: Relative fermionic population n_{+LT}/n_{+0} (black triangle) and interaction shift $\Delta_{+\mathrm{LT}}/\Delta_{+0}$ as a function of the interaction shift (orange circles). The long-time (LT) subscript corresponds to the averaging of the two quantities within the evolution time window $10 < \Delta t < 30\,\mathrm{ms}$. For $k_F a > 1$ the energy shift drops to less than 10% of its initial value, while the uncoupled fermion population does not decrease below $15 - 20\%$, reaching a sort of equilibrium. The error-bars include the contribution of the all the fitting error together with the statistical error given by the standard deviation of the mean of the experimental points comprised in the LT time window.

- Because of the molecular formation, the density of the unpaired fermions drops, leading to a reduction of the interaction energy. In a mean-field picture, considering instantaneous thermalization, the interaction energy $k_F a$ would decrease as $n^{1/3}$, where n is the unpaired atomic density.

- The release of the binding energy during the molecular formation process causes the heating of the system increasing the average collision energy. As discussed in Section 3.2.4 of Chapter 3 this would reduce the scattering amplitude, hence, the effective interaction strength.

- A macroscopic phase separation of atoms and dimer would push the uncoupled fermions in the wings of the density distribution, leaving the molecules in the center of the trapping potential. The probed fermions, therefore, occupy a spatial region of both lower density and lower degeneracy, potentially explaining the drop of the observed energy shift.

In the following, we will describe all the additional analysis and experiments we performed to understand what is the relative importance of these four physical phenomena in the dynamics of the energy shift we observe in our system. We will see that the first scenario is more relevant, while the others only give negligible contributions to the evolution of the system.

5.2.3 Incompatibility of the long-time spectral response with simple density reduction of the Fermi liquid

In this section we will show that the drop of the atomic density caused by the molecular formation can not explain the energy shift drop. In order to understand the role of the density in the interaction shift we introduce two new quantities, the instantaneous Fermi

energy $\varepsilon_F(t)$ and the instantaneous interaction strength $k_F(t)a$ defined as:

$$k_F(t) = k_F \left(\frac{n(t)}{n_0}\right)^{1/3}, \tag{5.9}$$

$$\varepsilon_F(t) = \varepsilon_F \left(\frac{n(t)}{n_0}\right)^{2/3}, \tag{5.10}$$

where n_0 is the unpaired atomic density at zero evolution time, $n_0 = n(0)$. Using this renormalization we can present the evolution dynamics of the shift and the interaction strength in a parametric plot in which the unpaired density is the variable parameter, instead of the time.
First of all we plot the measured energy of the upper branch Δ_{+0} measured in section 5.1 (cross symbols in Figure 5.11). For a fixed temperature, within the normalization introduced by the equations 5.9 and 5.10, it provides a universal relation between the k_Fa and the interaction energy. In other words, starting from any given point of the Δ_+-k_Fa phase space which lies on the pump data (purple circle marked as A), if the evolution of the interaction shift was described by the drop of the density n, we would expect the evolution to coincide with the measured shift at lower interaction strength (marked as B).

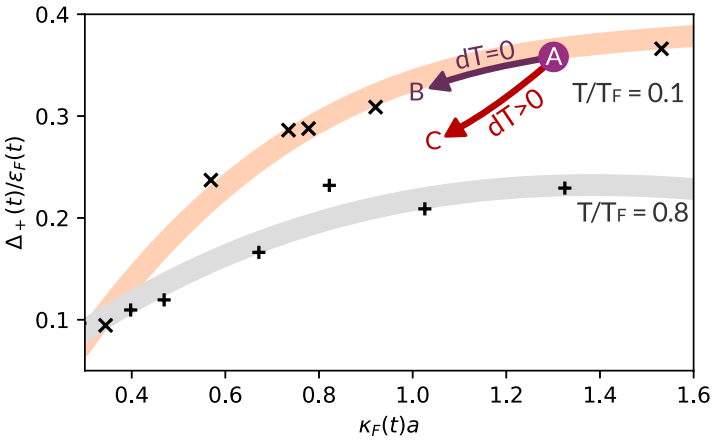

Figure 5.11: Upper branch energy as a function of the interaction parameter for two different initial temperature of the system: $T = 0.12(2)T_F$ (cross symbol) and $T = 0.80(5)T_F$ (plus symbol). The orange and gray solid lines are guides to the eye for the two temperature respectively (obtained with a polynomial fit of third degree). An example of energy shift evolution given by the drop of unpaired fermions density is sketched for an initial $k_Fa \simeq 1.3$. The starting point is represented by the purple circle (marked as A). The evolution driven by the loss of the atomic density n at constant temperature is sketched by the violet arrow, which leads to points (e.g the one marked as B) belonging to the upper branch spectra (orange line). If the temperature increase caused by molecular formation is taken into account, one can expect evolution like the one described by the red arrow and leading to the point marked as C. If the temperature of the system during the dynamics remains below $0.80(5)T_F$, all the possible points describing the evolution of the system, solely driven by the drop of atomic density and increase of temperature, have to be contained between the orange and the gray lines.

This would be strictly true in a mean-field picture in which the temperature of the system remains constant. If we want to take into the account for the heating due to the three-body

recombination, we need to consider that, as discussed in Section 3.2.4, the increase of the average collision energy effectively reduces the interaction parameter. We experimentally calibrate this effect by repeating the measurement of $\Delta_{0+}(k_F a)$ for a much higher initial temperature of the system corresponding to a degeneracy of $T/T_F = 0.80(5)$ instead of $T/T_F = 0.12(2)$ (plus symbols in Figure 5.11). As one can see, because of the higher kinetic energy, the shift drops by about a factor two. Considering that the chosen temperature $T = 0.80(5)T_F$ is an over-estimation of the actual increase of temperature we expect in our system, which is about a factor two as estimated in Section 5.2.8, the observed unpaired atomic density drop could only explain a drop in the energy shift following a similar path to the one described by the arrow going from point A to point C, as sketched with the red arrow. In the scenario in which the atomic density remains homogeneous, all the points describing the evolution of the system are expected to be strictly above the threshold given by the very high-temperature limit. Our observation completely rules out this hypothesis: as shown in Figure 5.12, for initial $k_F a > 0.8$, the drop of the energy shift is completely inconsistent with the lower-bound given by spectral response measured at high temperature. As we can see already the first point (empty symbols) after the pump (solid symbols) is completely out of the lower boundary given by the upper branch energy corresponding to a temperature $T = 0.80(5)T_F$ (lower edge of the shaded region). We, therefore, conclude that the drop of the unpaired fermionic density, together with the increase of the temperature due to three-body recombinations, is not nearly enough to explain the measured drop of the interaction shift, therefore, we exclude this mechanism to be extremely relevant to the evolution of the many-body system.

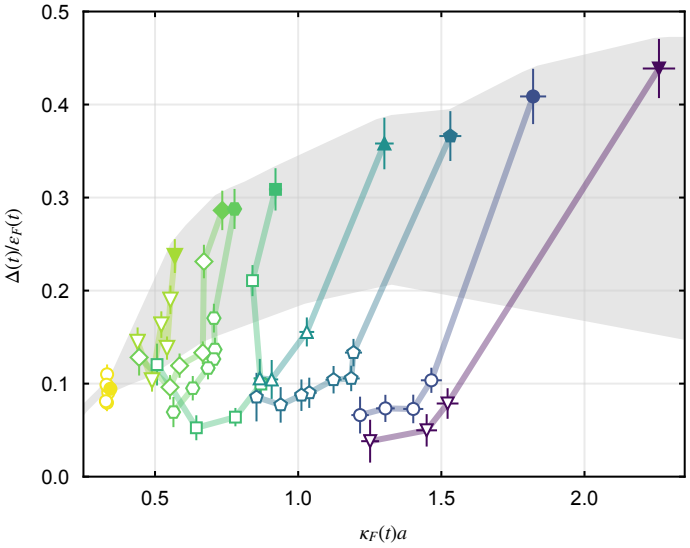

Figure 5.12: $\Delta_+(t)/\varepsilon(t)$ versus $k_F(t)a$ for different initial interaction parameter. The shaded region is the area between the energy of the upper branch measured with an initial temperature of the gas between $T = 0.12(2)T_F$ (upper limit) and $T = 0.80(5)T_F$ (lower limit). Full symbols show the upper branch energy shift while empty symbols the evolution of the system at an increasingly waiting time (i.e. decreasing unpaired atomic density) going from the top right to the bottom left region. Different colors represent different initial interaction strengths (the darker the color the higher the interaction strength). For $k_F a > 0.8$ the experimental points drops down below the bottom threshold, meaning that the drop of density cannot explain the drop of the interaction shift even with a 6-fold increase of the temperature.

5.2.4 Melting of the anti-correlated state

In order to further confirm that the temperature increase does not play a relevant role in the dynamics of the energy shift, we investigate the response of the system to slow changes of interaction strength. The idea is to quench the system to strong repulsive interactions, wait for the shift to drop and then externally lower the interaction strength by changing the scattering length a, and then monitor again the interaction energy. If the initial shift was caused by mean-field effects, such as the drop of the fermionic density of the increased collision energy, a reduction of the scattering length would necessary further reduce the measured energy shift Δ_+.

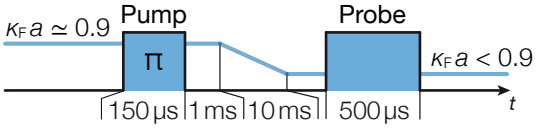

Figure 5.13: Sketch of the measurement scheme. The system is initially quenched to strong repulsion ($k_F a \simeq 0.9$). After waiting for 1 ms for the energy shift to drop, the Feshbach magnetic field is ramped down in 10 ms to reduce the scattering length. Finally the energy shift is spectroscopically probed.

The measurement sequence, sketched in Figure 5.13, can be summarized in four main

points:

1. We quench the system to an initial interaction strength $k_F a \simeq 0.9$. Here, the measured energy shift correspond to the upper branch energy (point **A** in Figure 5.14).

2. We let the system evolve for 1 ms in order for the energy shift to drop by 90% of its initial value (point **B**).

3. We lower the bias Feshbach field with a 10 ms ramp in the current, from 139 A to 136(134) A, which corresponds to a drop of the interaction strength from $k_F a \simeq 0.9$ to $k_F a \simeq 0.6$ and 0.4.

4. We wait 10 additional milliseconds in order for the magnetic field to stabilize and measure again the energy shift. The results correspond to the points **C** and **D**.

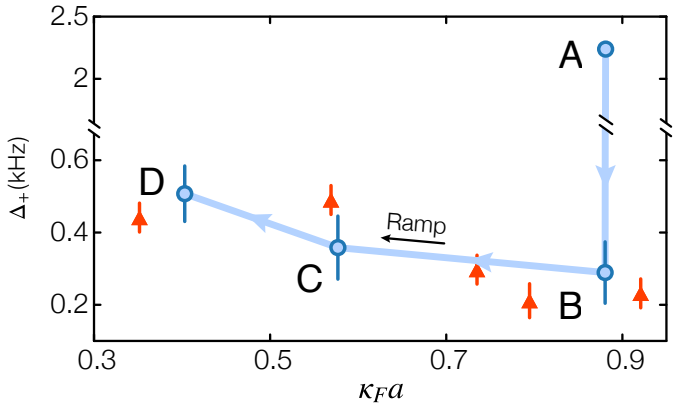

Figure 5.14: Anti-correlation melting experiment sequence: we start by quenching the system to $k_F a \simeq 0.9$ (point **A**), then we wait for the energy shift to drop below 10% of its initial value (point **B**). At this point, we ramp down the Feshbach magnetic field, decreasing the scattering length, hence the interaction parameter, in 20 ms. The measured interaction shift (points **C** and **D**) increases, suggesting that the anti-correlated state formed after the quench is not supported anymore by the lower repulsive interactions and melts. The spatial overlap between the two fermionic species increases and so does the interaction shift, reaching the asymptotic value (red triangles) which is recorded after a long evolution time Δ_{LT} quenching the system directly to the target field. The error bars show the fitting error.

One can notice how Δ_+ (points **C** and **D**) increases back from its smaller value at $k_F a \simeq 0.9$ (point **B**). This observation is not compatible with a trivial mean-field explanation of the RF shift behavior. The reversibility of the interactions shift, despite partial (irreversible) atom-molecule conversion, points to believe that the state corresponding to point **B** is an interaction-driven anti-correlated state. The idea here is that, after the initial quench, the system develops anti-correlations which cause the drop of the interaction shift after just 1 ms. Then, as soon as we slowly ramp down the scattering length, the repulsion between state-$|1\rangle$ and state-$|3\rangle$ atoms becomes weaker and stops to support the anti-correlated state which melts. The two different fermionic states start to overlap again and the measured

interaction energy increases reaching the asymptotic value Δ_{LT} (red triangle in Figure 5.14).
This experiment helps to rule out the hypothesis that the drop of the interaction shift could be explained by an increase of the temperature in the system or by the drop of the atomic density. If that was the case, ramping down the interaction parameter would have only caused a further decrement of the interaction shift, which is the opposite scenario of the observed behavior.

5.2.5 Atom-dimer interaction effects on the spectroscopy signal

In the previous sections we did not consider that also the interactions between the remaining unpaired atoms and the formed dimers can also play a role in the measured radio-frequency shift. As shown in Figure 5.15 the contribution to the interaction energy can be also negative because, unlike the atom-atom interaction, the atom-dimer one admit an attractive p-wave scattering channel which dominates at large collision energy [75]. After a sufficiently long evolution time, as soon as there is a non negligible fraction of dimers in the system, the observed energy shift starts to depend on both the two contributions. If the average collision energy becomes sufficiently high because of the heating caused by the three-body recombinations, these two contributions, having an opposite sign, might cancel out with each other explaining the observed drop of the RF spectroscopy shift.

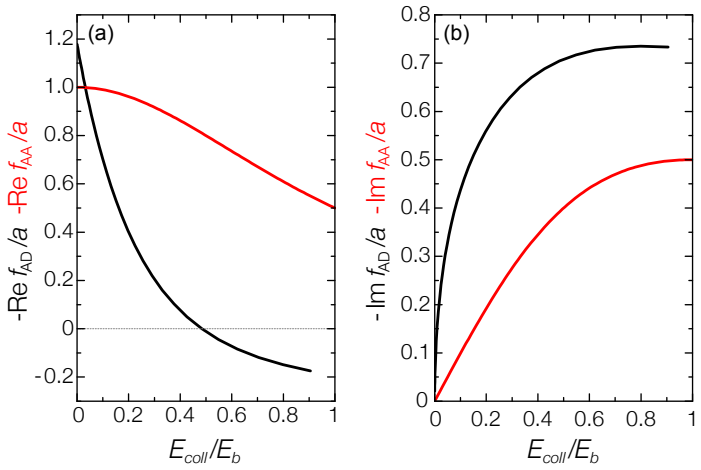

Figure 5.15: **On the left** panel the real part of the atom-dimer (black line) and atom-atom (red line) forward scattering amplitudes, normalized to the atom-atom scattering length a, as a function of the collision energy E_{coll} normalized to the dimer binding energy in the vacuum E_b (see Section 3.2.4). **On the right** panel the imaginary part of the atom-dimer (black line) and atom-atom (red line) forward scattering amplitudes, normalized to the atom-atom scattering length a, as a function of the collision energy E_{coll} normalized to the dimer binding energy in the vacuum E_b. The atom-dimer behavior is adapted from Reference [75]

.

We will now show that this is not a good interpretation of our data and that the scenario of a hot mixture of weakly interacting atoms and molecules is ruled out by the observed evolution of the atomic peak width. The idea is that the spectral broadening, unlike

the shift, monotonically increases with the collision energy both for atom-atom and atom-dimer interactions and therefore can be exploited to estimate the contribution of the higher collision energy in the system.
In Figure 5.16 we show the evolution of the spectral width of the atomic peak after the system is quenched to $k_F a \simeq 0.9$. The signal is normalized using the width measured width the same spectroscopy RF pulse on a non-interacting spin-polarized gas, which provides an estimation of all the technical broadening related to the measurement, mainly the Fourier broadening given by the final duration of the pulse. One can notice that the spectral width of the repulsive peak decreases in time and reaches, in the long-time limit, a value compatible with a non-interacting gas. This completely rules out the hypothesis of a hot mixture of atoms and dimer since it would have caused a broadening of the measured spectral width instead of a narrowing. Again, the simplest possible explanation is that anti-correlations between atoms in different spin states and molecules survive and the surviving unpaired fermions behave like nearly non-interacting isolated particles.

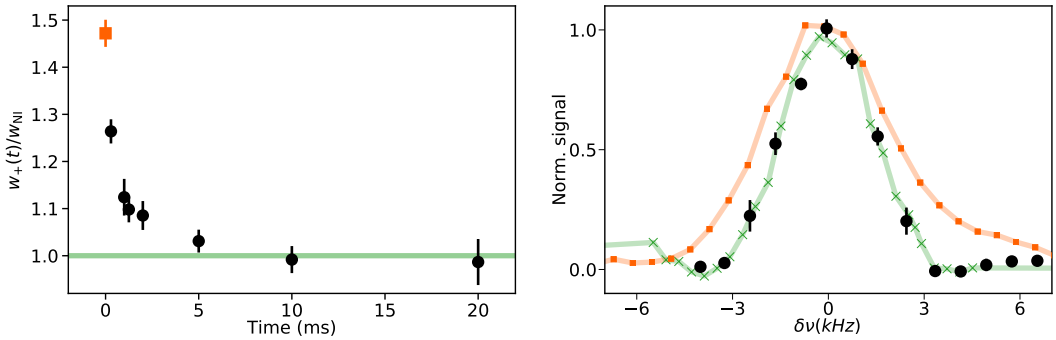

Figure 5.16: **On the left panel** the evolution of the spectral broadening of the atomic peak after the quench to $k_F a \simeq 0.9$. The spectral width is obtained via a Gaussian fit and it is normalized by the width measured with the same experimental sequence on a spin-polarized Fermi gas. Since the spectral broadening of the bare $|2\rangle \rightarrow |3\rangle$ transition is completely negligible at this level, this measurement quantifies all the technical broadening in our measurement, i.e. almost completely by the Fourier broadening related to the finite RF probe time. One can see that in about 5 ms of holding time the spectral width of the quenched system drops and reaches the one of an ideal Fermi gas. This is in agreement with the development of anti-correlation in the system and rules out the hypothesis of relevant heating of the gas. **On the right panel** the spin-polarized spectra (green solid line), the pump spectra (orange solid line) and the repulsive atomic peak after 10 ms of evolution time (black circles). The spectral properties of the anti-correlated system are almost indistinguishable from the one of an ideal Fermi gas. All the spectra shown in this panel are centered with each other to facilitate the comparison of the spectral broadening.

In Figure 5.17 we summarize the long-time behavior of the atomic spectral width for different interaction parameters, showing that quenching the system to higher interactions produces atomic states which resemble more and more to an ideal Fermi gas further confirming that higher repulsion builds up stronger anti-correlation in the system which effectively isolates the two spin components from each other.

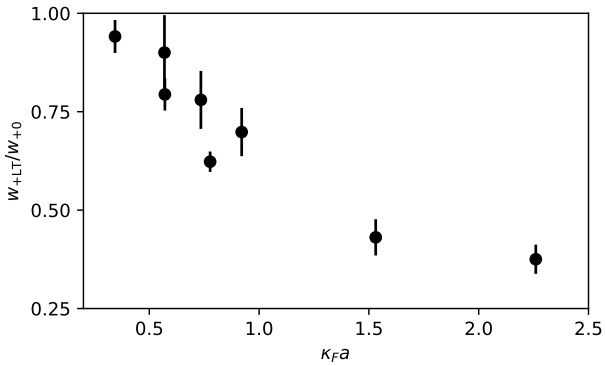

Figure 5.17: Ratio between the spectral width of the pump and the one of the system in the long time regime (average between 10 and 30 ms of evolution time). The error-bars represent the fitting uncertainty.

5.2.6 Rabi oscillation measurement on the anti-correlated state

Together with the observation of the decrease of the atomic peak spectral broadening discussed in the previous section, we present here an analogous observation in the time domain, which again points to the presence of anti-correlations surviving at long evolution time. The idea is the following: we quench the system to strong repulsion and we let the system evolve for 1 ms. Then we set the RF frequency to be resonant with the repulsive peak $\Delta_+(1\,ms)$ and its power to the maximum allowed by out experimental setup. Finally, similarly to what we have done when studying the lifetime of the repulsive polaron, as described in Section 4.2.5 of the previous chapter, we measure the Rabi oscillations between the state-$|3\rangle$ and the state-$|2\rangle$ and we fit the signal with the function:

$$f(t) = Ae^{-\Gamma_R t} + Be^{-\gamma_R t}\cos\left(\frac{\Omega t}{2\pi}\right), \tag{5.11}$$

where $\Omega/(2\pi)$is the Rabi frequency, γ_R is the damping rate and Γ_R is the excited population decay rate. In order to normalize the Rabi frequency, we repeat the experiment on a spin-polarized Fermi gas obtaining the non-interacting Rabi frequency Ω_0. In Figure 5.18 we plot the normalized Rabi frequency as a function of a detuning we apply to the RF pulse, immediately after the quench and with an evolution time of 1 ms, as soon as the energy shift has dropped almost completely.
With no holding time the ratio $\Omega/\Omega_0 \leq 1$, showing the expected behavior or the repulsive Fermi liquid regime, in which the renormalization of the quasi-particle coherence is encoded in a quasi-particle weight smaller than one [111]. Instead, after one millisecond of evolution time, the Rabi frequency matches the one of the ideal Fermi gas, confirming that the gas has developed anti-correlations and has started to behave more like an ideal Fermi gas. This observation is fundamentally related to the measured spectral broadening drop described in the previous section: they basically describe the same phenomena in the time and in the frequency domain.

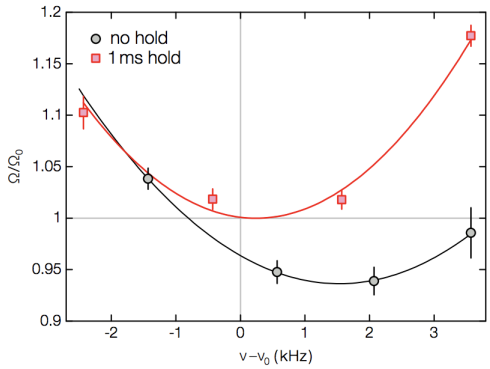

Figure 5.18: Normalized Rabi frequency as a function of the detuning from the bare Breit-Rabi energy. The gas is quenched to strong repulsion ($k_F a \simeq 2$) and Rabi oscillations are measured for different detuning immediately after the pump pulse (gray circles) and after 1 ms of evolution time (red squares). The Rabi frequency is extracted via a fit of equation 5.11 and it is normalized by the corresponding frequency measured on a spin-polarized Fermi gas Ω_0. The error bars represent the fit uncertainty. After 1 ms of evolution time the measured Rabi frequency matches the one of an ideal Fermi gas, suggesting the development of anti-correlations.

5.2.7 Macroscopic overlap between unpaired fermions and dimers

Up to now we implicitly assumed that the overall density distribution of the atomic and molecular parts share the same volume in the trapping potential. Here we will justify this assumption showing that they macroscopically overlap and no phase separation can be detected in the system. Since atoms and dimers can not be discriminated by our imaging, we use a radio-frequency pulse to selectively probe one of the two states in the following way:

- As usual, we prepare the system by waiting a time Δt after a quench to $k_F a \simeq 2.3$.
- We acquire a full spectrum comprising both the repulsive atomic peak and the molecular one, and we locate the corresponding resonance frequency $\Delta_+(t)$ and $\Delta_D(t)$ respectively.
- We probe the in-situ position of the atoms by transferring part of them from the state $|2\rangle$ to the state $|3\rangle$ with an RF pulse at $\Delta_+(t)$ and by imaging the state $|2\rangle$ immediately after.
- We probe the in-situ position of the molecules by dissociating part of them with an RF pulse at $\Delta_D(t)$ and imaging the state $|2\rangle$ immediately after.

In Figure 5.19 we plot on the left the probe spectra together with the fit used to extract the best resonant frequency for transferring atoms and dimers from the state-$|3\rangle$ to the state-$|2\rangle$ and, on the right, the density profile integrated along the axial direction both of the unpaired atoms (in blue) and of the dimers (in orange). Since the amplitude of the molecular spectra grows in time, while the atomic one decreases, we plot (in orange) a rescaled version of the atomic integrated density to match the amplitude of the molecular one in order to compare the two profiles more easily. One can notice that the two density profiles overlap quite perfectly, ruling out the possibility of macroscopic phase separation between atom and molecules.

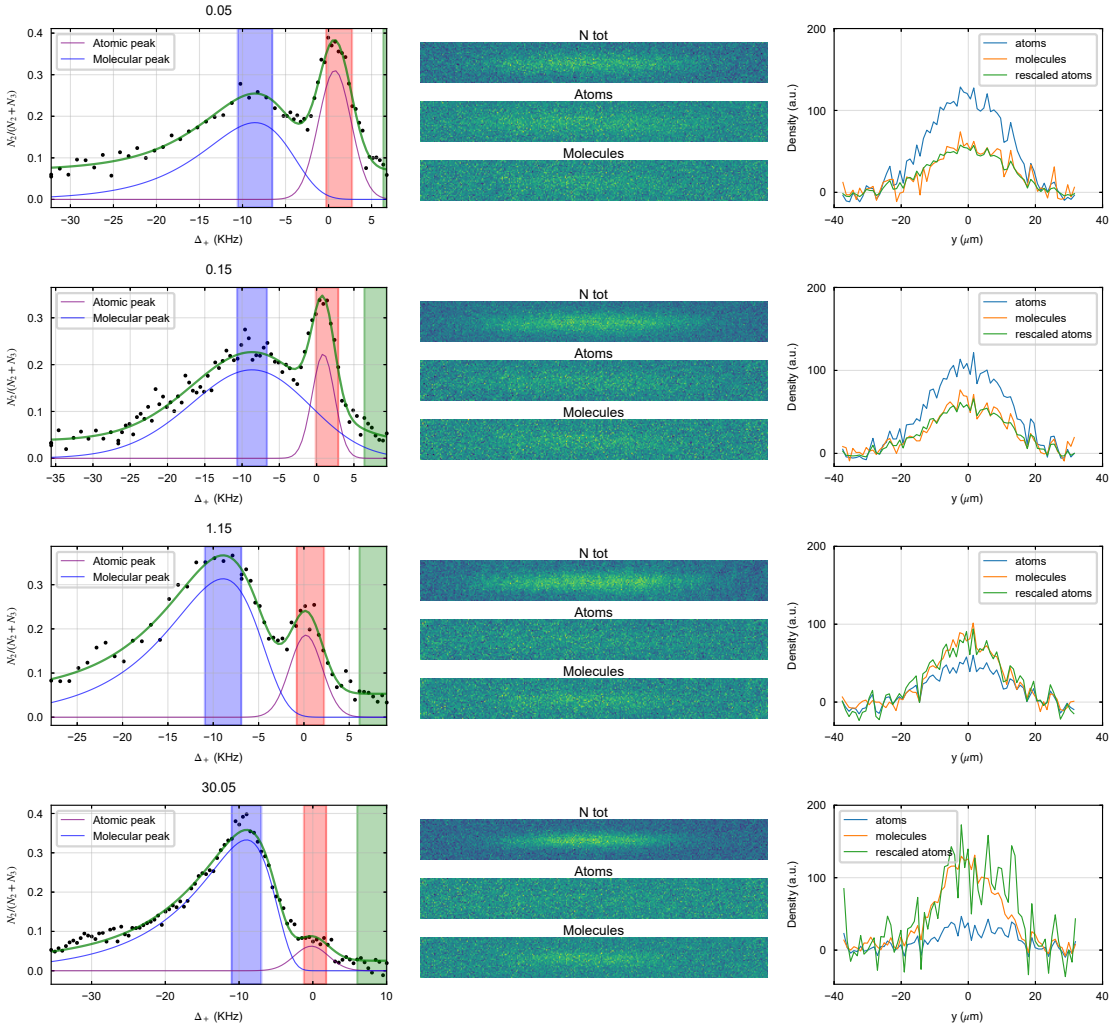

Figure 5.19: **On the left** the spectra of the many-body system with an increasing evolution time after the quench: 50 μs, 150 μs, 1.15 ms and 30 ms from top to bottom. The zero frequency $\Delta_+ = 0$ corresponds to the bare atomic transition, measured by probing the state-$|2\rangle$ to state-$|3\rangle$ transition on a spin-polarized Fermi gas. The molecular and atomic peaks are fitted with a sum of a Gumbel (shown in blue) and a Gaussian function (in purple). The overall best fit is plotted in green. **On the right** we plot the density profile integrated along the longitudinal axis of the cloud. The blue solid line corresponds to the unpaired atomic density, obtained by transferring state-$|3\rangle$ atoms to the state-$|2\rangle$ by applying an RF pulse with a frequency corresponding to the center of the Gaussian fit. The orange line is the density profile of the molecules, acquired in the same way but setting the RF frequency to the maximum of the Gumbel function. The green solid line shows the atomic signal with its amplitude rescaled to match the one of the molecules for easier comparison. Within the experimental accuracy, the in-situ profiles show an almost perfect overlap between the atomic and the molecular density profile, ruling out the possibility of macroscopic phase separation between the two. The profiles are obtained by averaging about 5 in-situ images in order to improve the signal to noise.

5.2.8 Temperature estimation from molecular density profiles

The molecular density profile extracted in the previous section can also be used to estimate the temperature of the system. In order to do this, we first assume that the molecules are in thermal equilibrium with the atoms, which is very likely after 50 ms of evolution time in the strong interaction regime. Moreover we assume that the molecular gas is thermal as confirmed by the lack of a Bose Einstein condensation signature in the system, e.g. the typical bimodal density profile. The thermal density distribution is therefore described by a Gaussian profile and can be fitted using the function:

$$n(x,y) = A \times e^{\frac{(x-x_0)^2}{2\sigma_x^2}} e^{\frac{(y-y_0)^2}{2\sigma_y^2}}, \tag{5.12}$$

where A is the amplitude, x_0 and y_0 the position of the center of mass, and σ_x and σ_y the widths from which the temperature can be extracted as:

$$T_{x,y} = 2\omega_{x,y}^2 \sigma_{x,y}^2 \frac{2m}{k_B}, \tag{5.13}$$

where $2\pi\omega_{x,y}$ are the axial and longitudinal trap frequencies respectively, $2m$ is the mass of a lithium dimer and k_B is the Boltzmann constant. By averaging the axial and the longitudinal temperature we obtain, independently from the evolution time (if longer than 10 ms), a temperature of about 160 nK. If we compare it with the initial temperature of about 45 nK corresponding to $T/T_F = 0.12$, we find a relative temperature increase between 3 and 4. This estimation has to be considered as an upper bound, in fact, because of the presence of anti-correlations in the system, the gas of dimers might occupy a larger volume due to unpaired fermions repulsion, which would result in a higher $\sigma_{x,y}$ and therefore a higher estimation of the temperature. Nevertheless this result is extremely valuable to validate the choice of a temperature $T = 0.8T_F$ as the lower bound for the shifts shown in Figure 5.11 of section 5.2.3.

5.3 Spin density fluctuations

In the previous sections we showed how the interplay between the pairing and the ferromagnetic instabilities give origin to an atom-dimers mixture in which the inter-particle interaction energy is minimized by the development of spin anti-correlations. In this section we will present our measurements aimed to understand if anti-correlations promote the formations of ferromagnetic domains. Through the analysis of the density fluctuations we will be able to exclude the presence of macroscopic domains bigger than few hundreds of particles, moreover we will be able to provide us an upper-bound to the increase of the temperature in the system after the quench, confirming the results of the previous section.

5.3.1 Atom number variance

The direct observation of spin domains is very challenging in a 3D geometry. Small domains with a size of few inter-particle spacing are undetectable with in-situ absorption imaging because of the density integration along the line of sight of the imaging system. Still, as described in Section 3.3.8 it is possible to probe their presence by studying the spin density fluctuations. Spin domains in the system increase the shot to shot local fluctuations, which can be measured with a good time resolution during the evolution of the system after

the quench and with a decent spatial selectivity. This allows us to study separately the dynamics that happens in the center of the cloud from the one taking place on the low-density wings. Since the estimation of the absolute values of the atom number variance is very difficult and requires a non trivial calibration performed on a spin-polarized Fermi gas, in this section we will never draw conclusions based on this number alone, but we will always compare the results obtained in two very different regimes: the very weakly interacting mixture at $k_F a \simeq 0.3$ and the strongly repulsive one at $k_F a \simeq 1.3$.

Effect of spin domains on the variance

A visual way to understand how the presence of spin domains in the system affects the atom number fluctuations is to consider a simple model in 2D. Let us consider a density slice of the atomic cloud and name it $N_{x,y}$. The integration related to the absorption imaging technique corresponds to the integration along the y-axis of the density slice, which results in the 1D vector N_x:

$$N_x = \sum_y N_{x,y}, \tag{5.14}$$

where the summation is performed over all the vertical pixels.

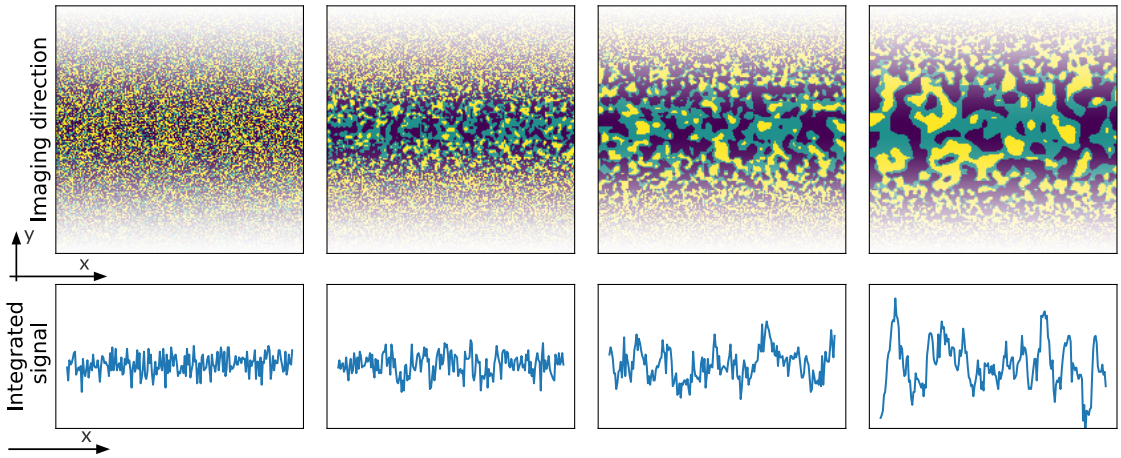

Figure 5.20: Visualization of how the presence of spin domains affects the number of atom variance. From left to right slices of density profiles containing atomic and molecular domains with increasingly larger size. The color yellow corresponds to state-$|1\rangle$ atoms, the blue-green to $|1-3\rangle$ dimers and the dark blue to state-$|3\rangle$ atoms. On the bottom, the integration of the profiles along the vertical direction, setting to 0 the value of the pixels containing state-$|1\rangle$ atoms and to 1 the one containing state-$|3\rangle$ atoms and molecules. The vertical scale is unchanged between the four plots. One can see that the presence of domains drastically increases the density noise, hence the atom number fluctuation. The bigger are the domains, the higher are the fluctuations.

In Figure 5.20 we show four different examples of density slices in the presence of domains of growing size (from left to right). Yellow regions represent atoms in state-$|1\rangle$, dark blue regions atoms in state-$|3\rangle$ and blue-green regions $|1-3\rangle$ dimers. Our imaging is set to be resonant with state-$|3\rangle$ atoms, which includes also the molecular state, therefore, our probed quantity is the gas density with some holes created by the state-$|1\rangle$ atoms. The integrated signal is shown in the second row of the figure. Since the domain position

varies in different experimental realizations, the measured number variance of each pixel increases with their presence and grows with their size. In order to quantify this behavior, we generate $K = 100$ different density slices varying the domain size from 1 to 30 pixels. We name them $N_{x,y}^{k,s}$, where k is the realization index and s the domain size[8]. We integrate along the y direction each set, we compute the variance over the k index and finally we average over the x direction to obtain the number variance associated with the domain size s:

$$\frac{(\Delta N)^2}{N}(s) = \sum_x \left(\frac{1}{\overline{N}_x^s} \sum_k^K \frac{(N_x^{k,s} - \overline{N}_x^s)^2}{K} \right), \tag{5.15}$$

where $\overline{N}_x$ is the mean of the integrated profile N_x^b over the K realizations. From the results plotted in Figure 5.21 one can see that the number variance grows almost linearly with the s except for a saturating behavior for the largest domain size, which appear as soon as s approaches the finite size of the system. In conclusion, although the model

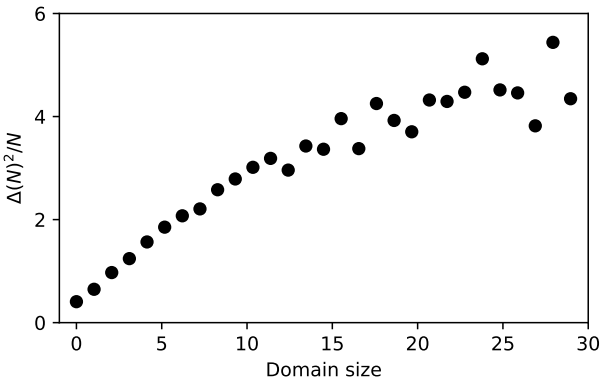

Figure 5.21: Number of atom variance as a function of domain size. Each point corresponds to the variance calculated using 100 randomly generated density profiles. The domain size corresponds to the characteristic size of the domains in the central position of the cloud (see Figure 5.20).

we used is very simplistic, the relationship between the presence of cluster in the system

[8]The density profiles are generated with the following procedure, which by no mean has a physical background, but it is capable of easily produce domains with a controlled size:

1. We create a 200×200 grid of random number uniformly distributed between 0 and 1, $N_{x,y}$. This produces a density distribution with high-frequency components in the noise which emulate the intrinsic noise of the system in absence of any spin domain.
2. We apply a Gaussian filter to the density decreasing progressively its low-pass frequency while going towards the center of the grid. This lowers the maximum spatial frequency of the noise in the central region in order to take into account that the domain formation is favored in the high-density region of the cloud, where the repulsive interactions are stronger.
3. Finally we set two numbers, a and b, to define the position of the atoms and molecules: the regions with $N_{x,y} < a$ will contain state-$|1\rangle$ atoms, the ones with $a < N_{x,y} < b$ will contain $|1-3\rangle$dimers and $N_{x,y} > b$ state-$|3\rangle$ atoms. a and b are chosen to fix the relative population between the three possible states.
4. The integrated signal is obtained but setting a value of 0 to state-$|1\rangle$ atoms, a value of 1 for state-$|3\rangle$ atoms and dimers, and finally sum along the y-axis.

and the increase of the atom number variance is very clear. In a real system, the shape and the spatial distribution of the domains could change the details of this behavior but not the overall trend. In the following, we will use the atom number fluctuation as our main observable to study the nature of the anti-correlation developing in our system after applying the interaction quench to strong repulsion. It is important to notice that, while the presence of domains implies the growth of density fluctuations, the opposite argument is not true: other effects like temperature can increase the fluctuation in the system up to the Poissonian limit $(\Delta N)^2 = N$ as already described in Section 3.3.8.

5.3.2 Atom number fluctuation after the quench

We have seen how the presence of atom number fluctuations can help us to probe the presence of spin domains in the system. We will now report the results obtained by measuring the evolution of the number variance after the quench to strong repulsion. The experimental preparation is exactly the same as the one of the pump-probe spectroscopy, except for the last part, in which the probe spectroscopy is replaced by the in-situ imaging of the state-$|3\rangle$. To recap, the procedure is the following:

1. Start with a weakly interacting $|1\rangle$-$|2\rangle$ mixture at the target magnetic field, which set the strength of the repulsive interactions after the quench, $k_F a$.

2. Quench the system into the upper branch via an RF pulse resonant with $\Delta_+(0)$. The RF power is set to the maximum allowed by the experimental apparatus in order to reduce the pulse time and increase the pump efficiency and the time resolution.

3. We acquire around 90 images of the state-$|3\rangle$ unpaired atoms and $|1-3\rangle$ dimers.

4. From the density profiles we extract the atom number variance as a function of the local mean number of atoms, $(\Delta N)^2/N$, as described in section 3.3.8.

As we discussed in Section 3.3.8, the determination of the absolute value of the atom number variance is very challenging because of the finite resolution of the imaging system. Given this difficulty we will avoid drawing conclusions based on the atom number variance alone but, instead, we will always compare results corresponding to a quench to strong repulsion $k_F a \simeq 1.4$ with the ones obtained without quench on the weakly interacting $|1\rangle$-$|2\rangle$ mixture[9]. In Figure 5.22 we report the evolution of the normalized atom number variance of the system after a quench. The holding time is represented along the y-axis of the plot, the mean atom number on the x-axis and the atom number variance normalized by the weakly interacting one by the color scale. First of all, we notice that the evolution mostly happens on the high atom number region, corresponding to the center of the trap, which is expected since the higher is the density the stronger are the local interactions. We can clearly see that, the closer we look to the center of the cloud, the faster is the dynamics of the variance: on the density wings ($N \sim 60$) $\Delta N/N$ is basically constant in time, while for $N \sim 120$ the variance quickly increase to more than twice its initial value.

[9] As shown in Figure 5.23, if we measure the variance of the weakly interacting $|1\rangle$-$|2\rangle$ mixture, the result is independent of the time of the imaging pulse. Hence, in the following, we will average the variance obtained at different times and we will use this result as a normalization for the strongly interacting cases.

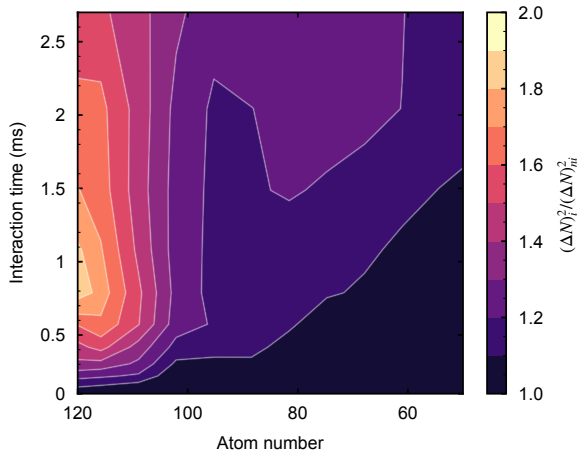

Figure 5.22: Time evolution of normalized the atom number variance as a function of the mean number of particle per bin. The vertical axis represents the holding time t, the horizontal the mean number of atoms per 5×5 bin, N (see section 3.3.8 for the details about the estimation of the variance). The left side of the plot corresponds to the central high-density region of the cloud, the right side to its low-density wings. The colors represent the evolution of the atom number variance relative to the weakly interacting case. The brighter the color, the bigger is the relative change.

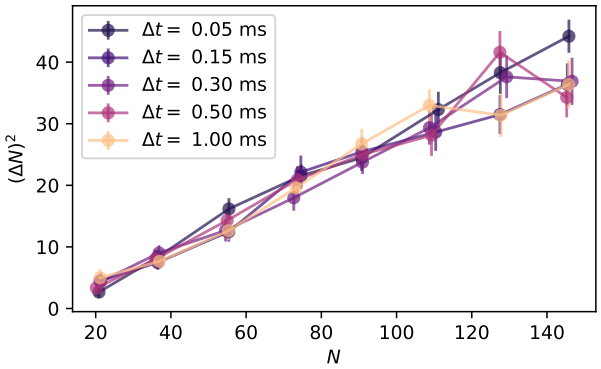

Figure 5.23: Atom number variance versus the mean atom number of a weakly interacting $|1\rangle$-$|2\rangle$ mixture. The interaction strength is so weak that we are able to detect any evolution of the system. All the measurement at different holding time, represented with different colors, are overlapped within the uncertainty of the measure. The error-bars denote the standard deviation of the mean (see section 3.3.8 for details).

High density region cut

In order to focus on the higher density region of the cloud we can select the data along the vertical direction, in the region of about 120 atoms per bin. The corresponding spatial region of the cloud is shown in Figure 5.24 and the results are plotted in Figure 5.25.

In the first millisecond of evolution time the atom number variance increases to twice

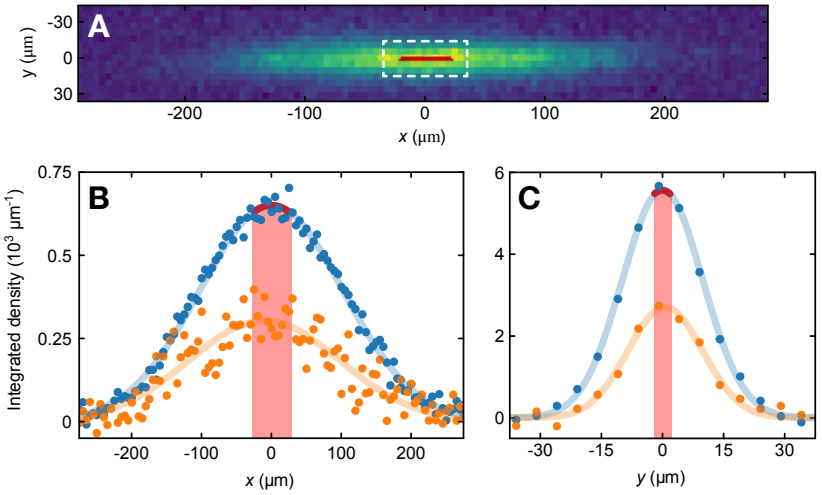

Figure 5.24: The top image shows a typical experimental density profile of the gas after the quench with a 5×5 binning, which allows us to reduce the effect of the finite resolution of the imaging system on the estimated atom number variance (see section 3.3.8 for details). The red region, $\Re$, is the one containing about 120 atoms per bin and will be the one on which we focus on this section. For comparison, the white dashed rectangle represents the region we use to extract the spectroscopy signal. The two bottom panels show the integrated density (in blue) and integrated atom number variance (in orange) along the transverse and the axial axes respectively. The red band indicates again the high-density region analyzed in this section.

its initial value, then it slowly drops. We can think of two possible ways to explain this behavior:

1. The temperature of the system increases by a factor of two due to the binding energy released during the three-body recombination. In the regime of high degeneracy the temperature is, in fact, proportional to the atom number fluctuations (see Section 3.3.8).

2. Due to strong repulsion the system develops micro-domains of atoms and molecules, whose size increases with time.

The measurement is not able to distinguish between the two scenarios but it provides at the same time an upper bound for the temperature in the system and for the maximum size of the ferromagnetic domains. Let us consider the two extreme cases in which only one of the two explanations is correct. Considering the first to be correct we find the upper bound for the temperature to be $T \simeq 0.3T_F$, which is twice its initial value. This estimation of the maximum temperature limit is in agreement with the estimation of section 5.2.8, based on the fit of the molecular density profiles.

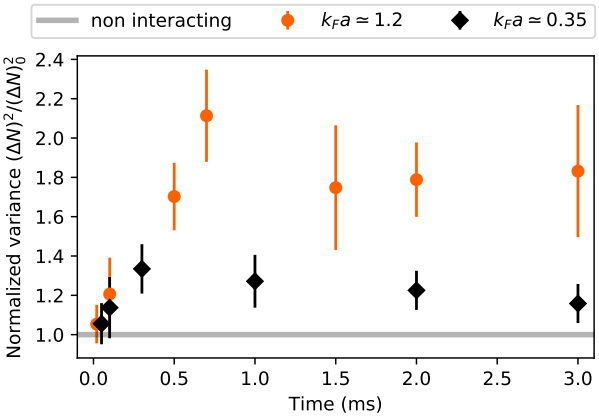

Figure 5.25: Evolution of the normalized atom number variance in the high density region of the cloud (mean number of atoms per bin between 100 and 120) for a quench to $k_Fa \simeq 1.2$ (orange dots) and to $k_Fa \simeq 0.35$ (black dots). The error-bars denote the standard deviation of the mean.

Concerning the ferromagnetic domain size, the interpretation of the result is less straightforward. While on the one hand, the factor of two would limit the domain size to a couple of inter-particle spacings, we know that after one millisecond of evolution time the number of molecules in the system overcomes the number of unpaired atoms. Hence, as illustrated in Figure 5.26, by normalizing the number variance with the mean number of atoms in the state-$|3\rangle$ we could easily underestimate its increase for the domain driven enhancement of fluctuation. It is very hard to estimate more reliable value without modeling the interplay between temperature increase, domain formation and atom-dimer interactions which, at the moment is beyond our capability. It is important to remark that this last argument does not apply to temperature since the presence of molecules, in this case, would add a contribution to the variance even bigger than the atomic one.

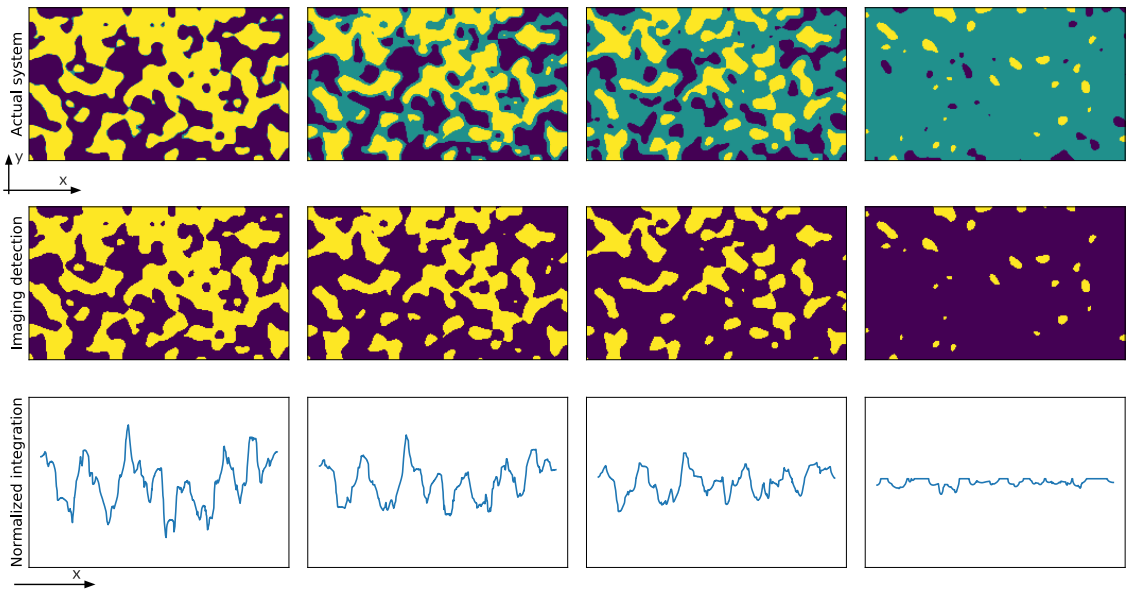

Figure 5.26: On the first row the sketch of the system in presence of domains of fixed size. The color code is the following: yellow → state-$|1\rangle$ atoms, green-blue → $|1-3\rangle$ dimers, and dark blue → state-$|3\rangle$ atoms. From left to right the relative population of dimer increases. In the second row, we plot in dark blue the atoms and molecules detected by the imaging light (resonant with state-$|3\rangle$). On the last row we plot the integration along the vertical direction of the correspondent image on the second row, counting 1 the dark blue pixels and 0 the yellow one, normalized by the mean counts. The vertical scale is the same for all the plots. One can intuitively see how the presence of molecules drastically reduces the measured variance due to ferromagnetic domains. The fluctuations are in fact given by the "holes" that the state-$|1\rangle$ domains produce in the density.

Evolution time slices

A second possible way to look at the data presented in Figure 5.22 is to compare two key evolution times: $100\,\mu$s and $700\,\mu$s. These two time slices are presented is Figure 5.27 together with the measurement of a weakly interacting gas. One can notice that the evolution after $100\,\mu$s is almost absent except for a very weak deviation in the high density region. At first glance this observation seems apparently in contrast with the energy shift measured trough pump-probe spectroscopy, which features a drop of more than 50% already at $100\,\mu$s. On the other hand, the probed quantity is not the same: while the presence of domains implies a drop in the interaction shift, the opposite is not true, since the development of anti-correlations is sufficient. The formation of spin domains could be a slower process which is the natural evolution of the initial anti-correlated state. If now we look at the atom number variance after $700\,\mu$s of evolution time we observe a two-fold increase in the center of the cloud. As already discussed it could be originated both by an increase of temperature and by the formation of magnetic domains. In both cases, the maximum increase of the variance is in fact expected in the center of the cloud, where both the repulsive interaction strength and the molecular formation rate are higher.

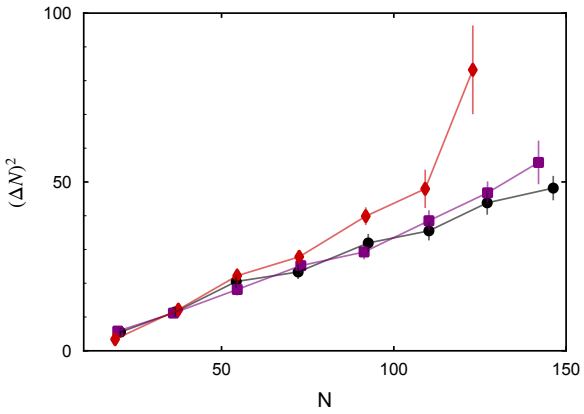

Figure 5.27: Atom number variance as a function of mean atom number. The black dataset is measured on a weakly interacting gas at the same temperature and serves as a reference. The purple data correspond to an evolution of 100 μs after the quench to $k_F a \simeq 1.2$. The red data points represent a 700 μs evolution. The relatively slow increase of the variance (as compared to the drop of energy shift measured via pump-probe spectroscopy) takes place mostly in the high-density region of the cloud and suggests the development of micro-domains in the system.

5.3.3 Density-density correlations

In the previous section we studied the development of the density fluctuations in the system after the quench to strong repulsive interactions. In order to further investigate spatial properties of these fluctuations we also calculate the density-density correlation function, a non local observable, which quantifies the probability of finding two particles in the same hyperfine spin state at a given distance R. We will see that, although this observable is extremely limited by the resolution of our imaging system, it will provide valuable information about the maximum size of the spin domains eventually present in the system.
The spatial correlation function of the density fluctuations is given by:

$$C(\mathbf{r}, \mathbf{r}+\mathbf{R}) = \langle (N_{\mathbf{r}} - \langle N_{\mathbf{r}} \rangle)(N_{\mathbf{r}+\mathbf{R}} - \langle N_{\mathbf{r}+\mathbf{R}} \rangle) \rangle = \langle N_{\mathbf{r}}\, N_{\mathbf{r}+\mathbf{R}} \rangle - \langle N_{\mathbf{r}} \rangle \langle N_{\mathbf{r}+\mathbf{R}} \rangle \,, \quad (5.16)$$

where $N_{\mathbf{r}}$ is the number of atoms contained in the column (super-) pixel with coordinates $\mathbf{r} = (i, j)$, $\mathbf{R}$ is the distance vector expressed in (super-) pixel units, and the angular brackets represent averaging over a set of images consisting of $\mathcal{N} \approx 80$ experimental realizations. Notice that the zero-distance correlation function $C(\mathbf{r}, \mathbf{r})$ corresponds to the atom number fluctuations $(\Delta N)^2_{\mathbf{r}}$ of the content of a column (super-) pixel, whose determination was discussed in the previous Section. In order to obtain $C(R)$, we first perform an azimuthal averaging of $C(\mathbf{r}, \mathbf{r}+\mathbf{R})$:

$$C(\mathbf{r}, R) = \frac{1}{N_R} \sum_{|\mathbf{R}|=R} C(\mathbf{r}, \mathbf{r}+\mathbf{R}) \,, \quad (5.17)$$

where N_R is the number of (super-) pixels at distance R. By averaging over all (super-) pixels within the central region $\Re$ of the atomic cloud (defined in figure 5.24), we obtain $C(R)$, i.e. the auto-correlation function and the azimuthally averaged auto-correlation

function of density fluctuations. An example of the $C(\mathbf{R})$ for a weakly interacting gas is shown in Figure 5.28. As for the determination of the atom number variance, the

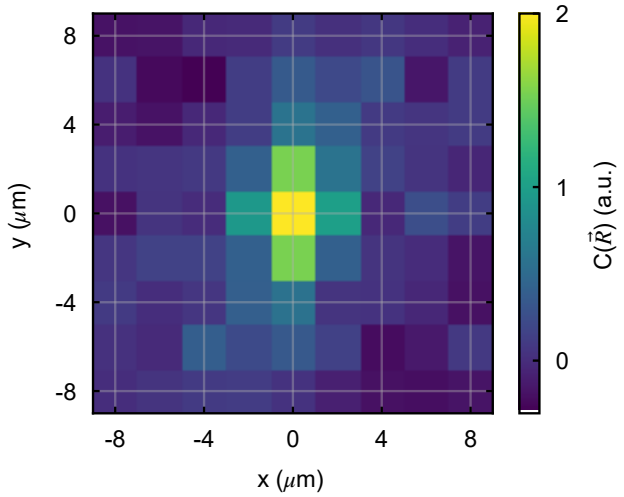

Figure 5.28: Spatial noise correlations $C(\mathbf{R})$ for a non-interacting degenerate Fermi gas, with a binning size of 2 px. The finite optical resolution results in the blurring of the variance, i.e. the zero-range noise correlator, to finite distance R, yielding non-zero spatial correlations over a distance associated with the width the imaging point-spread function.

choice of the bin size, i.e. the super-pixel area, plays an important role. While for too small binning size the atomic variance is completely washed out by the resolution blurring as described in section 3.3.8, having bigger bins implies an intrinsic drop of the spatial resolution, consequently in the detection of spatial feature in the correlation. The best compromise we found is a binning of 2 pixels, which provides a small but sufficient signal from the atomic fluctuations and, at the same time, allows to probe the presence of spin domains with a size of the order of 2 μm. Following this analysis procedure, we calculate the density-density correlation function of the system after the quench, using the same dataset presented in Figure 5.22. Since the finite resolution of the imaging system has a positive contribution to the correlation function, we normalize our data subtracting from the correlator measured after the quench to strong repulsion, $C_{1.2}(R)$ (corresponding to $k_F a \simeq 1.2$), the one obtained by probing a very weakly repulsive gas $C_{0.3}(R)$ (corresponding to $k_F a \simeq 0.3$). The result is plotted in Figure 5.29. First of all, one can notice that $C(R = 0, t)$ corresponds to the evolution of the variance presented in Figure 5.25, but this time, since the super-pixel are is smaller, the amplitude of the signal is drastically reduced. Nevertheless, one can notice the growth of spatial correlations within a range of about 2 μm, which is compatible with the increase of the atom number variance measured in the previous section. Moreover, at 1 ms of evolution time we find a slightly negative signal, which is again compatible with the presence of spin micro-domains with a size of 2 μm. However, it is really important to keep in mind that these two observations are at the very edge of our experimental resolution and comes with an extremely low signal. They are therefore too weak to claim the presence of ferromagnetic domains in the system but, on the other hand, they can be valuable to define an upper limit of about 2 μm for their possible size. In conclusion, with the current experimental setup, we do not have enough spatial resolution to resolve the presence of spin micro-domains but, in the future, upgrading of

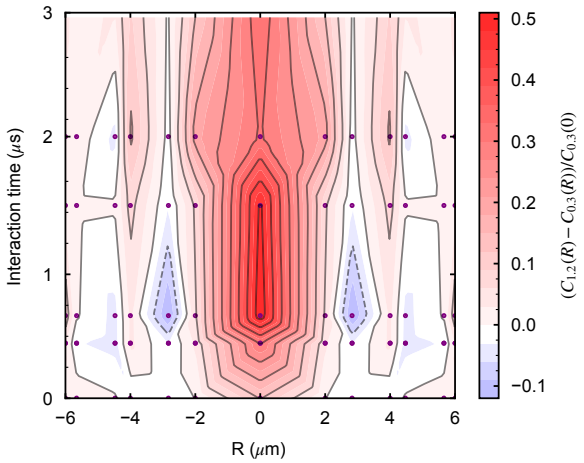

Figure 5.29: Density-density correlation function averaged in the central region of the atomic cloud $\Re$ as a function of the evolution time after the quench. The correlation function is calculated using a bin size of 2×2.

our imaging system with a sub-micrometer resolution microscope, the methods described in this section can be used to finally reveal or completely reject their presence.

5.4 More spectroscopic observables

In the previous section we showed how the two-component Fermi gas evolves after a quench to strong repulsion by quickly developing anti-correlations and, at the same time decay into the lower branch of the many-body system by molecular formation. Furthermore we studied the long time behavior of the system, during which, anti-correlations are preserved producing a meta-stable glassy state, in which magnetic atomic and molecular micro-domains survive for more then 30 ms. Hereafter, we will discuss about a set of additional measurements we performed to further understand the state of the system after the quench and the interplay between the pairing and the ferromagnetic instabilities.

5.4.1 Time evolution of the $|1\rangle$-$|2\rangle$-$|3\rangle$ mixture

Among the various characterization of the emulsion state, we have also investigated the spectral response of the system if the optical blast that follows the RF pump pulse is not applied. In this case, the quenched gas comprises three different atomic states. In general, the presence of three distinguishable fermionic states has detrimental effects on the stability of the trapped gas, limiting the lifetime of the overall population in the trap through three-body inelastic decay processes towards deeply-bound molecular states [112, 113]. On the other hand, we checked that a small state-$|2\rangle$ population not exceeding 30% of that of state-$|3\rangle$, does not cause substantially enhanced losses within the first 2 ms of evolution. As such, state-$|2\rangle$ fermions can be considered as weakly-interacting spectators of the correlated many-body dynamics in the $|1\rangle$-$|3\rangle$ mixture and the emergent anti-correlated phase.
In Figure 5.30 we show the probe spectroscopy signal, $N_2/(N_2+N_3)$, up to 1 ms of evolution time. On the left panel, we plot the signal obtained probing the central region of the cloud,

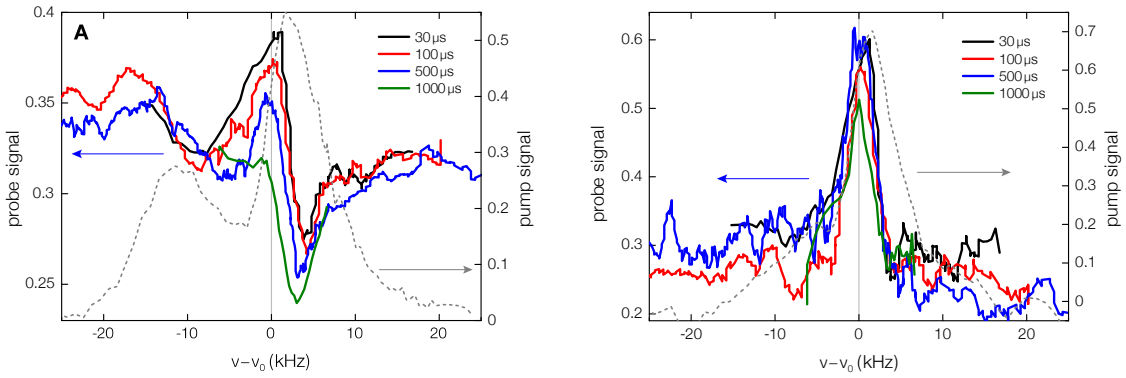

Figure 5.30: Spectral response of a quenched three-component $|1\rangle$-$|2\rangle$-$|3\rangle$ gas at various evolution times for $\kappa_F(0)\,a \sim 1.7$ (see text), for the central region (**A**) and the outermost region of the trapped sample (**B**). In both panels, the pump spectra are shown as a reference (gray dashed lines, right y-axis), and the different colors correspond to the different evolution times indicated in the legend. While state-$|3\rangle$ atoms evolve into the emulsion phase within the central region, leading to $\Delta_+(t) \to 0$, state-$|2\rangle$ atoms remain mixed at all times with all other particles (state-$|1\rangle$ and $|3\rangle$ fermions, and 1-3 molecules, respectively). As such, the spectral response of state-$|2\rangle$ atoms starkly differs from that of state-$|3\rangle$ surviving fermions, simultaneously probed with the near-resonant 2-3 RF frequency pulse. This leads, within the denser part of the sample, to a double-peak structure at positive detuning: the negative peak refers to state-$|2\rangle$ atoms being transferred in the $|3\rangle$-state. The positive peak near zero detuning corresponds instead to state-$|3\rangle$ atoms transferred back from the emulsion phase. The double feature is absent in the paramagnetic wings of the distribution where both state-$|3\rangle$ and $|2\rangle$ atoms are always mixed with the surrounding medium.

on the right panel the one extracted from the wings. One can immediately realize that a new peak, with negative amplitude, appears for positive detunings. In a $|1\rangle$-$|2\rangle$-$|3\rangle$ mixture the probe spectroscopy pulse does not only flip atoms from state-$|3\rangle$ to state-$|2\rangle$, but also the opposite. In order to understand the peak structure one needs to consider all the possible transitions between the two-state as sketched in Figure 5.31. Since the $|2\rangle$ atoms are weakly interacting with the other two states, they will uniformly occupy all the atomic cloud and act as a background. We can therefore recognize three different configurations of atoms and molecules which will produce a different spectroscopy signal (corresponding to the three panel of Figure 5.31):

1. The configuration with a majority of state-$|3\rangle$ atoms in the anti-correlated or micro-domain phase together with a lower density of state-$|2\rangle$ atoms. The regions of the cloud corresponding to this configuration will resonate with an RF frequency close to the $|2\rangle$-$|3\rangle$ bare transition and produce a positive spectroscopy signal.

2. The configuration comprising $|1-3\rangle$ dimers and residual state-$|2\rangle$ atoms. In this case, the RF pulse can drive two possible transitions. The first one corresponds to the dissociation of the molecule and producing state-$|1\rangle$ and state-$|2\rangle$ free atoms. The peak is at negative detuning, corresponding to the binding energy of the molecule, and with a positive sign. The second possibility is the transfer of the free state-$|2\rangle$ atoms into state-$|3\rangle$. Since the final state is repulsively interacting, the spectroscopy peak will have a positive detuning. The spectroscopy this time signal will be negative since the number of state-$|2\rangle$ particle decreases.

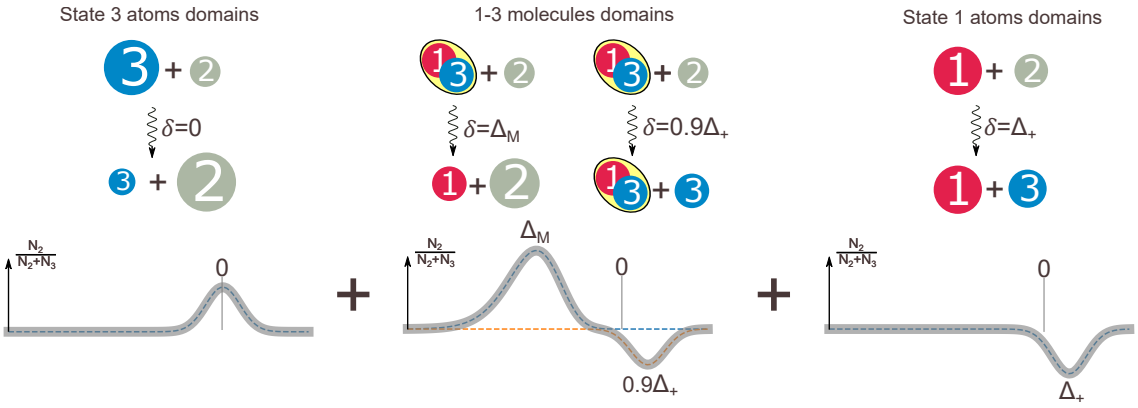

Figure 5.31: Sketch of the three possible local configurations of the $|1\rangle$-$|2\rangle$-$|3\rangle$ mixture after the $|1\rangle - |3\rangle$ anti-correlations are formed and the corresponding spectroscopy signals when the RF pulse frequency is scanned near the $|2\rangle$-$|3\rangle$ transition. **The left(right) panel** corresponds the region containing state-$|3\rangle(|1\rangle)$ atoms in the anti-correlated of micro-domain phase. **The middle panel** corresponds to regions containing $|1-3\rangle$ dimers. Since the state-$|2\rangle$ atoms are weakly interacting with the rest of the system, they are homogeneously distributed in all the regions of the cloud.

3. The configuration consisting in state-$|1\rangle$ in the anti-correlated or microdomain phase, and residual state-$|2\rangle$ atoms. In this case, the RF pulse will drive the weakly interacting $|1\rangle$-$|2\rangle$ mixture to the strongly interacting $|1\rangle$-$|3\rangle$. This is the exact analogy of the pump pulse, the detuning is positive and the sign of the spectroscopy peak negative.

In Figure 5.30 one can observe how the evolution in time of the system affects these three different signals. The positive peak corresponding to the first configuration shifts towards zero detuning because of the growth of anti-correlations and decreases in time due to the molecular formation. On the other hand, the negative peak due to the combined contributions of the second and third configuration increases its amplitude because of the increase of $|1\rangle$-$|3\rangle$ dimers. Moreover, its detuning converges in time to the value measured through pump spectroscopy (gray dashed line). On the right panel of Figure 5.30 one can see that the signal extracted from the low-density wings of the cloud is completely different. There the interaction strength is not sufficient to build the anti-correlated state and the density low for efficient three-body recombination. Hence, we expect a $|1\rangle$-$|2\rangle$-$|3\rangle$ mixture with a relatively smaller number of state-$|2\rangle$ atoms. The spectroscopy signal is almost constant in time with a small detuning corresponding to the weak interaction strength. This observation confirms the hypothesis that the quenched gas evolves in time to produce an anti-correlated state, in which the wave-function overlap between state-$|1\rangle$ and state-$|3\rangle$ atoms drops because of the strong repulsion. The presence of three distinguishable features in the spectroscopy signal is in fact hard to explain if the density of the three component gas was homogeneous.

5.4.2 Spatial dependence of $\Delta_+(t)$

In order to better understand the spatial distribution of the anti-correlated phase within our inhomogeneous trapped sample, it is instructive to analyze the behavior of the spectral response of a $|1\rangle - |3\rangle$ gas mixture as a function of evolution time and distance $\tilde{R}$ from the

trap center for $k_F a \simeq 1.2$. The result plotted in Figure 5.32, shows an RF shift Δ_+ initially

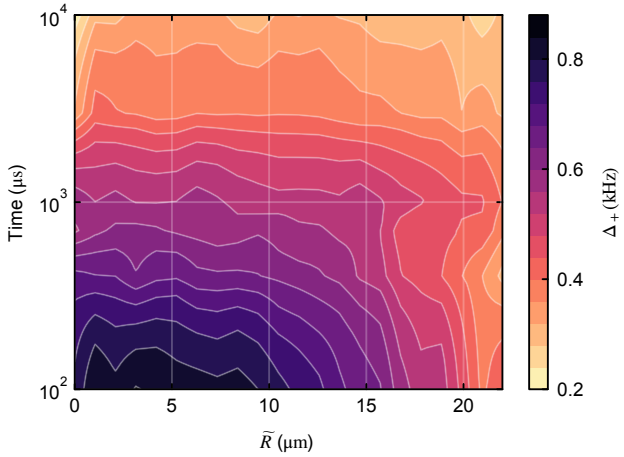

Figure 5.32: Evolution of the energy shift as a function of the distance from the center of the cloud. The shorter is this distance, the higher is the gradient of the energy shift, i.e. the rate of anti-correlations development. In the outer, low-density region of the cloud, the relative drop is almost negligible and we ascribe is to the decreasing of the unpaired atom density and heating in the system. Since the cloud is cigar-shaped, in order to azimuthally average the shift we perform a rescale of the long axis to match the shortest one. Hence, $\tilde{R}$ refers to the distance measured along the transverse direction of the cloud.

much bigger in the center than in the external regions of the cloud, owing to the higher density and therefore the higher interaction strength. However, as the system evolves $\Delta_+(t)$ within high-density central region quickly drops to values as low as 200 Hz, signaling the development of anti-correlations. In contrast, the outer wings of the sample present a much slower and less pronounced evolution of the interaction shift, consistent with a pure drop of the atom density and raise of the temperature. The intermediate regions, $10 \leq \tilde{R} \leq 20\,\mu$m, present a trend smoothly crossing-over between these two limiting behaviors.
This observation confirms the findings of the previous sections, offering a new possibility to measure the evolution of the system at different interaction parameters within the same experimental run. In the framework of the local density approximation (LDA), one can consider independently different density region of the atomic cloud. The center of the trap, where the density is higher, corresponds to the highest $k_F a$ and the wings of the density distribution to a weakly interacting gas.
In order to improve this analysis one could use the inverse Abel transformation to map the integrated signal presented in Figure 5.32 to three dimension and find the local energy shift $\Delta_+(x, y, z)$ as a function of the local density $n(x, y, z)$, which correspond to the local interaction parameter $k_F(x, y, z)a$. In practice, we could not carry out this procedure because of the insufficient signal to noise ratio to extract convincing results from the Abel deconvolution.

5.4.3 Spectroscopic probing with long RF pulses

To better understand the spectral features of the repulsive atomic peak in the anti-correlated regime, we sacrificed our time resolution using 2 ms long probe pulses in order to significantly reduce its Fourier width. As shown in Figure 5.33, with the increased

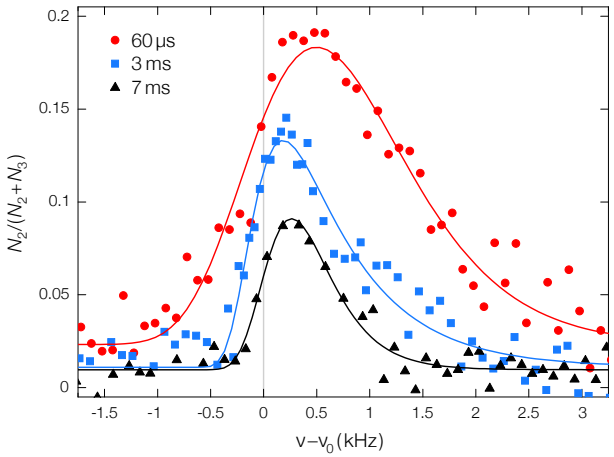

Figure 5.33: Spectral response of a gas evolving at $k_F a \simeq 1.3$ into the anti-correlated phase, recorded with a 2 ms-long probe pulse after different evolution times (see legend). The increased duration of the spectroscopy pulse significantly enhances our spectral sensitivity and it allows to trace the asymmetric decay of the spectral weight associated with different frequency detunings. In particular, the blue-detuned parts of the spectrum decay much more rapidly than the one around zero (or slightly positive). The solid lines are obtained by fitting the data with a Gumbel function.

spectral resolution, the line profiles result strongly asymmetric, being dominated by the inhomogeneity of the trapped system. In particular, one can notice the different timescales associated to the decay of the different contribution to the overall spectral response: while the signal at large and positive detuning is strongly reduced already after few milliseconds of evolution, the drop of the signal around zero detuning is much slower. Such a strong asymmetry, revealed within the central trap region, becomes much less pronounced by considering the outer low-density region of the cloud, as well as by considering lower interaction strengths for which the system remains paramagnetic.

5.4.4 Metastability of the anti-correlated state

Let me discuss about the last measurement described in this thesis. Its main purpose is to test the stability of the anti-correlated state by increasing the repulsive interaction strength once the anti-correlated state is already formed. The idea comes from the following observation: if we let the system evolve for a very long time after the quench to strong repulsion, up to 100 ms, and we measure the surviving unpaired population, we notice that it is bigger for higher interaction strengths. As shown in Figure 5.34 if we compare the evolution of the unpaired fermionic population when we quench the interactions to $k_F a \simeq 2.3$ with respect to $k_F a \simeq 0.9$ we notice that, even if the time zero population is smaller because of the lower efficiency of the pump RF pulse, its value around 100 ms is higher.
Why does the unpaired atomic population relative to different interaction parameter cross at a given evolution time even though the molecular formation rate should be higher, higher is the interaction strength? One simple explanation could be that after such a long time the system becomes a thermal mixture of hot molecules and atoms, with a population ratio set by the chemical equilibrium [114, 5]: since at higher interaction strength the binding energy of the molecules is lower, the energy difference between the upper and lower branch

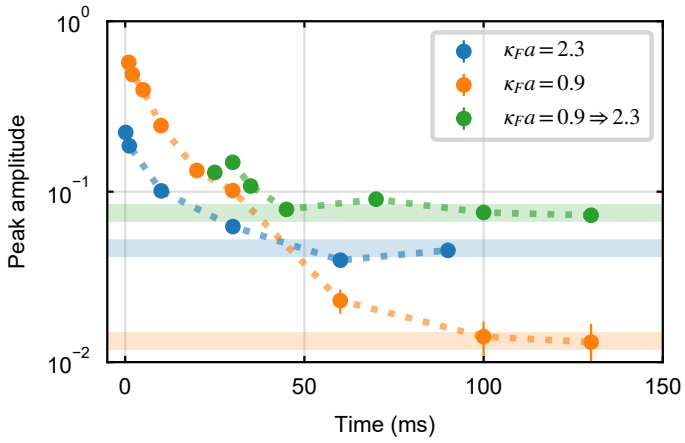

Figure 5.34: Time evolution of the repulsive atomic peak. The orange and blue data set correspond to the standard pump-probe spectroscopy described at the beginning of this section, with a quench to $k_F a \simeq 0.9$ and $k_F a \simeq 2.3$ respectively. While at short time the unpaired population is higher for the lower interaction strength, due to higher pump efficiency and slower pairing rate (see Figure 5.8), after 50 ms of evolution we find an opposite trend. The idea is that once the anti-correlations in the system are developed, the stronger is the repulsion, the slower is their melting, increasing their lifetime. Furthermore, this is confirmed by a second experimental sequence, of which the results are plotted in green: the system is quenched at $k_F a \simeq 0.9$, then, after a waiting time of 1 ms during which the anti-correlations are established, the interaction strength is adiabatically rumped up to $k_F a \simeq 2.3$. Therefore, the already developed anti-correlations are reinforced preventing further formation of dimers and, as one can see, the unpaired atomic population remains almost frozen. The error-bars correspond to the fitting uncertainty on the amplitude of the atomic peak fit.

is also reduced. Therefore, the ratio between atomic and molecular population, set by the Boltzmann distribution, would be higher. A second possibility is that, when the anti-correlated state is formed, the wavefunction overlap between the atoms in the state $|1\rangle$ and in the state $|3\rangle$ is drastically reduced, effectively suppressing the three-body recombination mechanism.
In order to discriminate between these two hypotheses we perform the following experiment, which consists of four main steps:

1. We quench the system to $k_F a \simeq 0.9$
2. We wait for the energy shift to drop (1 ms).
3. We ramp up the Feshbach magnetic field to increase the interaction parameter up to $k_F a \simeq 2.3$ in about 20 ms.
4. We probe the unpaired fermionic population up to 100 ms of evolution time in the strong repulsive regime.

The result is reported in green in Figure 5.34. As we can see, this procedure leads to the highest ratio between unpaired atoms and molecules at a long evolution time. In order to give an interpretation of the result, it is useful to first look again at the evolution of the peak

amplitude after the quench without any magnetic field ramp. For lower interaction strength (orange data) the initial amplitude is higher than the higher interacting one (blue data) because of the greater pump efficiency and the lower pairing rate, as already presented in Figure 5.8. After about 30 ms we observe the opposite trend: the peak amplitude becomes bigger for higher interaction strength. As already observed in our previous work [115], the stability of the anti-correlated state is higher when supported by stronger repulsive interactions, which prevent its melting. Our interpretation of the physics taking place during the four steps is the following:

1. Quench to $k_F a \simeq 0.9 \rightarrow$ the system is pumped into the upper branch at a moderate interaction parameter, allowing for good transfer efficiency.

2. Wait for 1 ms $\rightarrow$ during the waiting time the anti-correlated state has formed. Being at $k_F a \simeq 0.9$ the pairing rate relatively low, not many molecules are formed in the process.

3. Ramp up the interactions to $k_F a \simeq 2.3 \rightarrow$ by increasing the interaction parameter one can naively think to increase the pairing rate. While this is clearly true for a homogeneous gas, it does not apply in the same way to a system which contains anti-correlations. The observed effect is the opposite: strengthening up the repulsive interactions, the anti-correlations become stronger, lasting for a longer time and effectively preventing further molecular formation.

4. Probe the unpaired fermionic population $\rightarrow$ probing the system after the quench followed by the increase of the interaction parameter correspond to measure a significantly high number of unpaired atoms even after 100 ms of evolution time.

In the end, this experimental sequence is a good strategy to increase the atomic population at long evolution time. It takes advantages both from the lower pairing rate at $k_F a \simeq 0.9$ and from the strong repulsion at $k_F a \simeq 2.3$.
In conclusion, this measurement rules out the hypothesis that the state of the system after a long evolution time is a hot mixture of atoms and molecules in thermal equilibrium. Instead, it seems that the atom-atom and the atom-dimer anti-correlations survive in a metastable glassy state [116, 117] or quantum emulsion [118], in which the overlap of the atomic and the molecular wave-functions at short distances, even down to a single particle spacing, is reduced.

Chapter 6

Conclusions

In this thesis, I present the study of the many-body dynamics of ultracold repulsive Fermi gases of ^{6}Li atoms. I performed two paradigmatic experiments which study the upper branch of the repulsive Fermi gas up to very strong coupling, both in a very unbalanced mixture and in the balanced case.
In the first experiment, I characterized this branch in the impurity limit, within the quasi-particle framework, through radio-frequency spectroscopy. This study is extremely valuable as a meeting point between theories and experiments and stands as an ideal cross-validation tool. I experimentally measured the property of the repulsive Fermi polaron such as its energy, effective mass, quasi-particle residue and lifetime, and compared the results with different theoretical methods highlighting their weaknesses and strengths in different interactions regimes. The main result of this first investigation is that for strong enough repulsive interactions, the energy of the repulsive polaron exceeds the Fermi energy of the system, which is a clear signature of the presence of a ferromagnetic instability in the repulsive branch.
In the second experiment, I have explored the out-of-equilibrium dynamics of a Fermi gas quenched to strong repulsion exploiting a pump-probe RF spectroscopy scheme. I found that within the first few Fermi times, contrary to previous studies, the pairing processes does not dominate the evolution of the system but instead competes with the growth of anti-correlations, which results even faster at strong coupling regime. Moreover, I showed how the interplay between these two mechanisms gives rise to a long-lived emulsion state of atoms and dimers in which the inter-atomic anti-correlations survive for thousands of Fermi times and prevent the system to completely decay into the molecular ground-state.
In the future I plan to exploit the experimental techniques learned and developed within the framework of this thesis to further study the out-of-equilibrium physics of Fermi gases such as the effect of repulsive impurities in a superfluid bath of pairs [119, 120]. Moreover, I aim to study the effect of different trapping geometries achieved by using a Digital Mirror Device, capable of generating almost arbitrary light potential. Finally, I want to explore the physics of the repulsive gas in lower dimensionality by confining the fermionic cloud in a quasi-2D regime [121, 122, 123]. Together with the implementation of a high-resolution microscope with a sub-micrometer resolution I plan to study again the development of spin anti-correlations in the system directly by probing the density distribution and confirming or excluding once for all the growth of ferromagnetic domains in the repulsive gas.

Bibliography

[1] Edmund C Stoner. Lxxx. atomic moments in ferromagnetic metals and alloys with non-ferromagnetic elements. *The London, Edinburgh, and Dublin Philosophical Magazine and Journal of Science*, 15(101):1018–1034, 1933.

[2] Dieter Vollhardt, N Blümer, K Held, and M Kollar. Metallic ferromagnetism - an electronic correlation phenomenon. In *Band-Ferromagnetism*, pages 191–207. Springer, 2001.

[3] M Brando, D Belitz, FM Grosche, and TR Kirkpatrick. Publisher's note: Metallic quantum ferromagnets [rev. mod. phys. 88, 25006 (2016)]. *Reviews of Modern Physics*, 88(3):039901, 2016.

[4] Gyu-Boong Jo, Ye-Ryoung Lee, Jae-Hoon Choi, Caleb A Christensen, Tony H Kim, Joseph H Thywissen, David E Pritchard, and Wolfgang Ketterle. Itinerant ferromagnetism in a fermi gas of ultracold atoms. *Science*, 325(5947):1521–1524, 2009.

[5] Christian Sanner, Edward J Su, Wujie Huang, Aviv Keshet, Jonathon Gillen, and Wolfgang Ketterle. Correlations and pair formation in a repulsively interacting fermi gas. *Physical review letters*, 108(24):240404, 2012.

[6] Cheng Chin, Rudolf Grimm, Paul Julienne, and Eite Tiesinga. Feshbach resonances in ultracold gases. *Reviews of Modern Physics*, 82(2):1225, 2010.

[7] Lev Davidovich Landau and Evgenii Mikhailovich Lifshitz. *Course of theoretical physics*. Elsevier, 2013.

[8] Vijay B Shenoy and Tin-Lun Ho. Nature and properties of a repulsive fermi gas in the upper branch of the energy spectrum. *Physical review letters*, 107(21):210401, 2011.

[9] M. Jag A. Trenkwalder P. Massignan G.M. Bruun F. Schreck C. Kohstall, M. Zaccanti and R. Grimm. Metastability and coherence of repulsive polarons in a strongly interacting fermi mixture. *Nature*, 485:615, 2012.

[10] Pietro Massignan, Matteo Zaccanti, and Georg M Bruun. Polarons, dressed molecules and itinerant ferromagnetism in ultracold fermi gases. *Reports on Progress in Physics*, 77(3):034401, 2014.

[11] David Pekker, Mehrtash Babadi, Rajdeep Sensarma, Nikolaj Zinner, Lode Pollet, Martin W Zwierlein, and Eugene Demler. Competition between pairing and ferromagnetic instabilities in ultracold fermi gases near feshbach resonances. *Physical review letters*, 106(5):050402, 2011.

[12] Joseph Orenstein. Quantum materials. *Physics Today*, 65(9):44, 2012.

[13] Claudio Giannetti, Massimo Capone, Daniele Fausti, Michele Fabrizio, Fulvio Parmigiani, and Dragan Mihailovic. Ultrafast optical spectroscopy of strongly correlated materials and high-temperature superconductors: a non-equilibrium approach. *Advances in Physics*, 65(2):58–238, 2016.

[14] LD Landau and SI Pekar. Effective mass of a polaron. *J. Exp. Theor. Phys*, 18:419–423, 1948.

[15] LD Landau. The theory of a fermi liquid. *Soviet Physics Jetp-Ussr*, 3(6):920–925, 1957.

[16] Herbert Fröhlich, Hans Pelzer, and Sigurd Zienau. Xx. properties of slow electrons in polar materials. *The London, Edinburgh, and Dublin Philosophical Magazine and Journal of Science*, 41(314):221–242, 1950.

[17] Herbert Fröhlich. Electrons in lattice fields. *Advances in Physics*, 3(11):325–361, 1954.

[18] Richard Phillips Feynman. Slow electrons in a polar crystal. *Physical Review*, 97(3):660, 1955.

[19] F Scazza, G Valtolina, P Massignan, Alessio Recati, A Amico, A Burchianti, C Fort, M Inguscio, M Zaccanti, and G Roati. Repulsive fermi polarons in a resonant mixture of ultracold li 6 atoms. *Physical review letters*, 118(8):083602, 2017.

[20] A Amico, F Scazza, G Valtolina, PES Tavares, W Ketterle, M Inguscio, G Roati, and M Zaccanti. Time-resolved observation of competing attractive and repulsive short-range correlations in strongly interacting fermi gases. *arXiv preprint arXiv:1807.10208*, 2018.

[21] Kerson Huang. *Introduction to statistical physics*. Chapman and Hall/CRC, 2009.

[22] Sylvain Nascimbène, Nir Navon, KJ Jiang, Frédéric Chevy, and Christophe Salomon. Exploring the thermodynamics of a universal fermi gas. *Nature*, 463(7284):1057, 2010.

[23] Munekazu Horikoshi, Shuta Nakajima, Masahito Ueda, and Takashi Mukaiyama. Measurement of universal thermodynamic functions for a unitary fermi gas. *Science*, 327(5964):442–445, 2010.

[24] Mark JH Ku, Ariel T Sommer, Lawrence W Cheuk, and Martin W Zwierlein. Revealing the superfluid lambda transition in the universal thermodynamics of a unitary fermi gas. *Science*, 335(6068):563–567, 2012.

[25] Stefano Giorgini, Lev P Pitaevskii, and Sandro Stringari. Theory of ultracold atomic fermi gases. *Reviews of Modern Physics*, 80(4):1215, 2008.

[26] ShangâKeng Ma. *Statistical Mechanics*. World Scientific, 1985.

[27] T Rom, Th Best, D Van Oosten, U Schneider, S Fölling, B Paredes, and I Bloch. Free fermion antibunching in a degenerate atomic fermi gas released from an optical lattice. *Nature*, 444(7120):733, 2006.

[28] Ehud Altman, Eugene Demler, and Mikhail D Lukin. Probing many-body states of ultracold atoms via noise correlations. *Physical Review A*, 70(1):013603, 2004.

[29] Torben Müller, Bruno Zimmermann, Jakob Meineke, Jean-Philippe Brantut, Tilman Esslinger, and Henning Moritz. Local observation of antibunching in a trapped fermi gas. *Physical review letters*, 105(4):040401, 2010.

[30] Amir Itah, Hagar Veksler, Oren Lahav, Alex Blumkin, Coral Moreno, Carmit Gordon, and Jeff Steinhauer. Direct observation of a sub-poissonian number distribution of atoms in an optical lattice. *Physical review letters*, 104(11):113001, 2010.

[31] Jakob Meineke, Jean-Philippe Brantut, David Stadler, Torben Müller, Henning Moritz, and Tilman Esslinger. Interferometric measurement of local spin fluctuations in a quantum gas. *Nature Physics*, 8(6):454, 2012.

[32] Rep Kubo. The fluctuation-dissipation theorem. *Reports on progress in physics*, 29(1):255, 1966.

[33] Yvan Castin. Basic theory tools for degenerate fermi gases. *arXiv preprint cond-mat/0612613*, 2006.

[34] GE Astrakharchik, R Combescot, and LP Pitaevskii. Fluctuations of the number of particles within a given volume in cold quantum gases. *Physical Review A*, 76(6):063616, 2007.

[35] Jan Jakob Meineke. *Fluctuations and correlations in ultracold Fermi gases*. ETH Zurich, 2012.

[36] Herman Feshbach. A unified theory of nuclear reactions. ii. *Annals of Physics*, 19(2):287–313, 1962.

[37] S Inouye, MR Andrews, J Stenger, H-J Miesner, DM Stamper-Kurn, and W Ketterle. Observation of feshbach resonances in a bose–einstein condensate. *Nature*, 392(6672):151, 1998.

[38] Bernard A Lippmann and Julian Schwinger. Variational principles for scattering processes. i. *Physical Review*, 79(3):469, 1950.

[39] Jun John Sakurai and Eugene D Commins. Modern quantum mechanics, revised edition, 1995.

[40] Ch J Joachain. Quantum collision theory (north-holland, amsterdam, 1975). *Eq.(11.296)*.

[41] Claude Cohen-Tannoudji and David Guéry-Odelin. *Advances in atomic physics: an overview*. World Scientific, 2011.

[42] Leonard I Schiff. Quantum mechanics, international series in pure and applied physics, 1968.

[43] Wilhelm Zwerger. *The BCS-BEC crossover and the unitary Fermi gas*, volume 836. Springer Science & Business Media, 2011.

[44] Gerhard Zürn, Thomas Lompe, Andre Niklas Wenz, Selim Jochim, PS Julienne, and JM Hutson. Precise characterization of li 6 feshbach resonances using trap-sideband-resolved rf spectroscopy of weakly bound molecules. *Physical review letters*, 110(13):135301, 2013.

[45] Yvan Castin and Félix Werner. The unitary gas and its symmetry properties. In *The BCS-BEC Crossover and the Unitary Fermi Gas*, pages 127–191. Springer, 2012.

[46] Ludovic Pricoupenko and Yvan Castin. One particle in a box: The simplest model for a fermi gas in the unitary limit. *Physical Review A*, 69(5):051601, 2004.

[47] DS Petrov, Christophe Salomon, and Gora V Shlyapnikov. Weakly bound dimers of fermionic atoms. *Physical Review Letters*, 93(9):090404, 2004.

[48] Ao J Leggett. Diatomic molecules and cooper pairs. In *Modern trends in the theory of condensed matter*, pages 13–27. Springer, 1980.

[49] Ultra-cold Fermi Gases. M. inguscio, w. ketterle, and c. salomon. *Proceedings of the International School of Physics Enrico Fermi, Course CLXIV, Varenna, 20-30 June 2006*, 2008.

[50] Eric Braaten. Universal relations for fermions with large scattering length. In *The BCS-BEC Crossover and the Unitary Fermi Gas*, pages 193–231. Springer, 2012.

[51] RA Duine and AH MacDonald. Itinerant ferromagnetism in an ultracold atom fermi gas. *Physical review letters*, 95(23):230403, 2005.

[52] Hui Zhai. Correlated versus ferromagnetic state in repulsively interacting two-component fermi gases. *Physical Review A*, 80(5):051605, 2009.

[53] GJ Conduit and BD Simons. Repulsive atomic gas in a harmonic trap on the border of itinerant ferromagnetism. *Physical review letters*, 103(20):200403, 2009.

[54] LJ LeBlanc, JH Thywissen, AA Burkov, and A Paramekanti. Repulsive fermi gas in a harmonic trap: Ferromagnetism and spin textures. *Physical Review A*, 80(1):013607, 2009.

[55] Ilya Berdnikov, Piers Coleman, and Steven H Simon. Itinerant ferromagnetism in an atom trap. *Physical Review B*, 79(22):224403, 2009.

[56] Xiaoling Cui and Hui Zhai. Stability of a fully magnetized ferromagnetic state in repulsively interacting ultracold fermi gases. *Physical Review A*, 81(4):041602, 2010.

[57] Shizhong Zhang, Hsiang-hsuan Hung, and Congjun Wu. Proposed realization of itinerant ferromagnetism in optical lattices. *Physical Review A*, 82(5):053618, 2010.

[58] Henning Heiselberg. Itinerant ferromagnetism in ultracold fermi gases. *Physical Review A*, 83(5):053635, 2011.

[59] S Pilati, G Bertaina, S Giorgini, and M Troyer. Itinerant ferromagnetism of a repulsive atomic fermi gas: A quantum monte carlo study. *Physical review letters*, 105(3):030405, 2010.

[60] Lev Davidovich Landau and EM Lifshitz. *Course of Theoretical Physics Vol 3 Quantum Mechanics*. Pergamon Press, 1958.

[61] Christian Sanner, Edward J Su, Aviv Keshet, Ralf Gommers, Yong-il Shin, Wujie Huang, and Wolfgang Ketterle. Suppression of density fluctuations in a quantum degenerate fermi gas. *Physical review letters*, 105(4):040402, 2010.

[62] Christian Sanner, Edward J Su, Aviv Keshet, Wujie Huang, Jonathon Gillen, Ralf Gommers, and Wolfgang Ketterle. Speckle imaging of spin fluctuations in a strongly interacting fermi gas. *Physical review letters*, 106(1):010402, 2011.

[63] DS Petrov. Three-body problem in fermi gases with short-range interparticle interaction. *Physical Review A*, 67(1):010703, 2003.

[64] Marko Cetina, Michael Jag, Rianne S Lous, Isabella Fritsche, Jook TM Walraven, Rudolf Grimm, Jesper Levinsen, Meera M Parish, Richard Schmidt, Michael Knap, et al. Ultrafast many-body interferometry of impurities coupled to a fermi sea. *Science*, 354(6308):96–99, 2016.

[65] Giacomo Valtolina. *Superfluid and spin dynamics of strongly interacting atomic Fermi gases*. PhD thesis, Scuola Normale Superiore di Pisa, 2016.

[66] Harold J Metcalf and Peter Van der Straten. *Laser cooling and trapping*. Springer Science & Business Media, 2012.

[67] Massimo Inguscio and Leonardo Fallani. *Atomic physics: precise measurements and ultracold matter*. OUP Oxford, 2013.

[68] DS Petrov, Christophe Salomon, and GV Shlyapnikov. Scattering properties of weakly bound dimers of fermionic atoms. *Physical Review A*, 71(1):012708, 2005.

[69] Daniel A Steck. Quantum and atom optics. *Oregon Center for Optics and Department of Physics, University of Oregon*, 47, 2007.

[70] Andrew T Grier, Igor Ferrier-Barbut, Benno S Rem, Marion Delehaye, Lev Khaykovich, Frédéric Chevy, and Christophe Salomon. λ-enhanced sub-doppler cooling of lithium atoms in d 1 gray molasses. *Physical Review A*, 87(6):063411, 2013.

[71] D Rio Fernandes, Franz Sievers, Norman Kretzschmar, Saijun Wu, Christophe Salomon, and Frédéric Chevy. Sub-doppler laser cooling of fermionic 40k atoms in three-dimensional gray optical molasses. *EPL (Europhysics Letters)*, 100(6):63001, 2012.

[72] Dipankar Nath, R Kollengode Easwaran, G Rajalakshmi, and CS Unnikrishnan. Quantum-interference-enhanced deep sub-doppler cooling of 39 k atoms in gray molasses. *Physical Review A*, 88(5):053407, 2013.

[73] Ya-Fen Hsiao, Yu-Ju Lin, and Ying-Cheng Chen. Raman gray molasses cooling of cesium atoms on the d2 line. *arXiv preprint arXiv:1807.05745*, 2018.

[74] A Burchianti, G Valtolina, JA Seman, E Pace, M De Pas, M Inguscio, M Zaccanti, and G Roati. Efficient all-optical production of large li 6 quantum gases using d 1 gray-molasses cooling. *Physical Review A*, 90(4):043408, 2014.

[75] Michael Jag, Matteo Zaccanti, Marko Cetina, Rianne S Lous, Florian Schreck, Rudolf Grimm, Dmitry S Petrov, and Jesper Levinsen. Observation of a strong atom-dimer attraction in a mass-imbalanced fermi-fermi mixture. *Physical review letters*, 112(7):075302, 2014.

[76] G Breit. G. breit and ii rabi, phys. rev. 38, 2082 (1931). *Phys. Rev.*, 38:2082, 1931.

[77] Franziska Kaminski. *Coherent Atom-Light Interaction in an Ultracold Atomic Gas Experimental Study of Faraday Rotation Imaging and Matter-Wave Superradiance.* PhD thesis, 2012.

[78] G Reinaudi, T Lahaye, Z Wang, and D Guéry-Odelin. Strong saturation absorption imaging of dense clouds of ultracold atoms. *Optics letters*, 32(21):3143–3145, 2007.

[79] Andrea Amico. *Measurement of the Equation of State of superfuid Fermi gases of lithium-6 atoms, Master thesis.* University of Florence, 2014.

[80] Wolfgang Ketterle, Dallin S Durfee, and DM Stamper-Kurn. Making, probing and understanding bose-einstein condensates. *arXiv preprint cond-mat/9904034*, 1999.

[81] Miroslav Gajdacz, Poul L Pedersen, Troels Mørch, Andrew J Hilliard, Jan Arlt, and Jacob F Sherson. Non-destructive faraday imaging of dynamically controlled ultracold atoms. *Review of Scientific Instruments*, 84(8):083105, 2013.

[82] Christian Sanner. *Fluctuations in Quantum Degenerate Fermi Gases.* PhD thesis, 2012.

[83] Brian DeMarco and Deborah S Jin. Onset of fermi degeneracy in a trapped atomic gas. *Science*, 285(5434):1703–1706, 1999.

[84] Brian DeMarco. *Quantum behavior of an atomic Fermi gas.* University of Colorado, 2001.

[85] GD Mahan. Many-particle physics, (kluwer academic/plenum publishers, new york, 2000).

[86] AP Chikkatur, A Görlitz, DM Stamper-Kurn, S Inouye, S Gupta, and W Ketterle. Suppression and enhancement of impurity scattering in a bose-einstein condensate. *Physical review letters*, 85(3):483, 2000.

[87] S Nascimbène. S. nascimbène, n. navon, kj jiang, l. tarruell, m. teichmann, j. mckeever, f. chevy, and c. salomon, phys. rev. lett. 103, 170402 (2009). *Phys. Rev. Lett.*, 103:170402, 2009.

[88] André Schirotzek, Cheng-Hsun Wu, Ariel Sommer, and Martin W Zwierlein. Observation of fermi polarons in a tunable fermi liquid of ultracold atoms. *Physical review letters*, 102(23):230402, 2009.

[89] J Catani, G Lamporesi, D Naik, M Gring, M Inguscio, F Minardi, Adrian Kantian, and Thierry Giamarchi. Quantum dynamics of impurities in a one-dimensional bose gas. *Physical Review A*, 85(2):023623, 2012.

[90] Nicolas Spethmann, Farina Kindermann, Shincy John, Claudia Weber, Dieter Meschede, and Artur Widera. Dynamics of single neutral impurity atoms immersed in an ultracold gas. *Physical review letters*, 109(23):235301, 2012.

[91] R Scelle, T Rentrop, A Trautmann, T Schuster, and MK Oberthaler. Motional coherence of fermions immersed in a bose gas. *Physical review letters*, 111(7):070401, 2013.

[92] Christoph Kohstall, Mattheo Zaccanti, Matthias Jag, Andreas Trenkwalder, Pietro Massignan, Georg M Bruun, Florian Schreck, and Rudolf Grimm. Metastability and coherence of repulsive polarons in a strongly interacting fermi mixture. *Nature*, 485(7400):615, 2012.

[93] Marco Koschorreck, Daniel Pertot, Enrico Vogt, Bernd Fröhlich, Michael Feld, and Michael Köhl. Attractive and repulsive fermi polarons in two dimensions. *Nature*, 485(7400):619, 2012.

[94] Pietro Massignan and GM Bruun. Repulsive polarons and itinerant ferromagnetism in strongly polarized fermi gases. *The European Physical Journal D*, 65(1-2):83–89, 2011.

[95] Richard Schmidt and Tilman Enss. Excitation spectra and rf response near the polaron-to-molecule transition from the functional renormalization group. *Physical Review A*, 83(6):063620, 2011.

[96] Frédéric Chevy. Universal phase diagram of a strongly interacting fermi gas with unbalanced spin populations. *Physical Review A*, 74(6):063628, 2006.

[97] Nikolay Prokofâev and Boris Svistunov. Fermi-polaron problem: Diagrammatic monte carlo method for divergent sign-alternating series. *Physical Review B*, 77(2):020408, 2008.

[98] R Combescot, A Recati, C Lobo, and Fv Chevy. Normal state of highly polarized fermi gases: simple many-body approaches. *Physical review letters*, 98(18):180402, 2007.

[99] Jonas Vlietinck, Jan Ryckebusch, and Kris Van Houcke. Quasiparticle properties of an impurity in a fermi gas. *Physical Review B*, 87(11):115133, 2013.

[100] RF Bishop. Ground-state energy of a dilute fermi gas. *Annals of Physics*, 77(1-2):106–138, 1973.

[101] Christian Trefzger and Yvan Castin. Polaron residue and spatial structure in a fermi gas. *EPL (Europhysics Letters)*, 101(3):30006, 2013.

[102] Christophe Mora and Frédéric Chevy. Normal phase of an imbalanced fermi gas. *Physical review letters*, 104(23):230402, 2010.

[103] Pietro Massignan, Georg Morten Bruun, and HTC Stoof. Twin peaks in rf spectra of fermi gases at unitarity. *Physical Review A*, 77(3):031601, 2008.

[104] J. Bardeen, G. Baym, and D. Pines. Effective interaction of he^3 atoms in dilute solutions of he^3 in he^4 at low temperatures. *Phys. Rev.*, 156:207–221, Apr 1967.

[105] F. Chevy and Christophe Mora. Ultra-cold polarized Fermi gases. *Rep. Progr. Phys.*, 73(11):112401, November 2010.

[106] Zhenhua Yu. Short-range correlations in dilute atomic fermi gases with spin-orbit coupling. *Phys. Rev. A*, 85:042711, Apr 2012.

[107] Michael Feld, Bernd Fröhlich, Enrico Vogt, Marco Koschorreck, and Michael Köhl. Observation of a pairing pseudogap in a two-dimensional fermi gas. *Nature*, 480(7375):75, 2011.

[108] M Zwierlein. Thermodynamics of strongly interacting fermi gases. In *Proceedings of the International School of Physicsâ Enrico Fermi*, volume 191, pages 143–220, 2016.

[109] AB Bardon, S Beattie, C Luciuk, W Cairncross, D Fine, NS Cheng, GJA Edge, E Taylor, S Zhang, S Trotzky, et al. Transverse demagnetization dynamics of a unitary fermi gas. *Science*, 344(6185):722–724, 2014.

[110] Richard J Fletcher, Raphael Lopes, Jay Man, Nir Navon, Robert P Smith, Martin W Zwierlein, and Zoran Hadzibabic. Two-and three-body contacts in the unitary bose gas. *Science*, 355(6323):377–380, 2017.

[111] Pietro Massignan, Matteo Zaccanti, and Georg M Bruun. Polarons, dressed molecules and itinerant ferromagnetism in ultracold fermi gases. *Reports on Progress in Physics*, 77(3):034401, 2014.

[112] Timo Bastian Ottenstein, T Lompe, M Kohnen, AN Wenz, and S Jochim. Collisional stability of a three-component degenerate fermi gas. *Physical review letters*, 101(20):203202, 2008.

[113] JH Huckans, JR Williams, EL Hazlett, RW Stites, and KM OâHara. Three-body recombination in a three-state fermi gas with widely tunable interactions. *Physical review letters*, 102(16):165302, 2009.

[114] Shizhong Zhang and Tin-Lun Ho. Atom loss maximum in ultra-cold fermi gases. *New Journal of Physics*, 13(5):055003, 2011.

[115] G Valtolina, F Scazza, A Amico, A Burchianti, A Recati, T Enss, M Inguscio, M Zaccanti, and G Roati. Exploring the ferromagnetic behaviour of a repulsive fermi gas through spin dynamics. *Nature Physics*, 13(7):704, 2017.

[116] Elbio Dagotto, Jan Burgy, and Adriana Moreo. Nanoscale phase separation in colossal magnetoresistance materials: lessons for the cuprates? *Solid State Communications*, 126(1-2):9–22, 2003.

[117] Jörg Schmalian and Peter G Wolynes. Stripe glasses: self-generated randomness in a uniformly frustrated system. *Physical review letters*, 85(4):836, 2000.

[118] Tommaso Roscilde and J Ignacio Cirac. Quantum emulsion: A glassy phase of bosonic mixtures in optical lattices. *Physical review letters*, 98(19):190402, 2007.

[119] MR Norman. Novel superfluids vol 2 ed kh bennemann and jb ketterson, 2014.

[120] Kenji Fukushima and Tetsuo Hatsuda. The phase diagram of dense qcd. *Reports on Progress in Physics*, 74(1):014001, 2010.

[121] GJ Conduit. Itinerant ferromagnetism in a two-dimensional atomic gas. *Physical Review A*, 82(4):043604, 2010.

[122] Xiaoling Cui and Tin-Lun Ho. Ground-state ferromagnetic transition in strongly repulsive one-dimensional fermi gases. *Physical Review A*, 89(2):023611, 2014.

[123] C Luciuk, S Smale, F Böttcher, H Sharum, BA Olsen, S Trotzky, T Enss, and JH Thywissen. Observation of quantum-limited spin transport in strongly interacting two-dimensional fermi gases. *Physical review letters*, 118(13):130405, 2017.